Results from a 3.1 kg day Target Exposure with Skipper CCDs from DAMIC at SNOLAB and other Beyond the Standard Model Searches with Semiconductor Detectors

Alexander Piers

A dissertation

submitted in partial fulfillment of the

requirements for the degree of

Doctor of Philosophy

University of Washington

2023

Reading Committee:

Alvaro Chavarria, Chair

Shih-Chieh Hsu

Miguel Morales

Program Authorized to Offer Degree:

Physics

University of Washington

Abstract

Results from a 3.1 kg day Target Exposure with Skipper CCDs from DAMIC at SNOLAB and other Beyond the Standard Model Searches with Semiconductor Detectors

Alexander Piers

Chair of the Supervisory Committee:
Assistant Professor Alvaro Chavarria
Physics

We present here progress on a dark matter (DM) and neutrionless double beta decay ($0\nu\beta\beta$) experimental search. We constrained the WIMP-nucleon scattering cross section $<$ 9 GeV/c^2 in a silicon target with an 11 kg days exposure from CCD detectors in the DAMIC at SNOLAB experiment. We also observed an unexplained excess above our background model of 17.1 $\pm$ 6.7 bulk events with an exponential decay length of 67 $\pm$ 37 eV$_{\rm ee}$. To investigate, we deployed skipper CCDs with significantly lower readout noise at SNOLAB and acquired 3.1 kg days—the largest skipper CCD exposure ever recorded—of data with an analysis threshold (10% reconstruction efficiency) of 6 e$^-$. We found a population of 11 (15) clusters below 200 (400) eV$_{\rm ee}$, which was above the expected background rate. We characterized this excess over the known bulk backgrounds as a decaying exponential with 12.3 $\pm$ 3.9 events and decay length of 89 $\pm$ 30 eV$_{\rm ee}$. A comparison of the energy scale and event rate of the two excesses suggest the data between the traditional and skipper CCD data sets are compatible and could share a common origin. We also operated skipper CCDs at the Modane Underground Laboratory and constrained new parameter space for the DM-e$^-$ scattering cross section in the mass range 1.6-1000 MeV/c^2 for the ultra-light and 1.5-15.1 MeV/c^2 for the heavy mediator. Finally, as a proof-of-concept for the Selena Neutrino Experiment, we developed a pixelated amorphous selenium sensor sensitive to single

γ/β interactions.

TABLE OF CONTENTS

LIST OF FIGURES

LIST OF TABLES

ACKNOWLEDGMENTS

It is an impossible task to thank the all the individuals who contributed to my graduate school journey.

To my DAMIC, Selena, and CENPA collaborators, I appreciate all the contributions—hardware, software, ideas, and many others—over the years. In my opinion, you all helped elevate the quality of science performed in these experiments. I want to specifically thank Alvaro Chavarria for his guidance throughout this process. Alvaro, you always gave quality and thoughtful suggestions to the problems we were investigating while giving me the freedom to address the problem how I saw fit. I appreciate your mentorship over the last few years.

I could not have completed, or even undertaken, this journey without my family. To my parents, Kevin and Gloria, your lifelong value of education and support of pursuing my interests were crucial in my decision to attend and persevere through graduate school. Amani and Nico, I am thankful to have such impressive, inspirational, and fun siblings.

And finally Elisa, you are the most supportive partner anybody could ask for. Your patience with and belief in me meant more than I can express. I couldn't have done this without you.

Chapter 1
INTRODUCTION

The Standard Model of Physics [1]—the mathematical framework that describes the subatomic world—should be considered nothing less than a resounding success of modern science. Numerous theoretical predication have been verified by experiments [2], including the discovery of the: charm [3], top [4, 5], and bottom [6] quarks; gluon [7, 8]; and W, Z [9][10], and Higgs Boson [11]. Additionally, many of these particles' measured properties were correctly predicted by the theory. However, there are several notable contemporary observations that the Standard Model does not explain, such as the existence of dark matter and energy, the hierarchy problem [12], or the excess of matter over anti-matter [13, 14] in the universe.

This thesis will discuss two experiments aimed at uncovering the answers to some of these questions left open by the Standard Model. The DAMIC experiment searches for low mass dark matter using charge-coupled devices (Chapters 2 and 3) and Selena experiment probes neutrino phenomena with pixelated CMOS detectors coupled to enriched amorphous ^{82}Se (Chapter 4). The remainder of the introduction will be dedicated to a simple overview of these topics with just enough background to understand the later chapters. I will let others explain the theory in more depth and with superior accuracy; please follow the references in the next sections for more details.

1.1 Dark Matter Searches

There is a considerable amount of cosmological evidence for the existence of some non-luminous, non-baryonic matter in the universe. Galaxy rotation curves [15, 16], gravitational lensing of the bullet cluster [17], and the cosmic microwave background spectral density

[18, 19] all suggest that there is a large amount of matter that interacts gravitationally, but not electromagnetically (hence the name "dark matter"). Each observation, despite the vast differences in length scale, predict similar ratios of baryonic to dark matter; the Planck Collaboration measured the energy density of baryonic and dark matter as 4.9% and 26.1% of the total universe energy density, respectively [19].

There are many proposed dark matter candidates varying over a large range of mass that could be measured by different experimental techniques: ultralight candidates ($\mathcal{O}(\text{peV} - \text{meV})$) like axions would couple to haloscope devices such as those used in ADMX [20], ORPHEUS [21], or ABRACADABRA [22]; Standard Model scale masses ($\mathcal{O}(\text{keV} - \text{TeV})$ like "Hidden" dark sector or Weakly Interacting Massive Particles (WIMPS) would scatter off atoms in sensitive calorimeters; or even extremely heavy in the form of primordial black holes or other astrophysical objects [23] could be observed in sky surveys. Furthermore, attempts have been made to create a theory that modifies gravity, called Modified Newtonian Dynamics (MOND), to explain the astrophysical observations without introducing a new particle [24, 25], but so far have been unable to reconcile all anomalous gravitational observations [26]. The remainder of this thesis will focus on the Standard Model scale scattering DM candidates. An excellent review of the theory, motivation, and strategies behind this type of dark matter candidate can be found in the community reports in Ref. [27, 28, 29].

We consider cold dark matter candidates that are bound by the gravitational pull of the galaxy. We characterize dark matter as particles with some local density ρ following a Maxwellian velocity distribution with an upper cutoff of the galactic escape velocity. As the earth rotates around the galaxy/sun, it drifts through these particles at a velocity dependent on the galactic and solar rotations. The values of these variables, known as the "Standard Halo Model" parameters, are largely agreed upon by the community and can be found in Ref. [30]. We can then model the DM interactions in an instrumented target based off the kinematics of scattering between dark matter and detector particles, which is of course model dependent. For example, the WIMP differential scattering rate can be computed as

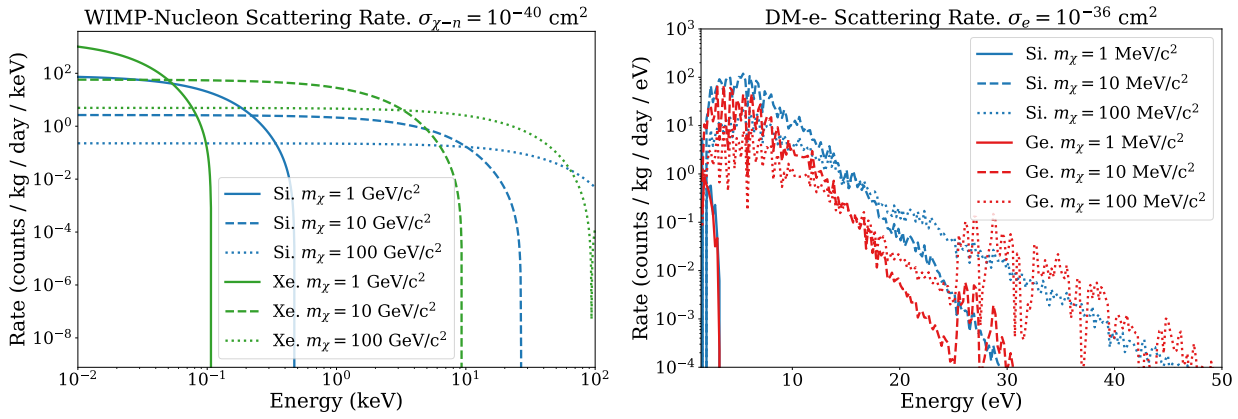

(a) (b)

Figure 1.1: (a) differential scattering rate of WIMPs off of target (Si and Xe) nuclei for a range of masses and cross section of 10^{-40} cm^2 and (b) inelastic scatter of dark matter and electrons in a crystalline targets (Si and Ge) at a cross section of 10^{-36} cm^2. Note the differences in energy scale, scattering rate, and mass for the two dark matter candidates.

$$\frac{d\Gamma}{dE_{\rm nr}} = \frac{\sigma_0 \rho_0 F^2(q)}{2 m_\chi \mu^2} \int_{v_{\rm min}}^{\infty} \frac{f(v)}{v} d^3 v, \tag{1.1}$$

where σ_0 is the cross section at 0 momentum transfer, ρ_0 the local DM density, $F(q)$ the form factor that encodes information of the target nucleus, m_χ the DM mass, μ the reduced mass of the DM-nucleon system, and $f(v)$ the DM velocity distribution in the lab frame.

A full treatment of these calculations can be found in many locations, such as Ref. [31, 32] for the WIMP spectrum. For different DM models, while the approach remains similar, other complications need to be accounted for in the kinematic exchange, such as the bound states of electrons in semiconductors as in Ref. [33, 34]. Two sample DM candidate spectra can be found in Figure 1.1.

The energy from DM interaction is deposited in a detector and can create a measurable signal in the form of ionization (DAMIC [35]), scintillation (COSINE [36], DEAP [37]), or

vibrations. Many experiments measure two channels—light and charge (XENON [38], LUX [39], Darkside [40]), phonons and charge (EDELWEISS [41], CDMS [42]), or phonons and light (CRESST [43])—and use the combination to discriminate between β/γ backgrounds and the nuclear recoils expected from a WIMP interaction. In any case, the original energy of the interaction can be inferred from these signals after an extensive calibration campaign. We then search for some DM signal over the known radioactive backgrounds, which are computed using detailed simulations and data—such as radioactive assays or in-situ calibrations—outside the DM region of interest. Eventually, with enough statistics, experiments would observe the differential scattering rate change due to the time varying relative velocity of the DM wind as the earth orbits the sun; this is known as "annual modulation" and if observed and confirmed, would be extremely compelling evidence for a dark matter discovery.

To maximize experimental sensitivity, we need three factors: large exposure, providing the most potential targets for the the DM flux to interact with; low backgrounds in the region of interest to be able to statistically observe a signal over the known backgrounds; and excellent energy response in the region of interest (typically a low energy threshold for scattering experiments which gives a access to a larger fraction to the differential spectrum). Each generation of experiments—including those detailed in the later chapters—aim to improve upon these factors simultaneously to probe further in the mass-cross section parameter space of a DM model and hopefully discover the nature of dark matter.

1.2 Neutrino Physics

The history of neutrino physics is rich, and I point the reader to Ref. [44, 45, 46] for a more complete picture. I will briefly explain two particular phenomenon that are most relevant to the experimental attempts discussed later in this thesis.

One clear experimental signature of new physics would be neutrinoless double beta decay ($0\nu\beta\beta$); comprehensive reviews of the topic can be found in Ref. [47, 48]. The nature of neutrinos are not fully understood. It is possible they are Dirac particles, meaning neutrinos and antineutrinos are distinct particles, or Majorana, where they are their own antiparticle.

If they are Majorana, it is possible that in the rare but allowed standard model process of $2\nu\beta\beta$

$$(A, Z) \rightarrow (A, Z + 2) + 2e^- + 2\bar{\nu_e} \tag{1.2}$$

the neutrinos annihilate via an exchange of light massive Majorana neutrinos and only the electrons are emitted

$$(A, Z) \rightarrow (A, Z + 2) + 2e^- \tag{1.3}$$

which is known as $0\nu\beta\beta$. Since there are no neutrinos to carry away energy, the decay energy, $Q_{\beta\beta}$, is carried by only the electrons. The energy of the electrons can be measured and we expect a clear experimental signature of a populations of decays above all backgrounds (including the irreducible $2\nu\beta\beta$) at precisely $Q_{\beta\beta}$. A toy example of this is illustrated in Figure 1.2(c). Furthermore, since there are no antineutrinos emitted, the process does not conserve the baryon minus lepton number, which is not allowed in the Standard Model.

This process, if discovered, would have significant implications on our understandings of fundamental physics. It would illuminate the nature of neutrinos, provide a possible mechanism for leptogenisis [13], and constrain the absolute mass of the neutrino (which is currently an active area of particle physics with several different experiment searching for the value [49, 50, 51]). That is because the half life

$$T^{0\nu}_{1/2} = \left(G_{0\nu} |\mathcal{M}|^2 \left(\frac{m_{\beta\beta}}{m_e} \right)^2 \right)^{-1} \tag{1.4}$$

depends on the phase space factor ($G_{0\nu}$), nuclear matrix elements ($\mathcal{M}$) [52], mass of the electron (m_e), and effective Majorana mass ($m_{\beta\beta}$), where

$$m_{\beta\beta} = \sum_{i=1}^{3} U^2_{ei} m_i \tag{1.5}$$

where U_{ei} is the PNMS neutrino mixing matrix [53], and here the sum is specifically over the ν_e mass states. It should be clear if we are able to detect $0\nu\beta\beta$ and measure the half

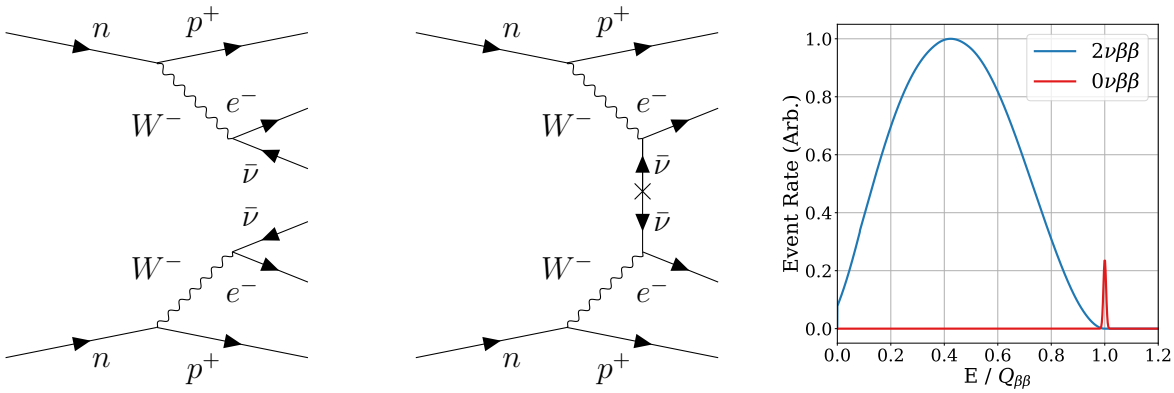

Figure 1.2: (a) Feynnman diagram of traditional $2\nu\beta\beta$ decay (b) $0\nu\beta\beta$ decay with the exchange of a massive Majorana neutrino (c) signature of a $0\nu\beta\beta$ experiment. These experiments search for a δ peak at the decay Q value (and then some Gaussian energy resolution) on top of the $2\nu\beta\beta$ spectrum. The amplitude of the $0\nu\beta\beta$ signature has been significantly exaggerated here for illustrative purposes.

life, we can constrain the mass of the neutrino. The phase space factor and nuclear matrix elements have significant theoretical uncertainty [47][54], so this is not a model independent approach, emphasizing the need for confirmation via other experimental techniques.

A major effort is underway to discover this process. Similar to dark matter searches, these experiments require a large exposure, ultra-low background specifically around the $Q_{\beta\beta}$ range, and excellent energy resolution to prevent events "bleeding" from the $2\nu\beta\beta$ background into the ROI. The sensitivity of the half life

$$T_{1/2}^{0\nu} \propto \begin{cases} MT \text{ if } b = 0 \\ \sqrt{MT} \text{ if } b > 0 \end{cases} \tag{1.6}$$

scales with the exposure (MT) in different functional forms, depending on the amount of background b in the search region, emphasizing the above experimental parameters. Cur-

rently experiments are looking at for $0\nu\beta\beta$ in ^{76}Ge (GERDA, $T^{0\nu}_{1/2} > 1.8 \times 10^{26}$ yr [55]), ^{82}Se (CUPID, $T^{0\nu}_{1/2} > 4.6 \times 10^{24}$ yr [56]), ^{100}Mo (CUPID, $T^{0\nu}_{1/2} > 1.5 \times 10^{24}$ yr [57]), ^{130}Te (CUORE, $T^{0\nu}_{1/2} > 2.2 \times 10^{25}$ yr [58]), ^{136}Xe (KamLAND-Zen, $T^{0\nu}_{1/2} > 2.3 \times 10^{26}$ yr [59]), as well as a few others with less competitive lower limits. The next generation of experiments are underway and aim to achieve $T^{0\nu}_{1/2} \sim \mathcal{O}(10^{27}$ yr) sensitivity and fully probe the $m_{\beta\beta}$ allowed by the inverted ordering of neutrino masses [54]. Future generations aim to reach $T^{0\nu}_{1/2} \sim \mathcal{O}(10^{28}$ yr).

A different phenomenon, neutrino flavor oscillations [45] were discovered in the last 25 years and observed in a number of experiments [60, 61, 62, 63, 64]. They arise due to the mixing of mass and flavor eigenstates of neutrinos and were the first indication that neutrinos had mass. We have only observed oscillations between ν_e, ν_μ, and ν_τ flavors, but the possibility of mixing into alternative flavor "sterile" neutrinos [65, 66]—neutrinos that do not interact with via the weak nuclear force—exists. Other than general interest as a beyond the Standard Model particle, a sterile neutrino could also be a dark matter candidate [67]. A number of current experiments are searching for the mixing of standard model (anti)neutrinos with their sterile counterparts, searching for an unexplained deficit in the measured neutrino flux from some source, such as nuclear reactors, radioactive sources, or particle accelerators. The results have been mixed, ranging from null results to some significant anomalies. Chapter 4 includes a further discussion on this topic in relation to the Selena experiment.

Chapter 2

DAMIC AT SNOLAB LOW ENERGY ANALYSIS

The DAMIC (Dark Matter in CCDs) experiment is a dark matter (DM) search aimed at detecting low energy recoils of dark matter particles off the nuclei or electrons in a silicon atom. The DM candidates are discussed in Chapter 1 and span a variety of theoretical models, but DAMIC leverages its low dark current and readout noise to search for the low mass WIMP and dark sector candidates.

2.1 DAMIC at SNOLAB 11 kg day Setup

A significant effort had previously gone into constructing the DAMIC experiments and detailed descriptions of the apparatus can be found in references [35] and [68] (and a diagram in Figure 2.1). At the core of the detector are seven functioning $\sim$ 16 megapixel charge-coupled devices (CCDs). Energy deposited in the CCDs creates a number of electron hole (e-h) pairs proportional to the energy (1 e^-/3.8 eV) of the interaction that are drifted across the z direction of the detector by an electric field created by the substrate bias (V_{sub}). While drifting, the charge thermally diffuses outwards following a Gaussian distribution with the variance proportional to the drift time ($\sigma^2 = Dt$) which is related to the depth of interaction and the electric field in the detector. The charge is collected near the front surface of the detector held by the potential of the CCD buried channel in a 2D projection of the energy deposited convolved with the depth dependent diffusion. The collected charge is held lossless during the detector exposure until readout. A set of three-phase potentials, called the parallel or vertical clocks, shift the charge row-by-row into the serial register. Here, a different set of three-phase potentials, the serial or horizontal clocks, shift each charge, one pixel at a time, to the amplifiers to readout the charge. The amplifiers perform correlated

double sampling (CDS) by integrating the voltage of an empty sense node (pedestal) and one filled with charge from the pixel (signal). The difference between the signal and pedestal values is proportional to the charge in the pixel, and therefore the energy. We are able to measure x, y, z positions and charge/energy of interactions, which is enough information for a dark matter detector. We achieved a readout noise of 1.6 e^- and pixel array dark current of $\mathcal{O}(10^{-4})$ e^-/pix/day. Both these values are extremely low and allow for a low mass DM search.

Figure 2.1 shows the experimental setup. Each CCD was held in a copper tray and has a flexible PCB connected to deliver/receive the control/readout signals. CCD1 was stored in an electroformed copper tray from PNNL and sandwiched between two ancient lead bricks. The other CCDs, CCD2-7, were stored in oxygen free (OFHC) copper trays. The trays slotted into a copper box that makes up the inner detector. The inner detector was capped by 18 cm of cylindrical lead pieces and placed in a copper cryostat. The cryostat fit into a lead castle with at least 21 cm of lead surrounding the detector from high energy external γ-rays. The innermost inch of lead surrounding the detector is ancient lead with minimal ^{210}Pb content. The lead castle was continuously flushed with N_2 gas from LN_2 boil-off to purge radon from near the detector. Finally the castle was surrounded by a 42 cm thick polyethylene shield to moderate environmental neutrons. The detector operated in vacuum ($\mathcal{O}(10^{-6}$ mbar)) and was cooled by a cryocooler to $\sim$ 140 K.

We aquired images with 30 or 100 kS exposure and readout the CCD with 100×1 hardware binning, i.e. placed 100 rows in the serial register and readout each the serial register pixels one at a time to make an effective pixel size of 1500×15 μm^2. This compressed the y direction spread of the track and reduced the charge distribution to 1-dimension in x, and thus we only measure σ_x. However, this method improves the signal to noise ratio since the charge is spread over fewer pixel, so the effective noise when clustering over multiple pixels is lower.

Data was taken from January 2017 to January 2019, resulting in a final exposure of 10.93 kg days, the most massive CCD exposure taken to date.

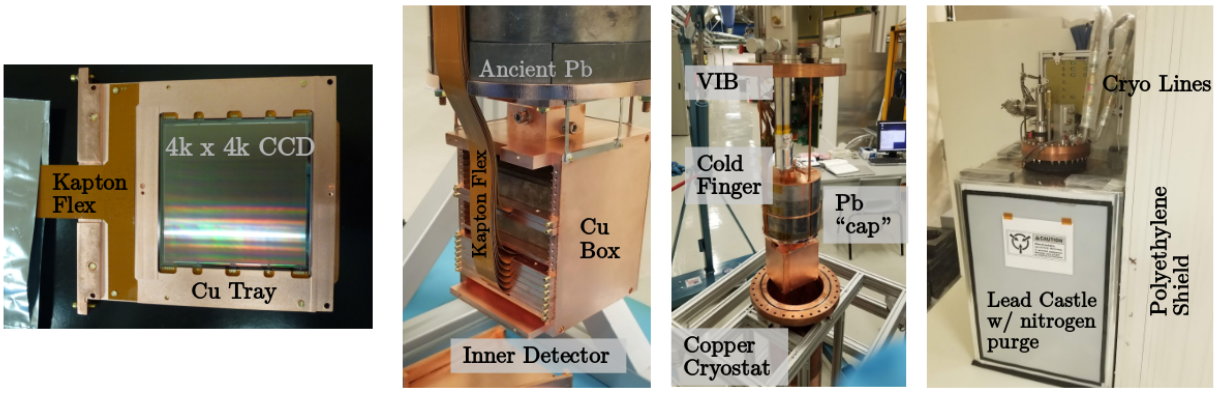

(a) (b) (c) (d)

Figure 2.1: DAMIC at SNOLAB detector setup. (a) A 4k x 4k CCD module installed in a copper tray. (b) The inner detector comprised of seven function CCD modules in a copper box. The top module (CCD1) is stored in electroformed copper and placed between two ancient lead bricks. (c) Cold finger, vacuum interface board (VIB), and inner detector preparing to go into the copper cryostat. (d) The cryostat placed in a 21 cm lead castle with nitrogen purge and a 42 cm polyethylene shield.

2.2 WIMP Search

The procedure and results of the search for Weakly Interacting Massive Particles (WIMPs) are discussed below.

2.2.1 Analysis Procedure

For the sake of brevity, the analysis procedure is abridged in the following section to focus more on the results. More details can again be found in Ref. [35, 69, 68]. We grouped adjacent pixels with charge values above the CCD baseline noise to form clusters and computed properties—position, energy, σ_x—of the cluster. We performed a likelihood clustering algorithm [35] on the data resulting in an efficiency down to 10% at 50 eV_{ee} and 90% at

120 eV_{ee} for the WIMP search data.

To construct a background model, we simulated the detector geometry in `Geant4` [70] [71] with radioactive contaminants in the detector parts from the ^{238}U, ^{232}Th, and ^{40}K decay chains. Additionally we specifically simulated ^{210}Pb on the CCD and copper surfaces and the cosmogenically activated isotopes of ^{3}H and ^{32}Si [72] uniformly throughout the CCDs. We grouped these simulations into 49 templates of contaminants from similar detector elements (i.e. module screws, CCD surface, etc.). We applied the detector response by sampling the position and energy of the interactions from the template, applying Fano noise [73], diffusion, and any partial charge collection, pasting the simulated events onto a "blank" (readout noise only) image with simulated shot noise, and applying the hardware binning. We clustered these simulated images to convert the radioactive templates from simulated variables ($E_{\rm sim}$, x, y, z) to observed variables (E, σ_x, x, y). We performed a likelihood fit in E-σ_x space for $E \in [6, 20]$ keV_{ee} of the data compared to a model of the summed weighted templates, where the weights (fit parameters) were constrained by radioactive assays. The `Geant4` templates were summed according to the fit weights and low energy (< 6 keV_{ee}) events from this distribution ($E_{\rm sim}$, x, y, z) were sampled, pasted on blanks (including detector response) and clustered. The clustered distribution was our background model (Figure 2.3(a)); a full table of the quantity of all contaminants is included in [68].

The partial charge collection (PCC) we include as a detector response is one of our main systematic uncertainties. A highly phosphorous doped (10^{18} atoms / cm^3) region is applied on the backside of the CCD to act as a conductive contact for the substrate bias. During fabrication, this layer can diffuse into the CCD, causing a gradient of phosphorous concentration down to 10^{11} atoms / cm^3, the nominal dopant concentration in the bulk. This gradient has been measured in DAMIC CCDs using secondary ion mass spectroscopy (SIMS) [68]. The changing dopant concentration affects the hole mobility, lifetime, and the electric field in this region, creating an increased probability of recombination before the charge escapes into the CCD bulk. The details of the numeric model can be found in Appendix A of Ref. [68]. Only a fraction of the charge created gets collected and thus pushes the true

event energy to lower reconstructed energies making this effect particularly problematic for a dark matter search. We included this as a detector effect on simulated data

$$q_{\text{collect}} = q_i \alpha(z), \tag{2.1}$$

where $\alpha(z)$ is the fraction of the initial charge (q_i) that escapes the PCC region to be collected and measured by the CCD (q_{collect}). $\alpha(z)$ ranges from 0 to 1 over a region 3 to 9 microns from the CCD backside. We used an ad hoc calculation to define the PCC and needed to estimate the systematic uncertainty. We varied two parameters of the model: 1) the overall position of the PCC or a shift in the z direction, and 2) the slope (shape) of the region. We simulated several shift in and outwards in 250 nm increments and vary the slope to $\pm 20\%$ (variations shown in (Figure 2.2(a)). We compared the spectral shape of simulated ^{210}Pb on the back surface under these different model assumptions and found that the position (shift) of the PCC to be the most important parameter that impacts the backside spectrum (Figure 2.2(b)). We also determined an efficient parametrization of the difference in the spectrum between the nominal model and systematic shifts with a single parameter

$$f(E) = N \exp\left(-\sqrt{E}/\beta\right), \tag{2.2}$$

where β is the shape parameter (0.18 $\text{keV}_{\text{ee}}^{1/2}$) and N is the amplitude that depends on the shift. The phenomenological function describes well the low energy effect of this systematic (Figure 2.2) and only deviates from simulation mildly at energies above 1 keV_{ee}. Furthermore, the difference in spectra when changing the slope to be negligible, so we neglected this variation as it would be unobservable in our data. A fascinating corollary is that this also accounts for the systematic uncertainty in the position of ^{210}Pb and presence of ^{3}H near the backside. The position of ^{210}Pb on the backside of the CCD or wafer has a negligible effect on the x-ray lines, but for the β spectrum, is effectively a shift in the PCC region position. For the possibility of ^{3}H in the CCD ISDP layer, the β spectrum will be distorted by the

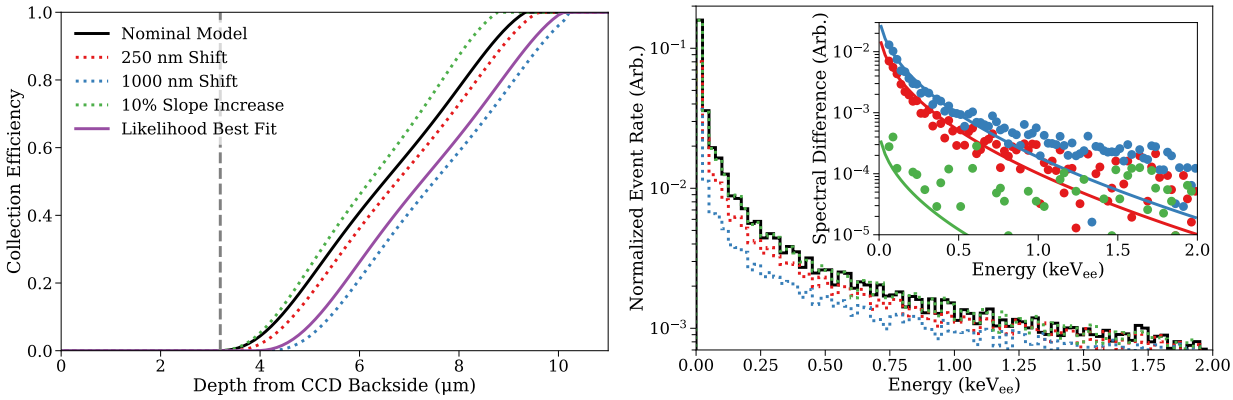

(a) (b)

Figure 2.2: PCC systematic uncertainty. (a) A sample of the various PCC models tested, varying the position of the start of the collection efficiency and the slope of the line representing the region compared to the nominal model (black). (b) Resulting spectrum from ^{210}Pb backside events in the case of the test and nominal PCC model along with the difference shown in the inset. These differences can be well parametrized at low energies by the functional for in equation 2.2. The functional form deviates above ~ 1 keV$_{ee}$, but $< 2\%$ of the integrated spectrum falls in that energy region; this is much less than the ultimate fit uncertainty on the PCC systematic parameter as describe in Section 2.2.2.

PCC and we found that the spectrum could also be described by Eqn 2.2. Ultimately the systematic parametrization of the PCC is an adjustment on the low energy β decays that interact in this region, and thus covers several different systematics. This is relevant for the reliability of the DM search; however, the downside is all these different systematics would be interpreted as an adjustment to the PCC position, even if the underlying reason is something else. Regardless, we include the the effect of the PCC region in the form of Eqn 2.2 as a systematic uncertainty by adding the amplitude N as nuisance parameter in our likelihood function.

For the WIMP search we performed an unbinned profile likelihood ratio test. We consid-

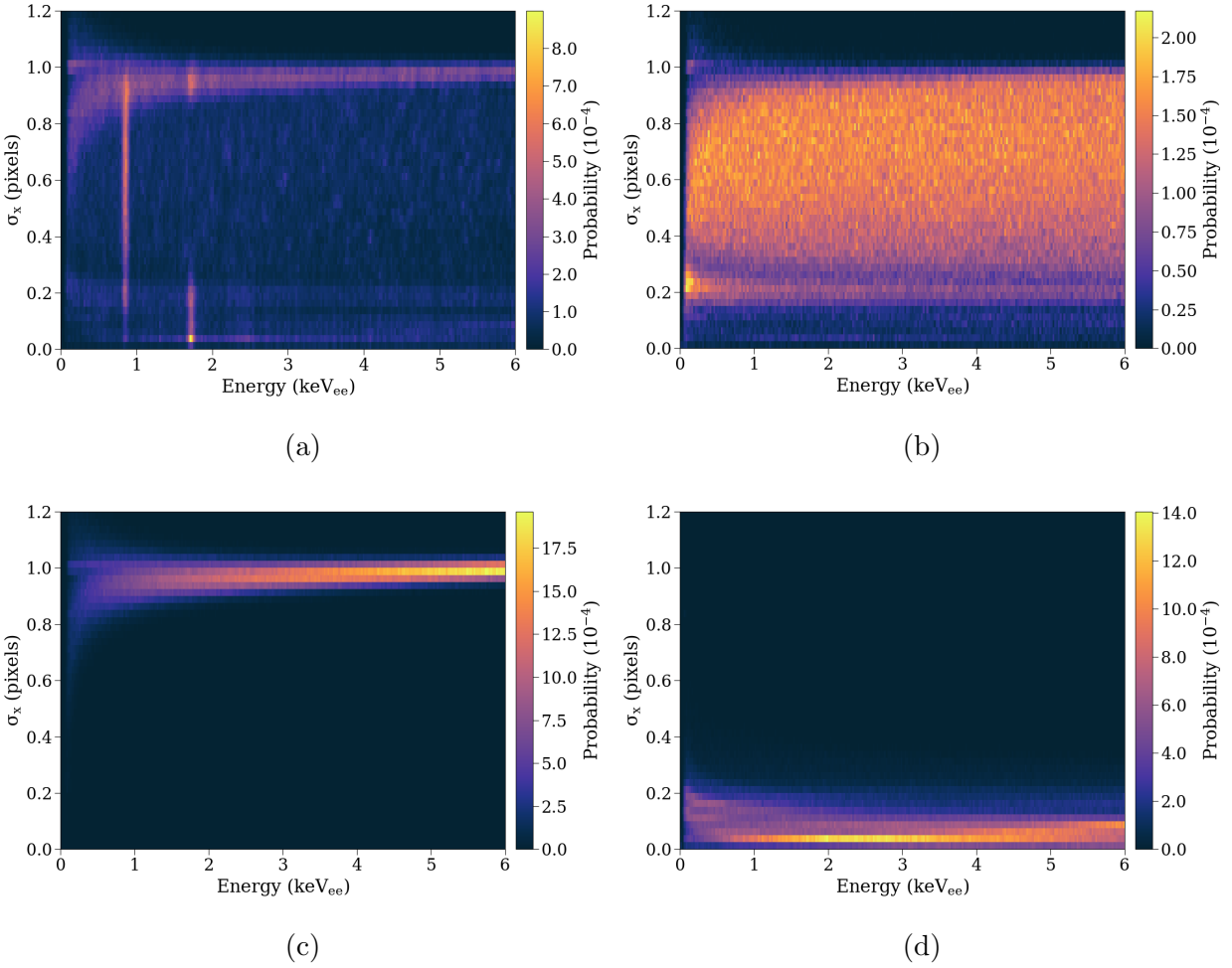

Figure 2.3: Probability distribution function of of events in E-σ_x space for different physical situations: (a) Energy and σ_x position following the extrapolated background model to low energies; (b) events distributed uniformly in energy and z position for use as the template for the signal models; (c) uniform energy distribution on the backside of the CCD; and (d) uniform energy distribution on the frontside of the CCD. We use these templates in the construction of our likelihood function.

ered two datasets, CCD1 and CCD2-7, as they experienced different background levels due to the electroformed copper and ancient lead. We defined an extended likelihood function in E-σ_x space for each data set:

$$\begin{aligned}\log \mathcal{L}(s,\epsilon,b,c|\vec{E},\vec{\sigma_x}) = &-(s+b+c)\\ &+\sum_i^N \log\left(sf_s(E_i,\sigma_{x_i}|\epsilon)+bf_b(E_i,\sigma_{x_i})+cf_c(E_i,\sigma_{x_i})\right)-\frac{(b-\bar{b})^2}{2\sigma_b^2}\end{aligned} \tag{2.3}$$

where s, b, and c are the number of signal, background, and partial charge collection events with PDFs f_s, f_b, and f_c, respectively. The energy component of the signal PDF is parametrized as a decaying exponential, with decaying length ϵ, convolved with a Gaussian resolution function that includes readout and Fano noise: $\sigma_n^2 = \sigma_r^2 + FE(3.8\text{ eV}_{\text{ee}})$, where the readout noise is $\sigma_r = 30\text{ eV}_{\text{ee}}$ and the Fano factor is 0.128 [74]. For energies $< 1\text{ keV}_{\text{ee}}$ the noise is almost entirely dominated by the readout noise, and thus we can define an analytic expression for signal spectrum

$$f_s(E|\epsilon,\sigma_n) = \underbrace{\frac{1}{2\epsilon}\exp\left(\frac{\sigma_n^2}{2\epsilon^2}\right)}_{\text{Norm}}\underbrace{\exp\left(\frac{-E}{\epsilon}\right)}_{\text{Shape}}\underbrace{\text{erfc}\left(\frac{\sigma_n^2/\epsilon - E}{\sqrt{2}\sigma_n}\right)}_{\text{Resolution}}, \tag{2.4}$$

where ϵ and σ_n are previously defined, and erfc is the standard complimentary error function. For f_c we use the energy parametrization of Eqn. 2.2. We converted the energy dependent functions of the signal and PCC components into E-σ_x space PDFs by multiplying the energy response with each σ_x bin in the detector responses at that energy, i.e. for the signal PDF:

$$f_s(E,\sigma_x|\epsilon,\sigma_n) = R(E,\sigma_x)\times f_s(E,|\epsilon,\sigma_n), \tag{2.5}$$

where $R(E,\sigma_x)$ is the distribution for a uniform spatial and energy distribution, shown in Figure 2.3(b) . We ensure that the integral of $f_s(E,\sigma_x|\epsilon,\sigma_n)$ is normalized to one and is

a true PDF. For the PCC component, $R(E, \sigma_x)$ is the response of a uniform energy signal interacting within 10 μm from the CCD backside (see Figure 2.3(c)).

We imposed a Gaussian penalty on the number of background events b in the data set. The mean predicted number of events $\bar{b}$ and uncertainty ($\sigma_b = 6\%$) was derived from the background model calculation to data above 6 keV_{ee}.

For the global fit, we considered both data sets in a joint likelihood function

$$\log \mathcal{L}_{\text{joint}}(s, \epsilon, b_1, c_1, b_{2\text{-}7}, c_{2\text{-}7}) = \sum_k \log \mathcal{L}(\gamma_k s, \epsilon, b_k, c_k) \tag{2.6}$$

where we summed over the k data sets (CCD1 and CCD2-7) each with their own number of background events (b_k) and spectral shape (f_{b_k}). We assumed a single DM shape (ϵ) and interaction cross section, such that the number of signal events observed in each data set is proportional to the fractional exposure γ_k. The number of PCC events is constrained to be proportional to the background rate on the backside of the CCD ($c_1 = 0.75 c_{2\text{-}7}$).

We minimized the $-\log \mathcal{L}_{\text{joint}}$ using `MINUIT` [75] for the results in the following section.

2.2.2 Results

For our search, we followed the procedure outline in [35], which is largely consistent with the dark matter community recommendations for rare physics searches [30].

We defined a test statistic:

$$q = -\log \left(\frac{\mathcal{L}(s = 0, \hat{\hat{\theta}})}{\mathcal{L}(\hat{s}, \hat{\theta})} \right) \tag{2.7}$$

where s, the number of signal events, is the parameter of interest and $\hat{\hat{\theta}}$ or $\hat{\theta}$ are the set of nuisance parameters—such as the number of background or PCC events—that maximize the likelihood function. The ratio of the background only hypothesis where we fix the signal strength to $s = 0$ and the global minimum where s is left free and maximizes the likelihood at $\hat{s}$ gives the significance of a dark matter signal.

Fit Parameter	Global Minimum	Background only ($s = 0$)
s	17.1 ± 6.7	0
ϵ ($\mathrm{eV_{ee}}$)	67 ± 37	–
b_1	57.6 ± 3.3	56.6 ± 3.1
$b_{2\text{-}7}$	609 ± 21	609 ± 21
c_1	0.9 ± 1.1	2.4 ± 1.1
$c_{2\text{-}7}$	6.6 ± 8.9	18.7 ± 8.3
q	6.82	

Table 2.1: Fit results of the likelihood search.

Our search yielded an unexpected excess of bulk ionization events at low energy. The fit global minimum preferred $s = 17.1 \pm 6.7$ events and spectral shape $\epsilon = 67 \pm 37$ $\mathrm{eV_{ee}}$ with a test statistic value of $q = 6.82$. For all results, we computed the significance using the Wilkes' theorem approximation that $2q$ follows a χ^2 distribution with the number of degrees of freedom equals to the difference in the number of free parameters from the null hypothesis (background only) and global minimum. This framework gave a p-value of 2.2×10^{-4}, or 3.7σ on a one-sided Gaussian, of that test statistic occurring randomly. The best fit results for the global minimum and background only hypothesis are included in Table 2.1. Figure 2.4 shows the data and background model of the low energy region in E-σ_x space. Specifically 2.4b shows the $[0, 1]$ $\mathrm{keV_{ee}}$ where the data < 200 $\mathrm{eV_{ee}}$ become inconsistent with the background model. The energy and σ_x projections are also shown with the global fit (red line) and background model (blue line).

An alternative way to inspect the excess is the global fit background model (b and c components) subtracted from the data in the energy parameter space, shown in Figure 2.5. Clearly the first three bins are inconsistent with zero, and the excess parametrization, including fit uncertainty, is overlaid and matches the data quite well. The dashed line shows

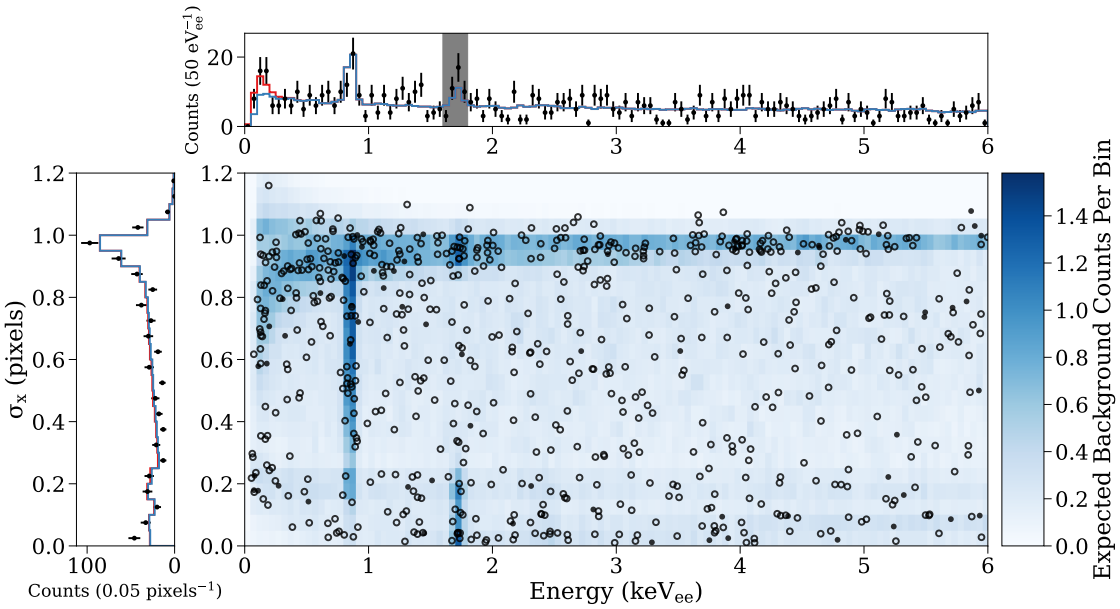

(a) $E \in [0, 6]$ keV$_{ee}$

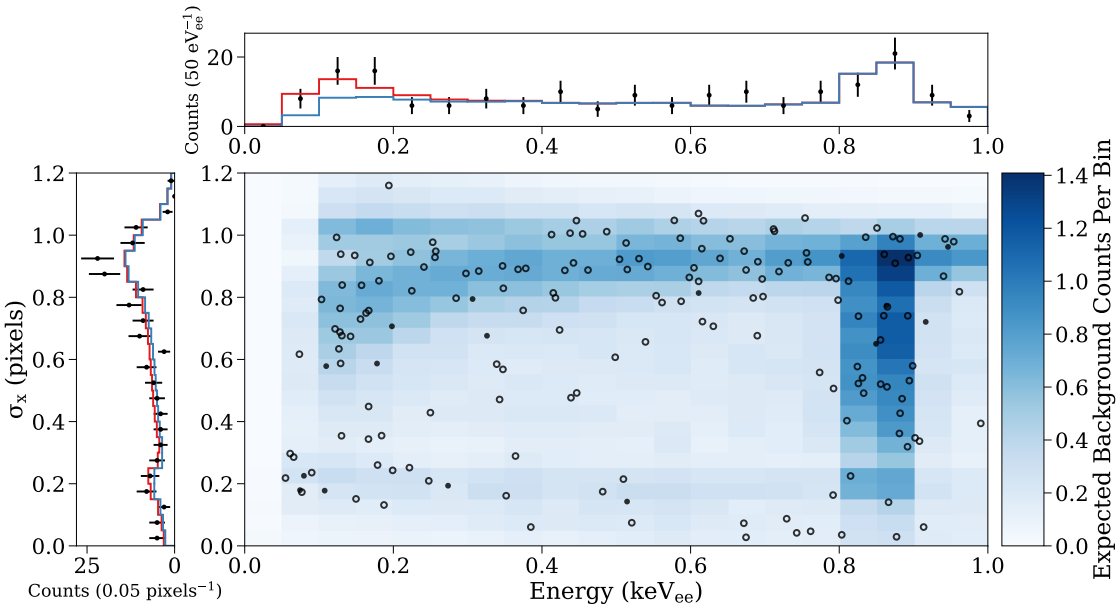

(b) $E \in [0, 1]$ keV$_{ee}$

Figure 2.4: Low energy fit result for (a) the entire ROI and (b) below 1 keV$_{ee}$ as described in the text.

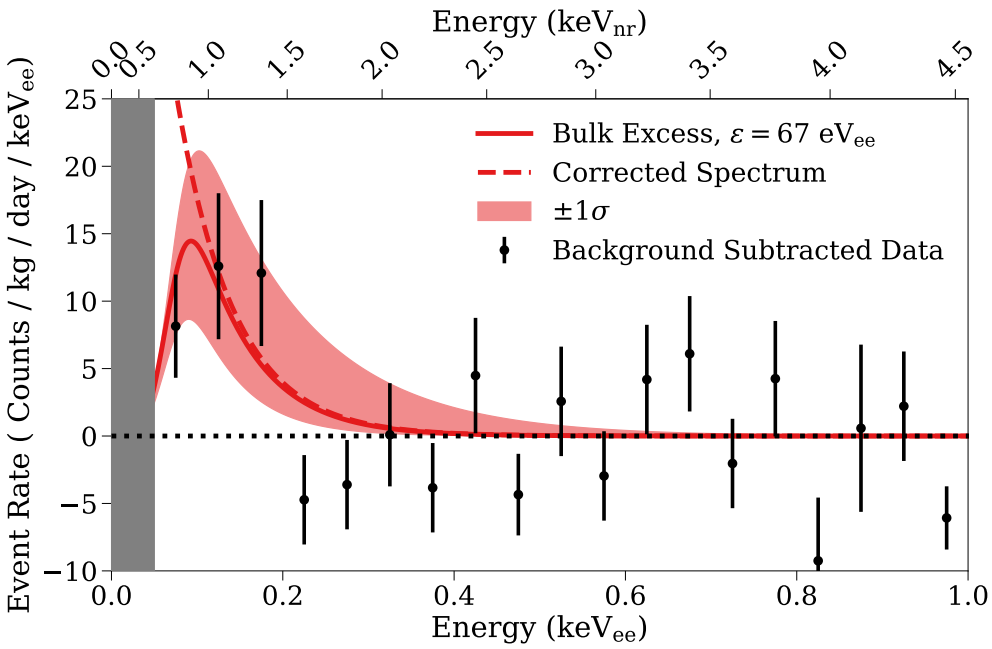

Figure 2.5: Energy projection of the background subtracted data using the best-fit background parameters for the global likelihood fit in electron equivalent (bottom axis) and nuclear recoil equivalent (top axis) energy [76]. The excess spectrum, including $\pm 1\sigma$ uncertainty, is shown in red. The uncertainty is only the Poisson uncertainty in each bin content before subtraction; the 6% uncertainty in the background model amplitude is a negligible addition. Clearly the first three bins are driving the signal preference and above 200 eV$_{ee}$ the data and background model are statistically compatible.

the efficiency corrected spectrum.

In spite of this excess over background of known radioactive contaminants, we did not claim a discovery (more discussion in Section 2.3) and thus set a limit on the WIMP-nucleon cross sections. For the limit setting, we considered two "signal" components; the aforementioned excess with spectral shape fixed to the global minimum value and free amplitude (s_e) and a traditional WIMP spectrum as a function of mass with amplitude s_χ. This can be thought as interpreting the excess as an unconstrained background. We followed the limit

setting procedure outlined in Ref. [30] where for each fixed mass point, m_χ, we scanned over the number of DM events, s_χ, from the best fit value upwards until the test statistic is > 2.7, which corresponds to a 90% C.L. following the Wilkes' theorem approximation. In the region where the WIMP spectrum is similar to the parametrized excess, the fit can efficiently exchange s_χ and s_e without impacting the test statistic, thus the limit suffers when the two spectra are similar and approaches the sensitivity when the spectra differ. We converted the s'_χ that pushes the test statistic over the threshold to the cross section by

$$\sigma_{\chi-n}(m_\chi) = C(m_\chi)\frac{s'_\chi}{\eta} \tag{2.8}$$

where $C(m_\chi)$ is the efficiency corrected cross section that results in one event / kg / day, s'_χ the number of signal events that the fit can accommodate at 90% C.L., and η the experiment exposure. The resulting limit on the WIMP-nucleon scattering cross section as a function of mass is shown in Figure 2.6. We also show the sensitivity from MC data drawn from the background model.

2.2.2.1 Systematic Checks

We considered a number of systematic checks for our WIMP search. The joint fit disfavored the background only hypothesis (p-value of 2.2×10^{-4}, goodness-of-fit p-value of 0.10), but each data set individually also preferred an excess over the background model. In CCD1 only we found a preference for $s_1 = 6.4 \pm 3.0$ events with decay constant $\epsilon_1 = 89 \pm 50$ $\mathrm{eV_{ee}}$ with $\eta = 1.6$ kg days (p-value of 5.8×10^{-4} and g.o.f p-value of 0.94) and in CCD2-7 find $s_{2\text{-}7} = 8.9 \pm 7.2$ and $\epsilon_{2\text{-}7} = 51 \pm 39$ $\mathrm{eV_{ee}}$ for $\eta = 9.3$ kg days (p-value of 0.039 and g.o.f p-value of 0.21). While the rate is higher in CCD1 (which interestingly has lower background and therefore is more sensitive), the deviation is $\sim 1.5\sigma$, and therefore we considered the two datasets (including spectral shape) consistent. In Figure 2.4, a collection of events around $\sigma_x = 0.2$ is an important driver of the fit; upon inspection of these events, they are predominantly single pixel, or two pixels of equal energy, such that the fit cannot accurately

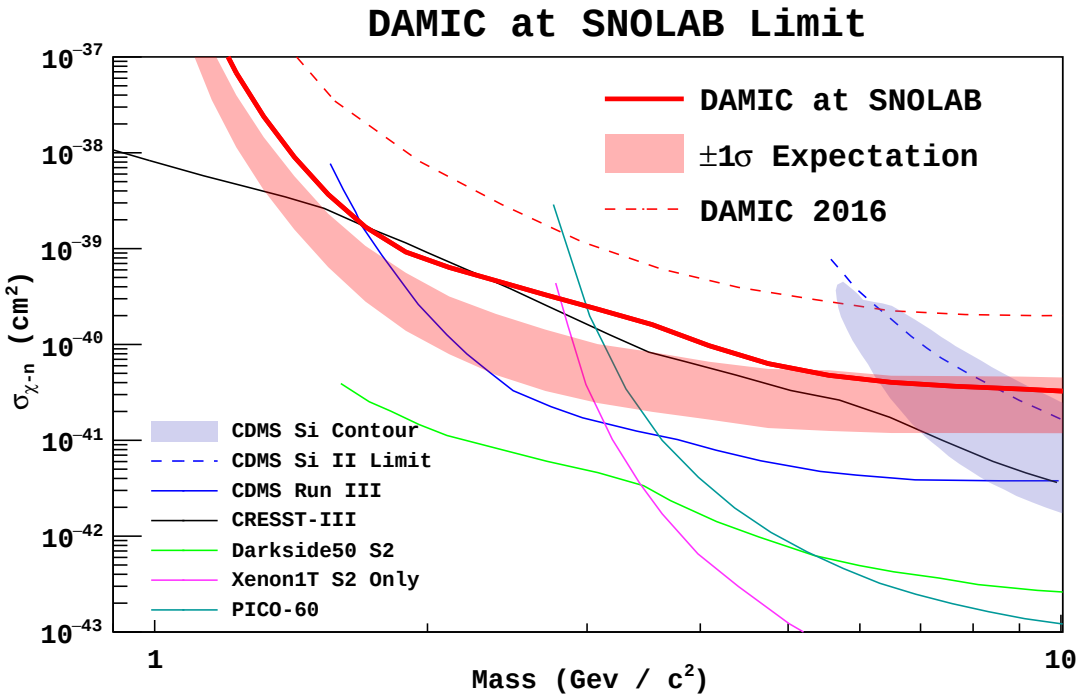

Figure 2.6: DAMIC at SNOLAB 90% C.L. upper limit on the WIMP-nucleon cross section (solid red) and the experimental sensitivity based on MC data generated from the background model (shaded red). The deviation of the limit from sensitivity is most pronounced in mass ranges where the WIMP spectrum has a similar shape to the parametrized excess. Above ~ 6 GeV/c^2 the WIMP spectrum becomes incompatible with the observed excess and the limit falls within the expected sensitivity. Other experimental including CRESST III (black) [43], CDMS II Silicon (blue dashed) [77], CDMS III (blue) [78], Darkside50 S2 only (green) [79], Xenon1T S2 only (pink) [80], and PICO (purple) [81]. Also shown is the DAMIC 2016 limit (dashed red) [35].

reconstruction the proper σ_x. These could be some bulk population or surface events. We added an additional cut to remove events with only one pixel $> 1.6\sigma_n$ which keeps $< 10\%$ of simulated surface events and $\sim 85\%$ of bulk events, making this an efficient front surface cuts. When performing the likelihood fit on this data we found $s = 13.9 \pm 6.8$ and $\epsilon =$

78 ± 33 $\mathrm{eV_{ee}}$ for $\eta = 10.3$ kg days (p-value of 5.1×10^{-3} and g.o.f p-value of 0.69), so the excess remains, suggesting it is not a front surface background. We also considered only events > 200 $\mathrm{eV_{ee}}$ and found no preference for an excess and g.o.f p-value of 0.32, suggesting the background model well describes the data in the region. Finally, we performed the statistical test proposed in Ref. [82] and found no statistically significant fluctuations in the data compared to the background model outside of the lowest energies, further reinforcing the robust nature of the background model.

2.3 Discussion

We ultimately did not claim a dark matter discovery from this result. While there was a statistically significant excess over our developed background model, we had no ability to categorize these events between nuclear or electronic recoils, and thus leave the option for the excess to be an unconsidered background or detector effect.

The limit on the WIMP-nucleon cross section—while not reaching our projected sensitivity due to this unknown excess—still holds scientific value. The limit here is the most stringent for a silicon target for $m_\chi < 9$ $\mathrm{GeV/c^2}$ and for masses above ~ 5 $\mathrm{GeV/c^2}$ we approach our expected sensitivity which further constrained the WIMP interpretation of the CDMS-II Si excess with the same nuclear target [77].

Regardless of the origin, understanding the nature of this population of events is absolutely critical for future CCD dark matter experiments. The next generation of experiments of SENSEI [83], DAMIC-M [84], and OSCURA [85] plan to employ CCD searches with 100 g, 700 g, and 10 kg of target mass with a 5, 0.1, and 0.01 counts / kg / day / $\mathrm{keV_{ee}}$ bulk background rate, respectively. Assuming our observed excess follows the parametrized form down to energies of a few electron, we would expect a rate of ~ 75 counts / kg / day / $\mathrm{keV_{ee}}$ as we approach an energy threshold of a few electrons, which is an energy regime these experiments plan to probe. If this excess is real—either DM or other—it will dominate the event rate in this low energy regime. Therefore it is crucial to gain an understanding of the underlying cause of these ionization events.

Chapter 3

SKIPPER CCDS IN UNDERGROUND LABORATORIES

3.1 Skipper CCDs

The hallmarks of direct detection dark matter experiment are typically large target mass, low radioactive background, and low energy threshold. The next generation CCD experiment, DAMIC at Modane (DAMIC-M), intends to address all three aspects with a large, $\sim$ 700 g, array of skipper CCDs [84][86]. The skipper CCD is a novel alteration to a traditional CCD output stage that allows for nearly arbitrarily low readout noise with repeated, uncorrelated, measurements of the charge in a single pixel, and therefore allows a lower energy threshold than the CCDs discussed in Section 2.2.2.

Skipper CCDs have demonstrated deep sub-electron noise in the laboratory settings and been employed as a single CCD for a light dark matter search. However further work on CCD operation and background control—including understanding the unexplained excess discussed in the previous chapter—are critical for the success of the CCD dark matter program.

The following chapter is dedicated to the fundamentals behind skipper CCD operation and the deployment of four skipper CCDs in two low background systems.

3.1.1 Detector Operation

The charge collection and transport in traditional and skipper CCDs are identical and outlined in Section 2.1; the difference between the two devices are the construction of the output stage. In a traditional CCD, charge is moved from the serial register into a floating diffusion gate, also referred to as the sense node, with some parasitic capacitance that is connected to the gate of the output amplifier. The gate voltage created by this charge changes the

output current, which is measured by the readout electronics. When the pixel readout is completed, a reset potential clears the pixel charge off the amplifier gate, so the charge is gone and we can readout the next pixel. In a skipper CCD, the sense node is separated from the output amplifier gate by an area of high resistivity silicon, and therefore is a "floating gate" and **capacitively coupled** to the output amplifier. The charge from a pixel now induces a charge on this metallic component which, like a traditional CCD, changes the current through this output amplifier. In this case though, by changing the potential of the previous summing and output gate, we can remove the charge from the sense node, preserving the amount of charge originally in the pixel. We can make repeated and uncorrelated measurements of the pixel charge as many times as we want. When finished, a new gate, the dump gate, connects the sense node to the drain potential, which discards the charge. If the distribution of the readout values are independent, identically distributed (I.I.D) Gaussian variables, when summing over all measurements, the mean and variance scale proportionally to N, the number of measurements, which we refer to as "skips." Therefore when we average over the measurement, we recover the original amount of charge in the pixel with a noise of:

$$\bar{\sigma} = \frac{\sigma}{\sqrt{N}} \tag{3.1}$$

and we can suppress the readout noise. An example of this from the sciences runs at SNOLAB (Section 3.2) is shown in Figure 3.1; as we increase the number of skips we average over up to 460, the noise reduces from above 4 e^- down to 0.16 e^-. While we only took 460 skips to optimize the detector for science purposes (Section 3.2.3), this trend has been shown in the lab up to 4000 skips. The trade off for reducing the noise is longer readout time; each skip takes $\mathcal{O}(10\ \mu s)$ and so recording thousands of skips for millions of pixels can result in a readout time of days. This is suitable for the low background, rare event searches discussed in the remainder of this chapter where the skipper CCD technology has opened the avenue for even lower threshold CCD experiments and a probe of additional dark matter parameter space.

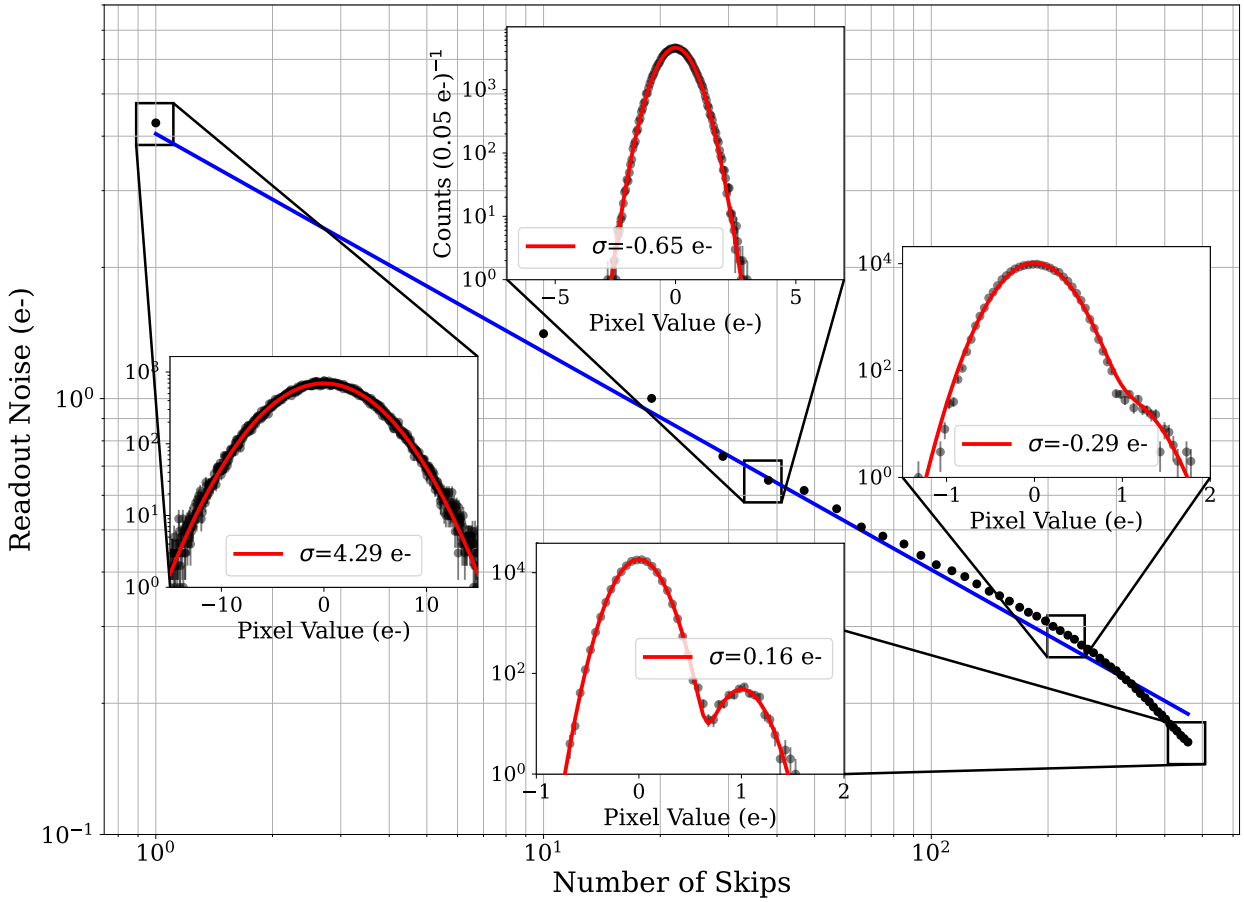

Figure 3.1: Skipper noise performance of a sample image taken at SNOLAB (black points). The noise trend follows $\sim \frac{1}{\sqrt{n_{\text{skips}}}}$ (blue line) where the deviations are a result of some correlated noise in the system. The pixel distribution of the image averaged over different number of skips are shown as the inset plots; the transition from seemingly Gaussian to counting the individual electron peaks is evident in these insets.

3.1.2 Testing and Selection of Underground Detectors

We tested nine candidate CCDs—denoted UW614D-UW6422D—at UW for potential underground deployment in SNOLAB (Section 3.2) and LSM (Section 3.4). The detectors are 6144 columns by 4128 rows CCDs designed at Lawrence Berkely National Lab (LBNL), which will

henceforth be referred to as 6k x 4k detectors. Each sensor includes two skipper and two traditional amplifiers. The two skipper amplifiers are denoted the U (upper) and L (lower) amplifier for each sides of the serial register. The serial register is extended by 8 pixels on each side, called the prescan, which are measured before the pixel array for every row.

In each CCD we verified that the amplifiers worked by observing 1) ionization events from radioactive and cosmic backgrounds, and 2) measuring the individual electron peaks by achieving sub-electron noise with the skipper procedure. We checked that there was no visible charge transfer inefficiencies (CTI) when moving ionization events in the pixel array or serial register. Finally, we mapped the defects of the CCD by creating a median image—an image comprised of the median value of pixel ij across a set of N images—of ~ 20 images with ~ 30 minutes exposures, which filters out ionization events and highlights pixels with persistent charge which is characteristic of defects in the CCD; we aimed to select CCDs with the fewest and least prominent defects. We generally did not optimize the CCDs for shot or readout noise, as this is often dependent on the specific setup and would be addressed during underground commissioning.

We selected UW6421D and UW6422D (UW6414D and UW6415D) for SNOLAB (LSM).

3.2 DAMIC at SNOLAB Upgrade

Given the excess of low energy ionization events observed at SNOLAB, deploying skipper CCDs underground in the same radioactive environment to probe the excess was a natural extension. The following sections detail the detector upgrade, operating conditions, and data analysis for this low energy probe.

3.2.1 Hardware Upgrades

We took two trips to SNOLAB (October and November of 2021) to perform the necessary upgrades on the experiment to run skipper CCDs. We decommissioned the existing detector, moving the CCDs, copper box, and electronics from the experiment into storage. We installed two 6k x 4k skipper CCDs in a new copper box. The copper was stored in SNOLAB for several

years, suppressing the quantity of cosmogenically activated isotopes in the copper [87][88], and brought to the surface for machining; the total surface exposure of each machined piece was < 9 days. We assembled the box with two 6k x 4k CCDs and connected it to the existing cold finger connection to provide cooling to the CCDs. Ancient lead bricks were placed above and below the CCDs to provide additional shielding. In the box, CCD1 is on the bottom and CCD2 is on top; the front surface of both CCDs points in the $+\hat{z}$ direction. Each CCD has two amplifiers, denoted "L" and "U" and we will refer to the four amplifiers with the naming convention 1L, 1U, 2L, and 2U throughout the remainder of this thesis.

We replaced the previous vacuum feedthrough with a new vacuum interface board (VIB) designed at UW specifically for the new CCDs and readout electronics. For readout, we used the Low Threshold Acquisition (LTA) electronics designed at Fermilab for skipper CCD readout [89]. The LTA is an integrated module providing all control and readout components for a single 4-channel CCD; multiple LTAs can be synchronized on the same clock signal in a leader-follower schema allowing low noise readout of multiple CCDs as employed at SNOLAB. We connected the LTA readout to the air side connectors on the VIB board via a 3 m cables with individual coaxial lines for each signal.

We also replaced the cryocooler cold head motor as this was the component that failed and ended the original DAMIC at SNOLAB run.

3.2.2 Detector Commissioning

The detector commissioning focused on minimizing the readout and shot noise (stemming from some detector dark current). Based on tests in the lab, we were confident in the parameters for reading ionization events; however, measuring extremely low dark current (DC) on the surface is challenging and thus we needed additional parameter and operation tuning to achieve the lowest DC possible. This process in reality was highly non-linear, however, the steps and tests summarized here are grouped by topic.

For the noise, we attempted to replicate the original DAMIC at SNOLAB grounding configuration to achieve the same noise. One notable difference in operation is during read-

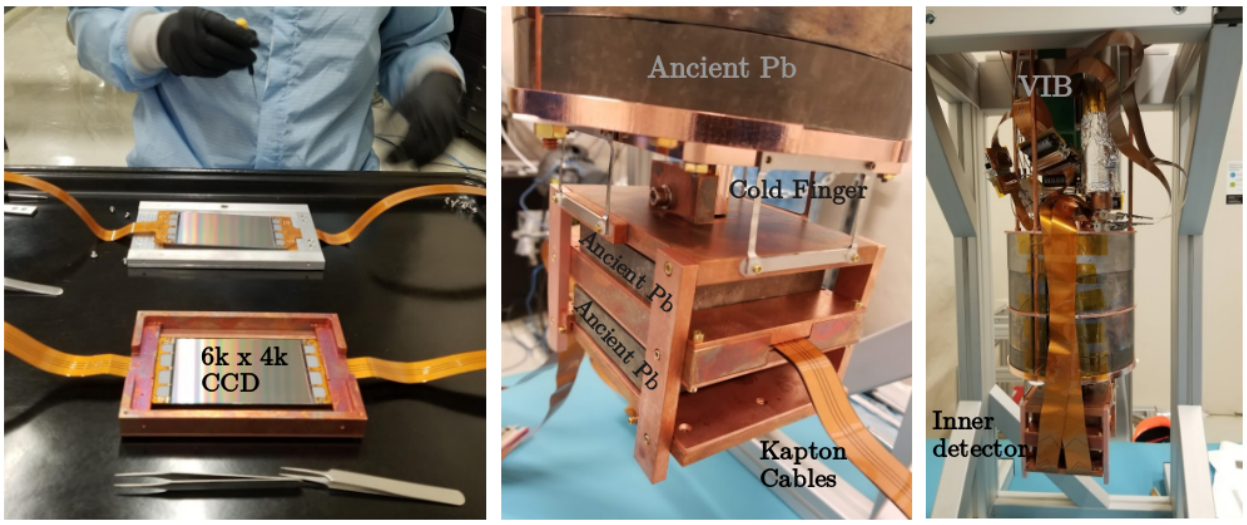

(a) (b) (c)

Figure 3.2: (a) 6k x 4k CCDs being transferred from aluminum storage boxes to the inner detector copper box. (b) CCD box installed on the cryocooler cold finger. Ancient lead bricks are placed above and below the CCDs. (c) DAMIC at SNOLAB detector assembly; the VIB board, CCD connections, and cooling are placed above the lead shielding. This structure is placed in the DAMIC cryostat and surrounded by additional lead and polyethylene shielding.

out, the predecessor experiment turned off the cryocooler to reduce the noise during the relatively quick readout. That was not possible for skipper operation as the readout was continuous. Therefore all commissioning, and eventually science, data was taken with the cryocooler turned on. We measured the single skip readout noise to be between $[3, 6]$ e^-, depending on the integration time.

To minimize the dark current in the CCD pixel array, we performed the following startup procedure. We brought the detector to 160 K and performed a series of erase procedures, which inverted the CCD potentials to clear surface charge and fill "traps" or defects in the CCD, while cooling down in intervals to our science operating temperature of 110 K. In between erase procedures we continually acquired images, which consisted of a clean

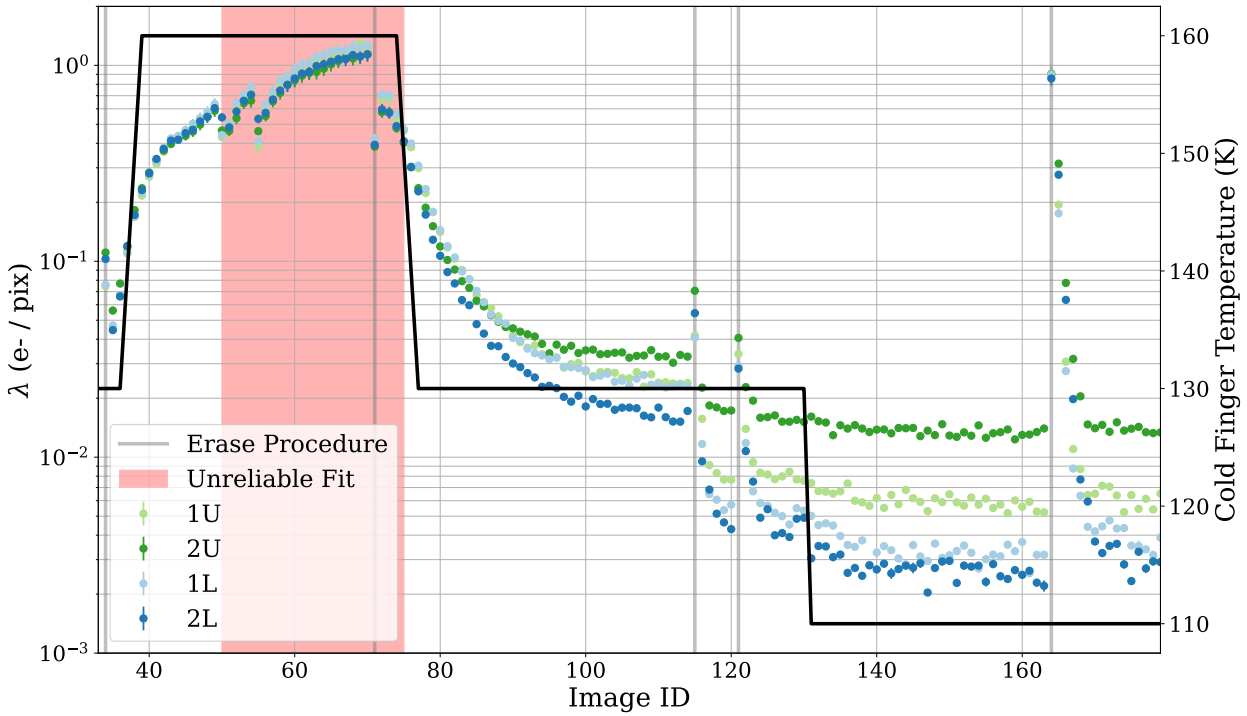

Figure 3.3: SNOLAB cooldown commissioning procedure.

(hardware bin and clock all the charge out of the pixel array as fast as possible, a few seconds), image (1000 skips to measure the dark current, $\sim$ 10 minutes), and idle (continually clock the charge with the same image `hclk` parameters as the image, but do not record the data, 20 minutes) sequence. An example of this procedure with specific erase and cooldown timings, as well as the reduction in bulk dark current, is shown in Figure 3.3. This recipe has proved to result in reliable dark currents between system restarts.

Additionally, we optimized several CCD parameters. We scanned over the difference in the amplifier bias voltage and CCD reference voltage, $V_{\mathrm{DD}} - V_{\mathrm{ref}}$. Previous lab measurements suggest that if the difference in voltages is too negative the current through the amplifier can cause heating/emission of infra-red radiation that appears as a "glow" near the amplifiers. There was no observable difference in the image quality for $V_{\mathrm{ref}} = -7$ V and $V_{\mathrm{DD}} \in [-18, -24]$ V. We took variable length exposures with identical readout times and V_{DD} either On/Off.

The slope of the mean charge per pixel vs. readout time gives the dark current during exposure, i_e. For $V_{\rm DD}$ on (off) the i_e varied from 2.4-3.0 $\times$ 10^{-3} e$^-$ /pix /day (0.5-2.0 $\times$ 10^{-3} e$^-$ /pix /day) between the four amplifiers, perhaps indicating some slight amplifier glowing. However, increasing $V_{\rm DD}$ above -18 V at $V_{\rm ref} = -7$ V reduced the gain, and therefore the SNR, of the amplifiers, which was undesirable. Finally we investigated the clocking parameters and found the values that minimized clock induced charge—spurious charge created due to changes in voltages from the clock signals[90]—while maintaining good charge transfer of the ionization events. Figure 3.4 shows a scan of the ΔV between the high and low clock values vs. the measured charger per pixel for the horizontal and vertical clocks. Each data point has identical readout parameters, except the noted clock voltage, so the relative impact on dark current can be inferred.

The full CCD configuration can be found on the SNOLAB DAQ computer, lilpeep.snolab.ca, at `/home/damic/soft/lta-daemon`.

3.2.3 Science Readout Strategy

Once the detector had been commissioned to optimize shot noise, readout noise, and charge transfer inefficiencies, there were several CCD parameters surrounding the readout that we tuned (integration time, exposure time, number of skips, pixel hardware binning). Our science goal was to probe the unexpected population of low energy bulk events previously observed, and thus we want to minimize our energy threshold and maintain maximum event depth information. Therefore, we limited ourselves to 1×1 hardware binning so we could most easily reconstruct σ_{xy}. We selected our run parameters by minimizing the estimated rate of accidental low energy clusters given the CCD noise performance. The detector noise can be modeled as Poisson shot noise (λ) convolved with a Gaussian readout noise (σ_r), so the probability of measuring pixel value x is

$$f(x|\lambda,\sigma_r) = \frac{1}{\sqrt{2\pi\sigma_r^2}} \sum_{q=0}^{\infty} \frac{\lambda^q e^{-\lambda}}{q!} \exp\left(\frac{-(x-q)^2}{2\sigma_r^2}\right) \tag{3.2}$$

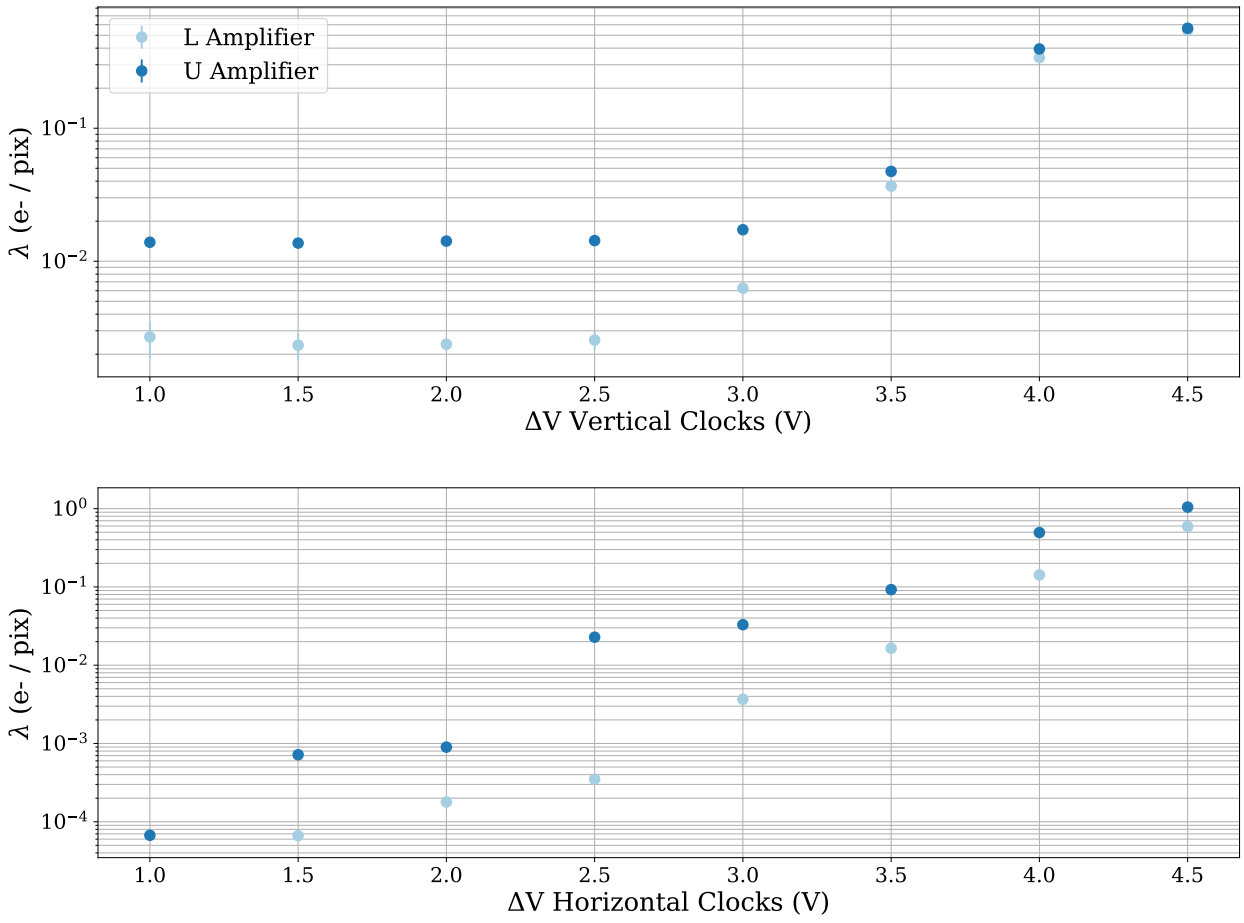

Figure 3.4: Clock swing scan for the vertical (top) and horizontal (bottom) clock voltages.

which is a sum of Gaussian distributions, weighted by the Poisson coefficient of measuring q electrons, given the shot noise. The shot noise can be expressed as a sum of exposure and readout components

$$\lambda = i_r t_r + i_e t_e, \tag{3.3}$$

where i_r (i_e) is the dark current during readout (exposure) and t_r (t_e) the readout (exposure) time[90]. The readout time is

$$t_r = t_p n_p n_s, \tag{3.4}$$

the product of the time to measure a single pixel (t_p), number of pixels (n_p) in the sensor and number of skips (n_s). Ideally, $i_e = i_r$, but due to glowing from the amplifiers or some effect due to clocking, could differ. Furthermore, the readout noise also depends on the number of skips

$$\sigma_r = \frac{\sigma}{\sqrt{n_s}} \tag{3.5}$$

We wanted to minimize the rate of high charge clusters in the images so first computed the probability that a pixel has above a given number of electrons, $\tilde{q}$

$$p(x \geq \tilde{q}) = \int_{\tilde{q}-0.5}^{\infty} f(x'|\lambda, \sigma_r) dx' \tag{3.6}$$

And the total number of pixels with that charge or higher is per kg day

$$N(x \geq \tilde{q}) = n_p p(x \geq \tilde{q}) = \frac{1}{\epsilon_p} p(x \geq \tilde{q}) = \frac{1}{m_p(t_r + t_e n_{\text{bins}})} p(x \geq \tilde{q}) \tag{3.7}$$

Where n_p is the number of pixel read per kg days, which is one over the exposure of a read pixel (ϵ_p), and m_p the mass of a pixel. We were not just concerned with single pixels above a threshold (which is also important), but also composite clusters. We estimated the probability of composites by considering the necessary combinations of charge in contiguous pixels. For example, we included the probability of measuring a single 5 e^- pixel, a 4 e^- touching a 1 e^-, a 3 e^- touching a 2 e^- or two 1 e^- pixels, etc. to estimate the rate of 5 e^- clusters.

With this formalism, we investigated how the dark current, number of skips—and therefore noise and readout time—affected the number high charge clusters. We began with the case of continuous readout, that is $t_e = 0$ s, which should minimize the shot noise, and computed the noise cluster rates for a range of integration times $\in [4, 20]$ μs and for dark currents $\in [10^{-3}, 10^{-1}]$ e^- / pix / day. We found that an 8 μs integration time resulted in the lowest rate of 5 e^- noise clusters. An example of the pixel probability and cluster rate per kg day for an 8 μs integration time are shown in Figure 3.5.

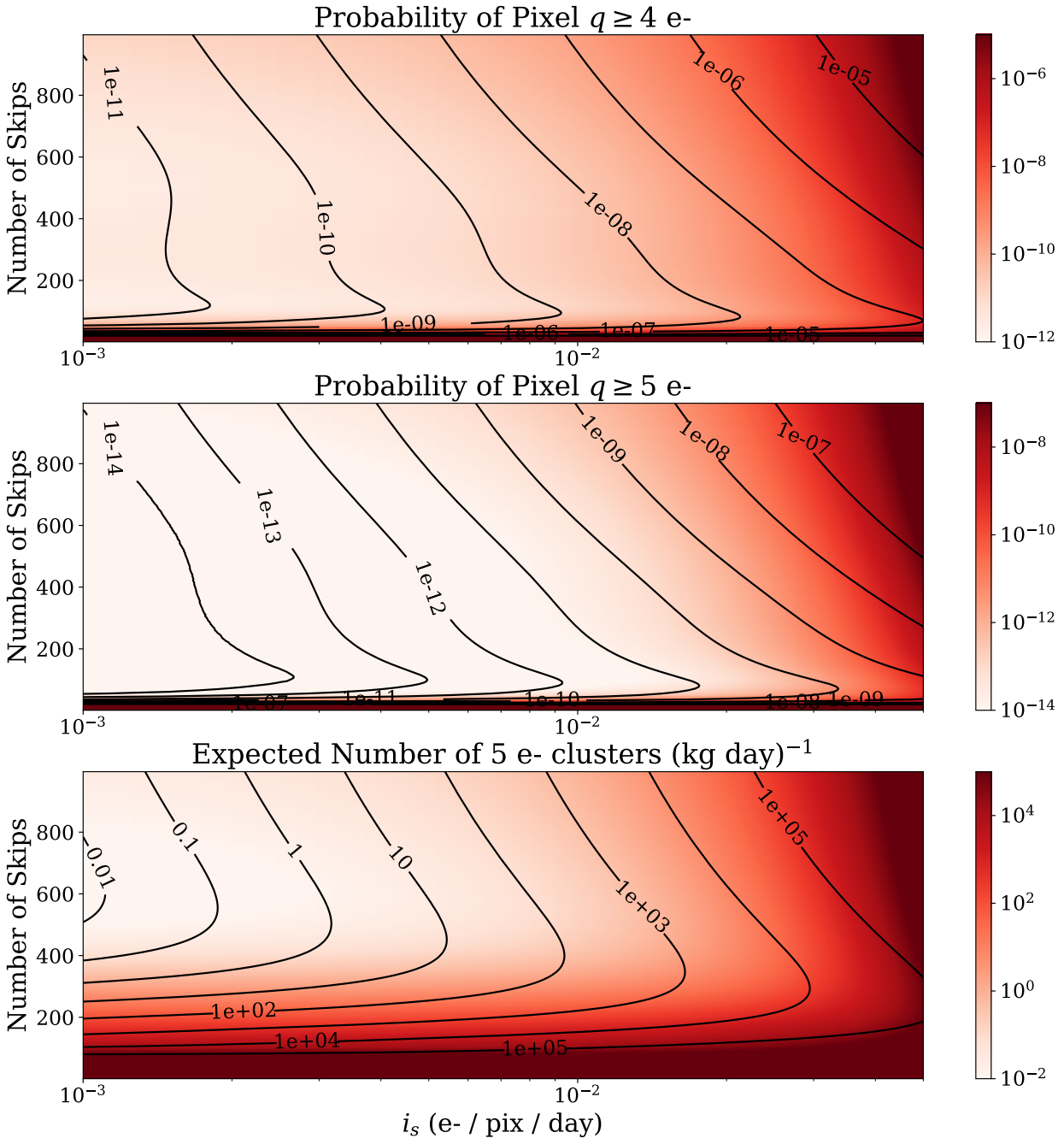

Figure 3.5: Pixel probability above 4 e^- (top) and 5 e^- (middle) along with the estimated rate of 5 e^- clusters (bottom) for a 8 μs integration time. The details of the calculation are included in the text.

At low number of skips, the rate is dominated by pixels above threshold due to the high readout noise. As more skips are measured and the readout noise is suppressed, the probability of high charge clusters becomes dominated by the increasing shot noise. For a given dark current, there is an optimal number of skip that minimizes noise clusters. For increasing dark current, the rate of noise cluster increases rapidly, emphasizing the necessity to minimize the detector dark current for low energy dark matter searches.

As mentioned, and evident from Eqn 3.3, shot noise (λ) is minimized with no exposure time. However, we considered the case where the exposure dark current (i_e) is much smaller than the readout dark current (i_r), and the increased shot noise could be offset by the increase in exposure per pixel and therefore decrease the require n_p. However, based off the i_e and i_r measured in the SNOLAB CCDs, continuous readout was optimal, and thus we used $t_e = 0$ s.

Finally, to determine the optimal number of skips, we can take slices in the dark current of Figure 3.5c to minimize 5 e^- for different dark currents. We found that 460 skips per pixel was optimal for the science runs.

As a note, the likelihood clustering described in Section 3.3.6 is significantly more complicated than this toy estimation and will cluster other combinations of charge; however, in the case of likelihood clustering we also have discrimination between Gaussian (real) and uniform (noise) clusters, so the pure rate of clusters is not the only metric that matters. Therefore, this estimation is useful for the determination of the readout configuration to limit accidentals from noise.

3.3 DAMIC at SNOLAB Upgrade Science Data

The following sections detail the data taken at SNOLAB and the analysis procedure to investigate the low energy regime from the skipper CCD data.

Run	Start Date	End Date	# Images	Exp (g days)	Hclks (V)	Image size
Run0	2022-02-25	2022-04-05	363	651.4	[-2.75, 0.5]	$210 \times 3100 \times 460$
Run1	2022-04-07	2022-04-27	189	330.5	[-2.75, 0.5]	$210 \times 3100 \times 460$
Run2	2022-05-25	2022-08-21	791	1518.3	[-2.0, 1.25]	$210 \times 3300 \times 460$
Run3	2022-08-25	2022-09-05	102	179.5	[-2.75, 0.5]	$210 \times 3300 \times 460$
Run4	2022-09-09	2022-10-24	399	753.1	[-2.0, 1.25]	$210 \times 3300 \times 460$
Run5	2022-11-02	2022-12-15	405 (371)	747.2	[-2.0, 1.25]	$210 \times 3300 \times 460$
Run6	2022-12-22	2023-01-25	301	563.3	[-2.0, 1.25]	$210 \times 3300 \times 460$

Table 3.1: Run summary. Generally parameters remained the same, though we did vary the `Hclk` low and high voltage (while maintaining the same ΔV) to improve the clock induced dark current. The listed exposure is the raw exposure of all images and does not include quality cuts. The Run5 "# Images" shows the number acquired with CCD1 (CCD2).

3.3.1 Science Run Summary

We began data collection February 25th, 2022 and continued until January 25th, 2023. We performed 7 data runs, Run0-6, that were typically ended by some DAQ interruption or system warm-ups from power interruptions or hardware failures.

Data was acquired locally at SNOLAB and copied over to UW for further processing. A mirror of the raw data is kept on site at SNOLAB.

The summary of runs is included in Table 3.1 and the cumulative exposure shown in Figure 3.6. The pixel exposure time was 49.6 (52.39) hours for the runs with 3100 (3300) columns during continuous readout.

3.3.2 Image Preprocessing

We began by compressing the multi-skip image into an "average" image, that is, the pixel value at ij

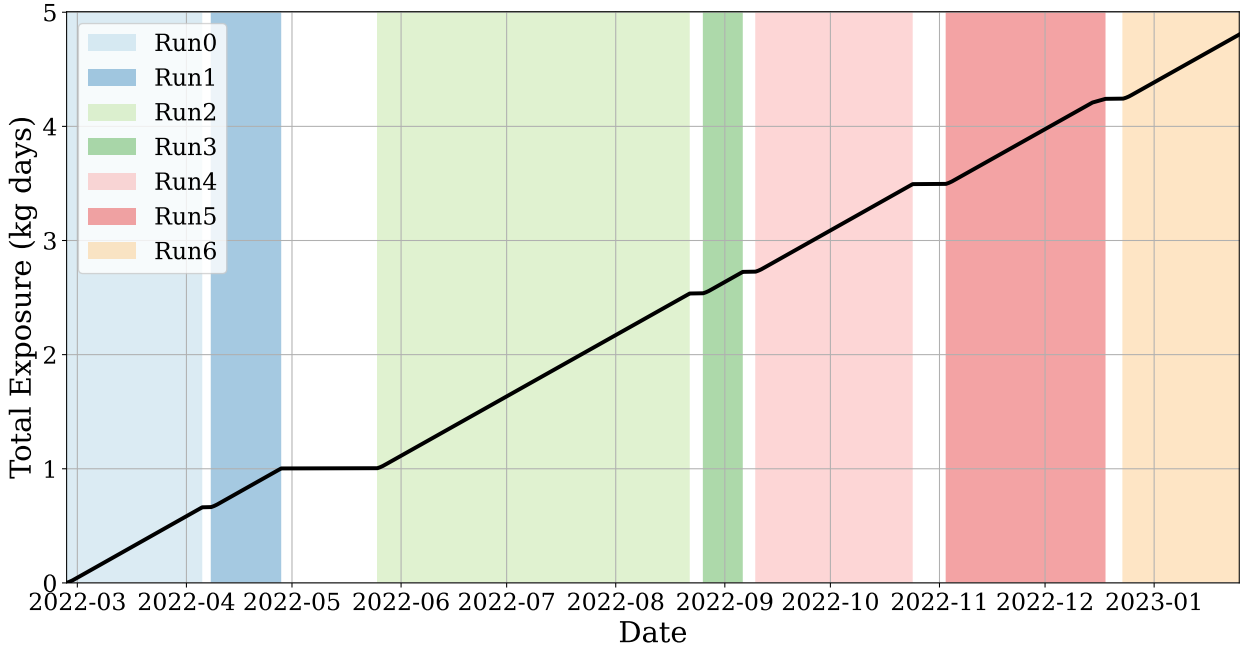

Figure 3.6: Cumulative raw exposure of the SNOLAB upgrade experiment. The separation of runs were typically caused by interruptions in data acquisition that resulted in a warm-up or restart of the data (power outages at SNOLAB, computer hardware failures, etc.). We reached a total exposure of 4.81 kg days.

$$p_{ij} = \sum_{k=2}^{n_s} \frac{p_{ijk}}{n_s - 1}, \tag{3.8}$$

is the mean of that value of the n_s skips taken of that pixel, excluding the first skip due to an electronic transient from moving charge from the serial register to the sense node. We observed a very slowly shifting baseline in the average image, the period being on the order of several tens of rows. To accommodate this, we subtracted the row median value from every pixel in row to achieve white noise throughout the image.

Finally, we fit the image pixel distribution with the convolution of Poisson and Gaussian function

$$F(x|N,\lambda,\sigma,k,C) = \frac{N}{\sqrt{2\pi\sigma^2}} \sum_{i=0}^{\infty} \frac{\lambda^i e^{-\lambda}}{i!} \exp\left(\frac{(x-C-ki)^2}{2\sigma^2}\right), \tag{3.9}$$

where N is the number of pixels in the image, λ the mean charge per pixel, σ the Gaussian readout noise, k the calibration constant (ADU / e^-), and C an offset in the x-axis. We left all parameters free, though constrained to physical values. Since λ is small, in the fit we summed over $i \in [0, 10]$, which is an excellent approximation for the true Poisson distribution. After the median column subtraction, the offset (C) is typically small, $\sim \lambda k$, but should still be included in the calibration. We subtracted the offset and divided by the calibration constant k such that the pixel values were calibrated in units of charge.

We vertically concatenated 40 average images into a joined image with 8400 rows $\times$ 3300 (3100) columns. This reduced the likelihood that an ionization event could be split between images for the later analysis.

3.3.3 Image Selection

Shifters were responsible for monitoring image quality everyday during science DAQ. They monitored the image pixel distribution, noise, calibration constant, appearance of hot column, and manually inspected all images taken that day. Any image with unexpected behavior, such as excessively high charge or artifacts in the image, were flagged and excluded from the final analysis. These images were highly correlated with power instabilities at SNOLAB.

In addition to the visual inspection of images, we rejected images whose calibration constants, k, were further than $\pm 3\sigma$ of the mean value for the given amplifier and data run. Figure 3.7 shows the distribution of k values as well as the per run cut applied. We made no selection on the amplifier readout noise. We did not change the experimental setup during the DAQ period, and therefore the fluctuations in the noise of Figure 3.7 are related to an external noise source. The period of high noise in the U amplifiers corresponds to a time of known electrical instability at SNOLAB. The noise fluctuations were accounted for in our simulations and therefore did not require a cut.

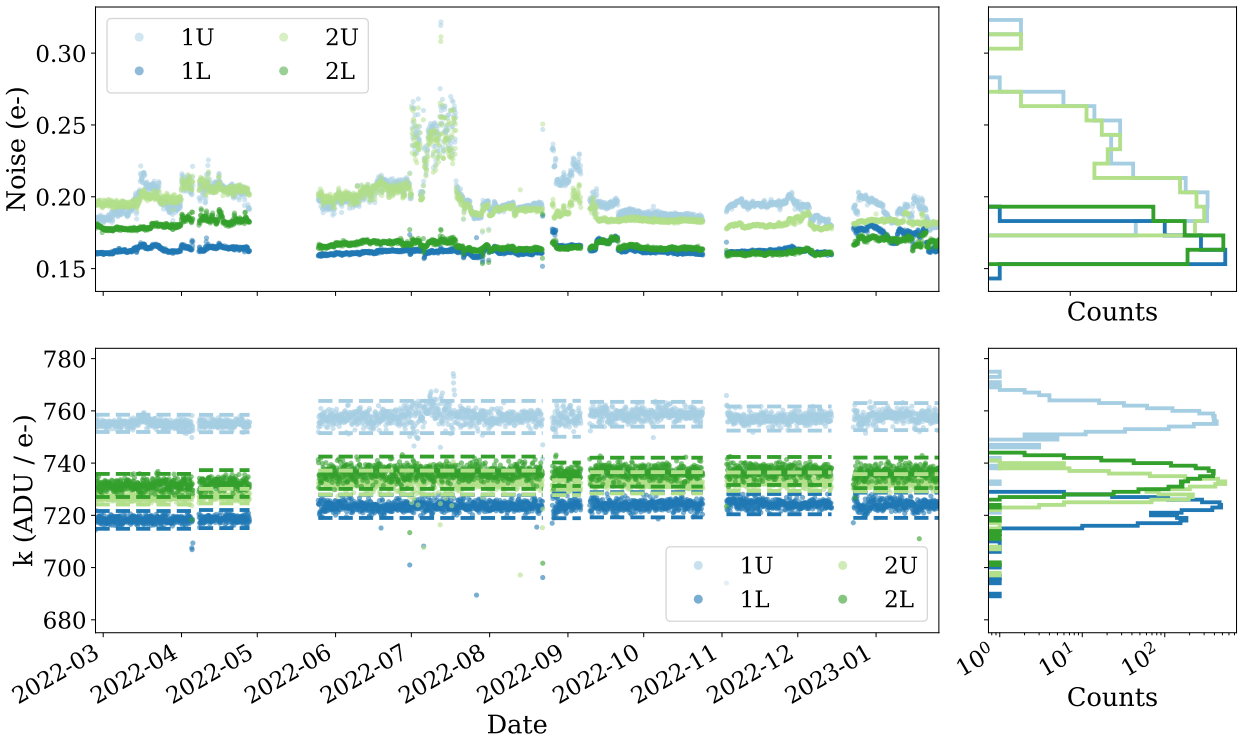

Figure 3.7: Noise and calibration constant of all image taken across science runs.

3.3.4 Mask

3.3.4.1 Column Mask

Defects in the silicon lattice are possible—for example from the displacement of atoms from incident radiation [91][92]—and can alter the local band gap of the material causing charge generation or increased leakage current at the defect site [93][94]. These regions of higher charge are spatially localized to a single point, which is inconsistent with a dark matter signal expected to interact uniformly throughout the detector, and therefore must be excluded from consideration in a dark matter search.

To create the mask, we generated a "λ map" per amplifier per science run by fitting the pixel distribution of column x_i to the noise function defined in Eqn 3.2 to extract the λ value of each column. We masked any isolated column with $\lambda_i > 0.035$ e$^-$ / pixel as well as any

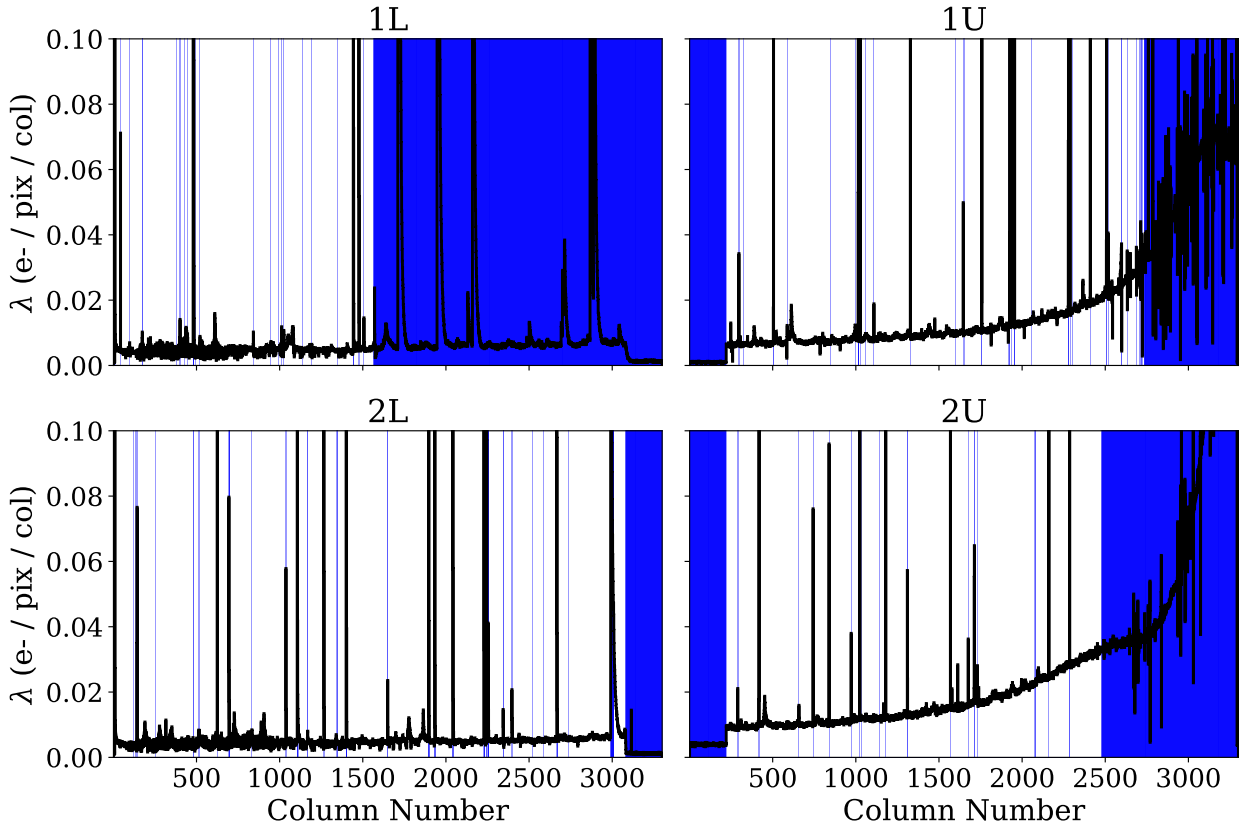

Figure 3.8: Run4 column mask for all CCD halves. Blue shaded regions are masked due to the criteria outlined in the text. Red shaded regions represent the CCD overscan.

region where the baseline charge per pixel—defined as the median λ of columns in the range $x_i \pm 100$—was above 95% of the listed threshold. We also masked columns where the charge distribution was poorly described by a Poisson distribution by excluding columns where the χ^2 is outside the $\pm 4\sigma$ distribution of all χ^2. Finally we exclude columns > 1565 in the 1L due to a distortion of events that we believe to originate from a charge trap in the serial register that skews clusters in the region to the right. The resulting mask for Run4 is shown in Figure 3.8.

We cross checked the masked columns with the x position of defects identified at high temperatures. At a cold finger temperature of 160 K, defects are much more "active" and

we can observe them with 30 minute exposures and 1×1, single skip readout. We acquired > 10 images at this temperature and generated a median image to filter out ionization events that were only present in a single image vs. the defects that were persistent throughout all. We defined the defects as pixels with $> 5\sigma$ the readout noise and grouped contiguous pixels into defects. The x location between this data set shows excellent agreement with the hot columns identified in the science data (the science data has no y position due to continuous readout), suggesting that using the science data to create the mask is not biasing.

Finally, we allowed for the possibility of an hot, non-Poissonian column escaping the previous selection. We therefore also excluded any column with an upward fluctuation 30% higher than the baseline value that also coincides with a defect found at higher temperatures.

3.3.4.2 Ionization Mask

Additionally, we defined a high energy ionization mask of clusters > 10 $\mathrm{keV_{ee}}$. Clusters were defined as touching groups of pixels ≥ 3 $\mathrm{e^-}$. The total charge was the sum of all pixel in the cluster and converted to total energy with an ionization efficiency of 3.8 $\mathrm{eV_{ee}/e^-}$ [69]. We masked a box in the range $[x_{\min} - 2, x_{\max} + 2, y_{\min} - 2, y_{\min} + 2]$ around the extent of the cluster. We also added an additional mask of 800 (100) pixels horizontally for the L (U) amplifiers and 20 pixels vertically in the direction opposite to charge transport. This removed potential trailing charge from high energy ionization events. We observed larger sporadic tails of clusters in the L amplifiers than the U amplifiers—likely due to different efficiency of the horizontal clocks—so placed a more conservative mask on the L amplifiers.

We observed an $\mathcal{O}(10^{-4})$ amount of cross talk between amplifiers, meaning high charge density event read out of one amplifier could populate the others with a few electron events. While this is mostly relevant for α events that have the highest charge density, we conservatively masked all pixels readout simultaneously to a pixel included in the ionization mask above.

Cut	Cut Efficiency			
	1U	1L	2U	2L
Bad Image	0.992	0.977	0.990	0.984
Column Mask	0.729	0.495	0.652	0.897
Ionization Mask	0.998	0.994	0.997	0.988
Noisy Pixels	$\mathcal{O}(10^{-6})$	$\mathcal{O}(10^{-6})$	$\mathcal{O}(10^{-6})$	$\mathcal{O}(10^{-6})$
Edge Mask	0.998	0.998	0.998	0.998

Table 3.2: Cut efficiency per amplifier.

3.3.4.3 Other Masks

When we computed the average pixel value across skips, we also computed the pixel root mean squared (RMS) value. We found that occasionally pixels had high RMS values, $\mathcal{O}(10^6)$ ADU compared to the nominal value of $\mathcal{O}(10^3)$ ADU, due to a single bad skip value that also skewed the average pixel value. Therefore we excluded any pixel with RMS $> 10,000$ ADU.

Finally we masked the edges around the images, 10 pixels in the x-direction and 5 pixels in the y-direction. The efficiency of the masking is described in Table 3.2. However, the cuts were not necessarily independent and the joint efficiency applied to simulated clusters is included in Section 3.3.8.

3.3.5 Background Rates > 0.5 keV$_{\text{ee}}$

We investigated the radioactive backgrounds > 0.5 keV$_{\text{ee}}$, which are outside the region of interest of the previously observed low energy excess. In the average images, any group of contiguous pixels, each with charge ≥ 3 e$^-$, was considered a cluster. The sum of the charge in all pixels of the cluster was converted to energy using a constant ionization factor of 3.8 eV$_{\text{ee}}$/e$^-$, which is an excellent approximation at this energy scale [95]. We used the

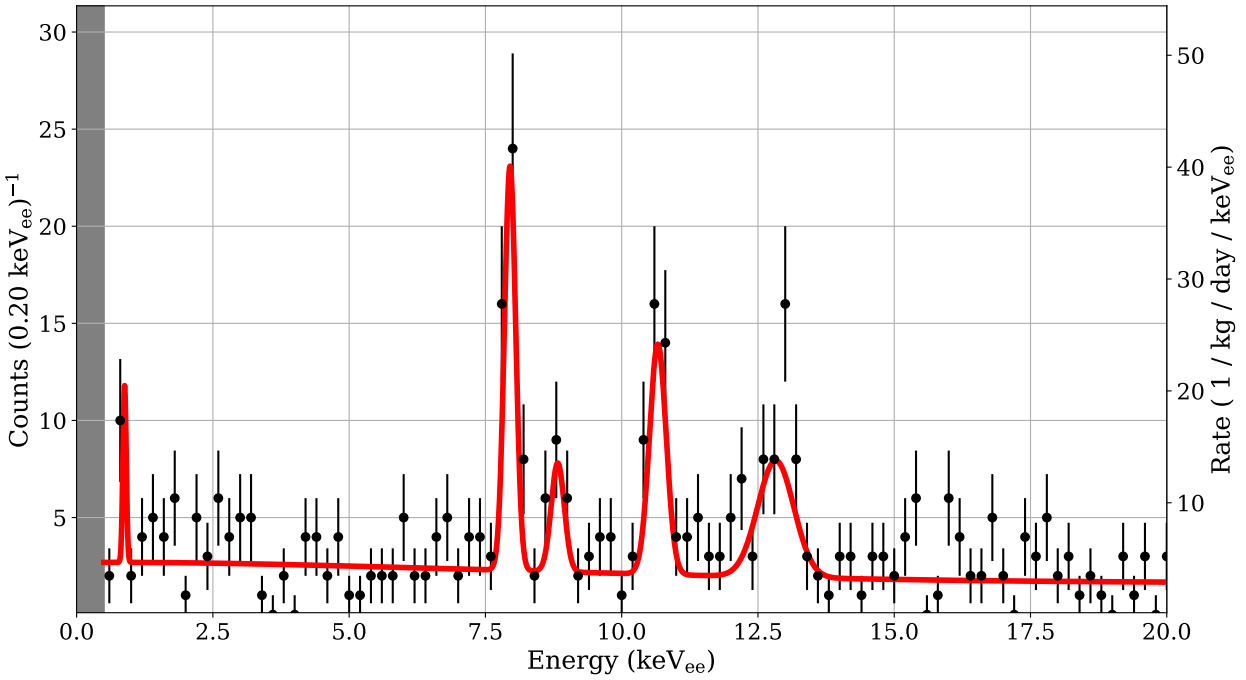

Figure 3.9: The bulk (after σ_y cuts) background rate above 0.5 keV$_{ee}$ for a bulk exposure of $\sim$ 3 kg days.

location of clusters in this course search to perform a fine search on clusters within the energy cuts, $E \in [0.5, 20]$ keV$_{ee}$, where we summed all pixels of the average image in the extent of the cluster ± 1 pixel. This captured any diffuse halo missed by the ≥ 3 e$^-$ threshold.

We applied a bulk fiducial cut on the cluster RMS in the y-direction, σ_y, by considering clusters with $\sigma_y \in [0.25, 1]$ pixels. We estimated the efficiency of this selection by applying it to simulated Gaussian events following the diffusion relationship, $\sigma_y(z) = \sqrt{-A \ln(1 - bz)}$ in Section 3.13. The bulk spectrum is shown in Figure 3.9.

We fit the bulk spectrum to the function

$$f(E|C, b_{trit}, \vec{b_\gamma}, \vec{\mu_\gamma}, \vec{\sigma_\gamma}) = C + b_{trit} f_{trit}(E) + \sum_i^4 b_i \text{Gaus}(E|\mu_i, \sigma_i), \tag{3.10}$$

where C is a constant to model Compton scattering backgrounds, b_{trit} is the number

of ^{3}H events with shape f_{trit}, following the analytic expression in Ref. [96], and a sum of Gaussians to model the intrinsic Na line as well as external Cu and Pb x-ray lines, most likely originating from ^{210}Pb decays in the copper box. We left the amplitudes and widths of the peaks free, and constrained the means to ± 0.5 keV$_{\text{ee}}$ of the literature values.

We measured the bulk background rate between $[1, 6]$ keV$_{\text{ee}}$ to be 5.2 ± 0.6 counts/kg/day/keV$_{\text{ee}}$.

3.3.5.1 α Rate

We leveraged the cluster topological information to discriminate α particles from other high energy β or γ interactions. Using the clusters discussed above, we introduced two additional variables initially used in references [97] and [98]: f_{pix}, the ratio of pixels with charge above threshold to total number of pixels in a bounding box around the cluster; and σ_x/σ_y, the ratio of the cluster variance in the x and y direction. The cuts of $E > 2$ MeV$_{\text{ee}}$ and $f_{\text{pix}} > 0.5$ effectively separated the high energy density α particles from the spread out, "worm" like βs. We further separated the α particles into bloom—vertically elongated originating near the front surface where the local electric field pushes charge over the potential barrier created by the vertical clocks—and plasma—circularly symmetric diffused clusters from the back surface—with a $\sigma_x/\sigma_y < 0.9$. The population of events in this parameter space is shown in Figure 3.10.

The α rate and their distribution on the relative surfaces of the CCD tells us important information of the radioactive backgrounds in this experiment. Table 3.3 contains the α rate for different scenarios. We observed an excess of αs < 5.3 MeV$_{\text{ee}}$ on the CCD surface that faces the copper box compared to the previous DAMIC setup. These were most likely the αs from ^{210}Po decay originating from ^{210}Pb in the copper box. Additionally, we found the rate of these αs was constant between science runs, indicating that the ^{210}Pb and ^{210}Po were in secular equilibrium.

We also found several clusters > 5.3 MeV$_{\text{ee}}$. We inspected the events a found traditional αs (or possibly multiple αs where the decay time is less than the time to clock the number

	α Rate (10^{-3} / cm^2 / day)							
	Run 0		Run 4		$E < 5.3$ MeV		$E > 5.3$ MeV	
	Front	Back	Front	Back	Front	Back	Front	Back
1L	7.7 ± 3.8	9.6 ± 4.3	7.6 ± 3.8	9.5 ± 4.2	4.2 ± 1.1	15 ± 2	0	0
1U	3.8 ± 1.9	28 ± 5	2.5 ± 1.4	19 ± 4	2.5 ± 0.6	18 ± 2	0.6 ± 0.3	0.3 ± 0.2
2L	32 ± 6	3.8 ± 1.9	36 ± 5	5.0 ± 2.0	28 ± 2	3.9 ± 0.7	1.5 ± 0.5	0.1 ± 0.1
2U	41 ± 7	5.2 ± 2.3	19 ± 4	4.3 ± 1.9	28 ± 2	3.7 ± 0.7	1.3 ± 0.5	0.2 ± 0.2

Table 3.3: α rate. The rates for αs above and below 5.3 MeV$_{\text{ee}}$ consider all data runs. This energy range is selected to roughly differentiate αs originating in the copper surfaces, most likely ^{210}Po, from dust or impurities on the CCD surfaces.

of rows the cluster extends, $\sim$ 70 rows or $\mathcal{O}(10)$ min) or composite $\alpha + \beta$ events. In the case of coincidence, these events must originate from the same location on the CCD surface, likely from some dust containing ^{238}U or ^{232}Th. The coincident decays could be a fast chain of decays such as $^{218}\text{Po} \rightarrow {}^{214}\text{Pb} \rightarrow {}^{214}\text{Bi}$. The high energy could also be single αs from a few candidates in the ^{238}U or ^{232}Th chain. Furthermore, we noted a higher coincidence in the x position between the high energy αs and particles > 2 MeV$_{\text{ee}}$ ($\mu = 2.1$) compared to random x coordinates ($\mu = 0.9$) further supporting that these events are contamination on the CCD surfaces.

3.3.6 Likelihood Clustering

For the low energy analysis, we performed a likelihood clustering algorithm similar to the one defined in Ref. [35], to efficiently find Gaussian distributed charge—as expected from bona fide ionization events—over the detector noise. We defined the expected pixel value, $\bar{q}(i, j)$, as the sum of Poisson shot noise and a Gaussian cluster centered at (μ_x, μ_y):

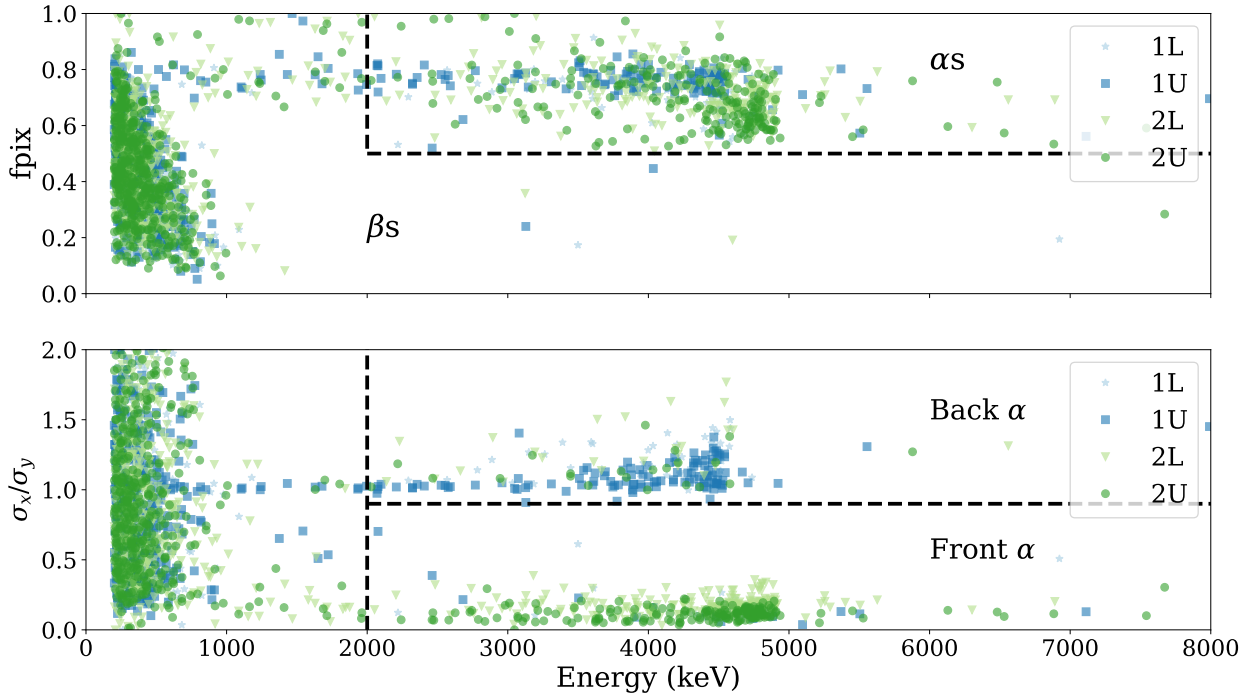

Figure 3.10: High energy particle fpix and σ_x/σ_y parameter space including the cuts for α vs. β discrimination

$$\bar{q}(i,j) = \lambda_i + N \int_{i-0.5}^{i+0.5} \int_{j-0.5}^{j+0.5} \text{Gaus}(x, y|\mu_x, \mu_y, \sigma_x, \sigma_y) dx dy \tag{3.11}$$

where i is the image column number, j the row number, λ_i is the shot noise at the column derived from the λ mask, N is the total charge in the cluster, μ_x (μ_y) are the mean x (y) position, and $\sigma_x = \sigma_y = \sigma_{xy}$ is the cluster variance.

We constructed a likelihood function from these pieces assuming the probability of measuring k electrons in a pixel follows a Poisson distribution with a mean $\gamma_{ij} = \bar{q}(i,j)$ convolved with a Gaussian with readout noise σ_r

$$\log \mathcal{L}(N, \vec{\mu}, \vec{\sigma}, \lambda, \sigma_r|\vec{q}) = \sum_i \sum_j \left(\sum_k^{\infty} \log \left(\frac{\gamma_{ij}^k \exp(-\gamma_{ij})}{k!} \frac{1}{\sqrt{2\pi\sigma_r^2}} \exp\left(\frac{-(q_{ij}-k)^2}{2\sigma_r^2} \right) \right) \right) \tag{3.12}$$

In reality we only summed over the k values near the expected value as those are the ones that contributed meaningfully to the likelihood.

To cluster, we scanned a 5×5 pixel window throughout the image and computed the likelihood that the pixels in this region come from noise ($\log \mathcal{L}_n$, or N=0) and noise plus a Gaussian distributed charge ($\log \mathcal{L}_g$) where μ_x and μ_y are fixed to the center of the region, N is the sum of all pixel values in the window, and $\sigma_x = \sigma_y = \sigma_{\max}/2$. Once we found a region where $\log \mathcal{L}_g - \log \mathcal{L}_n > 7$, that is there is a preference for a Gaussian cluster over the noise only hypothesis, we varied the window position until the above quantity was maximized. We fixed the window and performed a fit to minimize the $-\log \mathcal{L}_g$, leaving the cluster amplitude, position, and spread as free parameters. These fit parameters defined the cluster properties with N being the energy estimate of the cluster.

In the later sections, we rely heavily on the test statistic

$$\Delta LL = -(\log \tilde{\mathcal{L}}_g - \log \mathcal{L}_n) \tag{3.13}$$

where $\tilde{\mathcal{L}}_g$ is the likelihood using the cluster best fit parameters discussed above. This variable, as mentioned above, is an indication of how much the window under consideration prefers a Gaussian component . The more negative this value, the more preference for the Gaussian cluster component. Generally, the larger N, the more negative this value as it becomes increasingly unlikely that a fluctuation in the Poisson shot noise could explain the charge in the pixel. Additionally, smaller σ_{xy} also trend with more negative ΔLL values as the charge of the cluster is spread over fewer pixels, and therefore the cluster has a higher charge density and again the Poisson fluctuations struggle to explain it. Finally, the smaller underlying shot noise, λ_i, the more negative ΔLL values for the same reason.

3.3.7 Cluster Selection

We applied the following criteria on clusters to be considered legitimate ionization events.

3.3.7.1 Valid

We defined a cluster as valid if the cluster:

1. Comes from a good image (see Section 3.7).

2. Does not contain any masked pixels in the 5×5 search window.

3. The cluster mean x and y values are within 1.2 pixels of the fit window center x and y (i.e. the cluster is relatively well centered in the window).

4. Both σ_x and σ_y are less than the maximum fit value of 1.5 pixels (we expect the maximum $\sigma_{xy} \sim 1$ pixel).

Once all conditions are met, the cluster was considered valid.

3.3.7.2 ΔLL Cut

3.3.7.2.1 Data vs. Blanks We relied on the "blank" images to create the ΔLL cut. A blank is a noise only image, that is Poisson shot and Gaussian readout noise, for every real image acquired. We used the same image size to improve the ease of comparison. We used the column λ map, $\lambda(x)$ from Section 3.3.4.1 as the value of the Poisson parameter for each column in the blank images, so spatial variations in the noise was considered. We added Gaussian noise with a σ_r of the real image to which the blank was associated. It was critically important that we verified that the blanks were a good model of the real image noise.

To compare the noise like distributions between data and blanks, we inspected the distribution of clusters with $q \leq 10$ e$^-$ and $-25 < \Delta LL < -10$. While it was possible there were real ionization events with these parameters, it is relatively unlikely, and should be sub-dominant to the noise clusters. When using a single average $\bar{\lambda}(x)$ value to describe the shot noise for a column in a science run, we found a poor agreement in both the rate of noise

clusters and charge spectrum. We noticed a clear transient in the noise cluster rate over the science runs, accentuated during periods immediately after a power outage at SNOLAB where we know the temperature of the detector slightly increased. We therefore speculate that small changes in the temperature of the detector caused a fluctuation in the dark current value, which is then poorly described by an $\bar{\lambda}(x)$.

To correct for this, we performed a scaling of the λ map on an image-by-image basis. First we performed the clustering on a set of blanks with all λ maps scaled by a global factor $s \in [0.8, 1.2]$ and computed the mean number of noise clusters matching the above criteria, $\bar{N}_{noise}$. The function $\bar{N}_{noise}(s)$ was well parametrized by a quadratic fit.

From here, given the $\bar{N}_{noise}$ of each real image, we computed the necessary scaling factor of the blank to match this number. We then processed the ith image with a new λ map, $s_i\lambda(x)$ to account for the transient in the CCD dark current. The scale factors varied between ± 0.15 of the nominal value of one, with scaling values as high as $s = 1.4$ during the periods of known temperature increases mentioned above. While this is an approximation, after this correction, we observed excellent agreement between $\bar{N}_{noise}$ (by construction), cluster μ_x, and charge spectrum between the blanks and data, as shown in Figure 3.11.

This agreement—particularly in the charge spectrum—gives us good confidence in our noise model. This is important for getting the ΔLL cut in the next section correct. All future components of this thesis use the scaled λ maps.

3.3.7.2.2 ΔLL Cut Value We leveraged the ΔLL value of the cluster as a powerful discriminator of the topological information of uniform charge from shot plus readout noise vs. Gaussian distributed charge from real ionization events in the detector bulk. We set a target accidental cluster rate $R_a < 0.01$/kg/day integrated across the charge range $[5, 11]$ e^-.

We performed the likelihood clustering on a set of 30 kg days worth of blank images to get a distribution of noise (or accidental) events found under the noise only hypothesis. From simulation, we only observed noise cluster of any ΔLL value for $q \leq 10$ e$^-$. The rate of accidentals and the acceptance, α of noise values for a given ΔLL cut both depend on

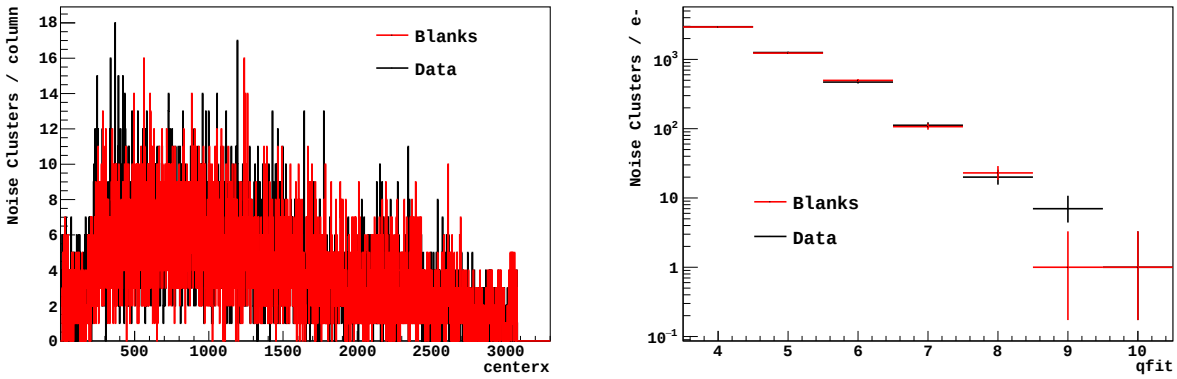

(a) Cluster `centerx` comparison.

(b) Cluster charge comparison.

Figure 3.11: Comparison of noise like distributions between data and blank images after including the λ scaling correction. We see good agreement in both the (a) x position of the clusters and (b) the charge spectrum of noise like events.

the underlying λ value, which spatially varies over the CCDs and temporally varies between images.

Thus for a given charge value, we select the ΔLL to satisfy the condition

$$\int R_a(q,\lambda)\alpha(\Delta LL,\lambda|q)P(\lambda)d\lambda < \frac{R_a^{\text{thresh}}}{\Delta q} \tag{3.14}$$

where $P(\lambda)$ is the probability of observing a region with λ. We enforced an equal contribution to the accidental rate from each charge bin and set a separate ΔLL cut for each bin. We kept clusters with ΔLL below the cut as a function of charge shown in Figure 3.12.

3.3.7.3 Depth Fiducialization

We calibrated the diffusion response of the 6k x 4k sensors similar to Ref. [35] and [98]. In a surface lab, we acquired images with 10 skips, resulting in an average image with $\mathcal{O}(1\ \text{e}^-)$ of electronic noise. We acquired images with $V_{\text{ref}} = -8$ V and $V_{\text{sub}} = [60, 70, 80]$ V. At

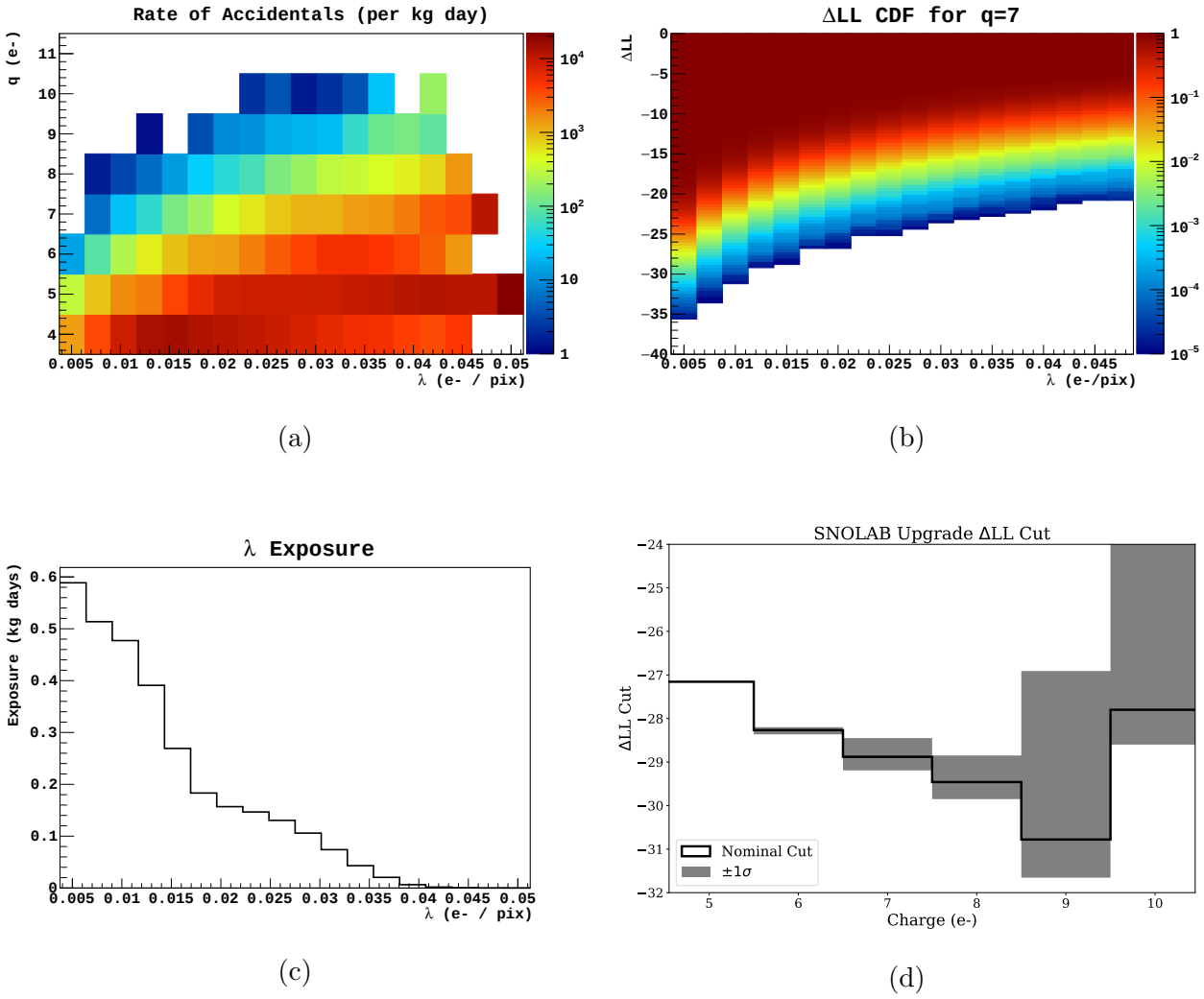

Figure 3.12: Components needed to compute the ΔLL cut values. (a) The accidental rate, $R_a(q, \lambda)$, of clusters (in counts / kg / day) as a function of the local λ value from the blank images. We simulated $\sim$ 30 kg days of images. (b) The CDF, $\alpha(\Delta LL, \lambda|q)$, of the ΔLL distribution for $q = 7$. (c) The distribution of λ values across all images. We convert the exposure to a probability distribution $P(\lambda)$. (d) Finally the ΔLL cut as a function of charge to allow < 0.01 accidental event / kg / day. The uncertainty in the shaded band comes from the uncertainty of the bin content in (a).

SNOLAB we operated with $V_{\rm sub} = 60V$, so we have a direct calibration.

We selected cosmic muon tracks without high energy δ-rays to achieve a set of straight line ionization events with a predictable (x, y) position and depth (z) of interaction relationship. We performed a likelihood fit on the cosmic muon tracks where we convolved the straight line track of the particle with 2D Gaussian with a depth dependent variance

$$\sigma_{xy}^2(z) = -A\ln(1 - bz), \tag{3.15}$$

where the parameters A and b correspond to physical constants in the CCD (see Ref. [99] for details of the derivation), though we fit these parameters without any constraints. We applied a linear energy correction based the backside ionization events between 2-20 $\mathrm{keV_{ee}}$ measured at SNOLAB following the framework of Ref. [68]. Therefore we arrived at a diffusion model

$$\sigma_{xy}(z, E) = \sqrt{-A\ln(1 - bz)}(\alpha + \beta E), \tag{3.16}$$

where $A = 3.07$ pixels^2, $b = 5.35\times10^{-4}\mu\mathrm{m}^{-1}$, $\alpha = 0.889$, and $\beta = 7.4\times10^{-3}$ pixels/$\mathrm{keV_{ee}}$.

To understand the response at low energies, we pasted charge sampled from a 2D Gaussian with the amount of charge following a uniform distribution $q \in [2, 400]$ $\mathrm{e^-}$ and variance sampled from different distribution, depending on the simulation scenario, randomly in the 5×5 pixel likelihood clustering fit window. We added shot noise $\lambda \in [0.00375, 0.05125]$ $\mathrm{e^-}$/pixel and readout noise $\sigma \in [0.16, 0.20]$ $\mathrm{e^-}$ corresponding to the observed detector parameters. We performed the likelihood clustering on the simulated clusters to reconstruct σ_x, σ_y, and σ_{xy}.

We were interested in the detector response to the front ($z \in [0, 10]$ μm) and back surfaces ($z \in [659, 669]$ μm) (CCD surfaces typically have higher radioactive backgrounds due to contamination) and bulk $z \in [0, 669]$ μm (we expect a dark matter signal to interact uniformly throughout the detectors) events. We simulated each population with a variance corresponding to a uniform distribution in the z ranges listed above. To complete the detector response, we convolved the reconstructed cluster response, $R(q, \sigma_{xy})$, for different simulated

λs with the λ distribution shown in Figure 3.12(b) to correctly account for the effect of shot noise on depth reconstruction.

The detector response distributions for front, back, and bulk events are shown in Figure 3.13. From the front and back distributions, we defined a set of σ_{xy} cuts to reject surface backgrounds. For each q bin, we found the σ_{xy} value that rejects 2σ (1σ), or $\sim 95\%$ ($\sim 68\%$) of surface events. These lines are shown in Figure 3.13 as solid (dashed) lines for the 2σ (1σ) cuts. We considered the region in between the 2σ cuts of the front and back surface as true "bulk" events. The efficiency of the 2σ cut is shown in Section 3.3.8.

3.3.7.4 Serial Register Events

Previous measurements with skipper CCDs have shown the possibility of ionization events interacting in, or just outside, the serial register, such that the event is a horizontal streak of charge with no extent in the y-direction[100]. Contrast this with bona fide events from the pixel array where the charge is distributed as a 2D Gaussian. These events can be a fraction of the charge from the initial ionization events and can be reconstructed as low energy events, which is particularly problematic for a dark matter search.

However, the nature of our readout schema, gives us information to discriminate against these type of events. Figure 3.14 shows the σ_y vs. σ_x distribution of Gaussian bulk clusters, constructed in the same way as Section 3.3.7.3, for events with charge $q \in [5, 400]$ e^-. Serial register events would have a large σ_x and small σ_y, so we defined a cut for events with $\sigma_y < 0.2$ and $\sigma_x > 0.5$ pixels. We conservatively applied a similar cut for vertical events, which could be created by defects trapping and releasing charge, but regardless of the origin, they do not fall in the parameter space of real bulk events. This cut would remove only 0.6% of bulk events in the above charge range, though the energy dependence of this cut is accounted for in the final efficiency of Figure 3.15.

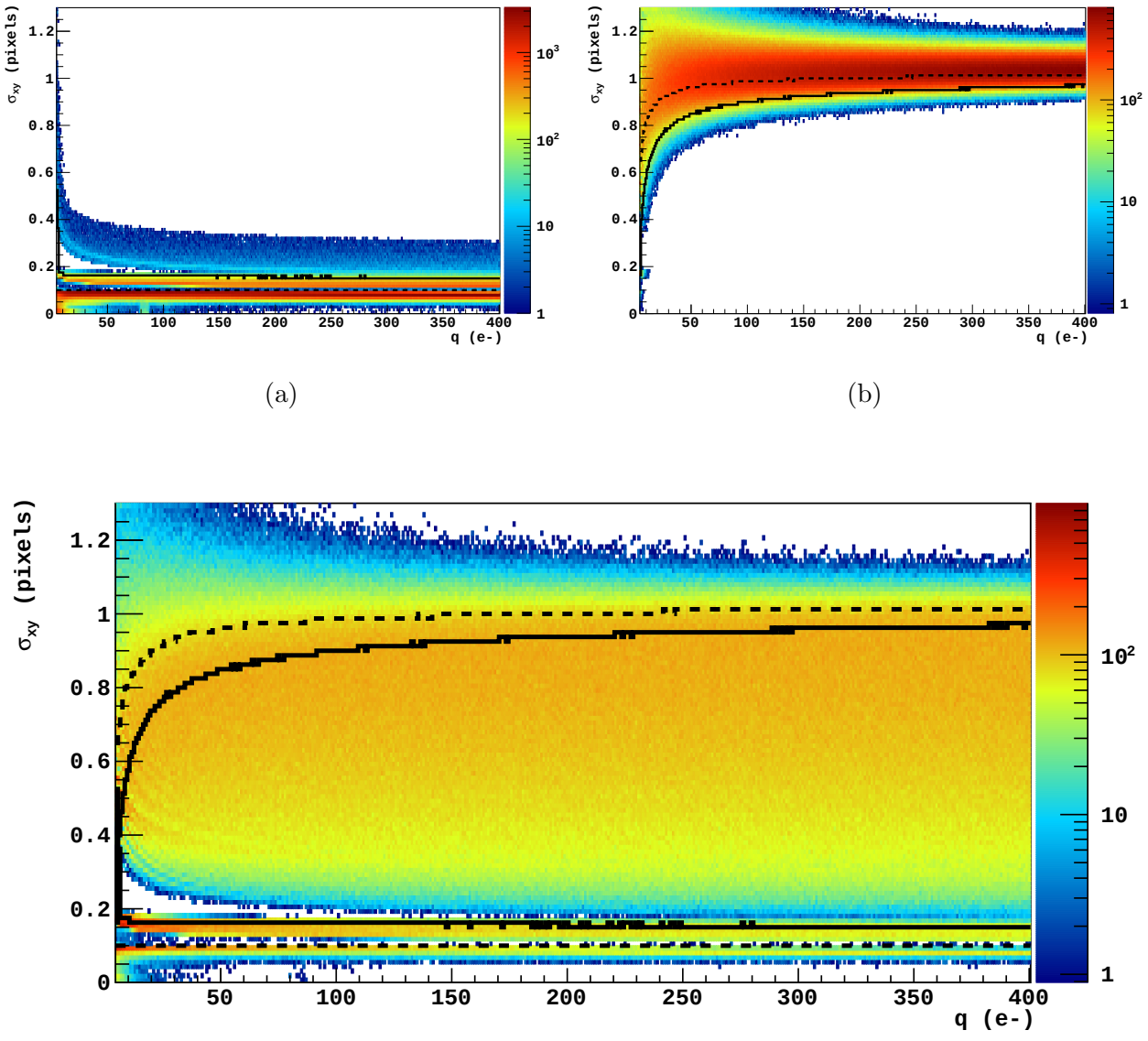

Figure 3.13: Detector diffusion response as a function of charge for (a) front surface, (b) back surface, and (c) bulk events. The solid (dashed) lines correspond to the cuts that reject $\sim 95\%$, ($\sim 68\%$) of surface events.

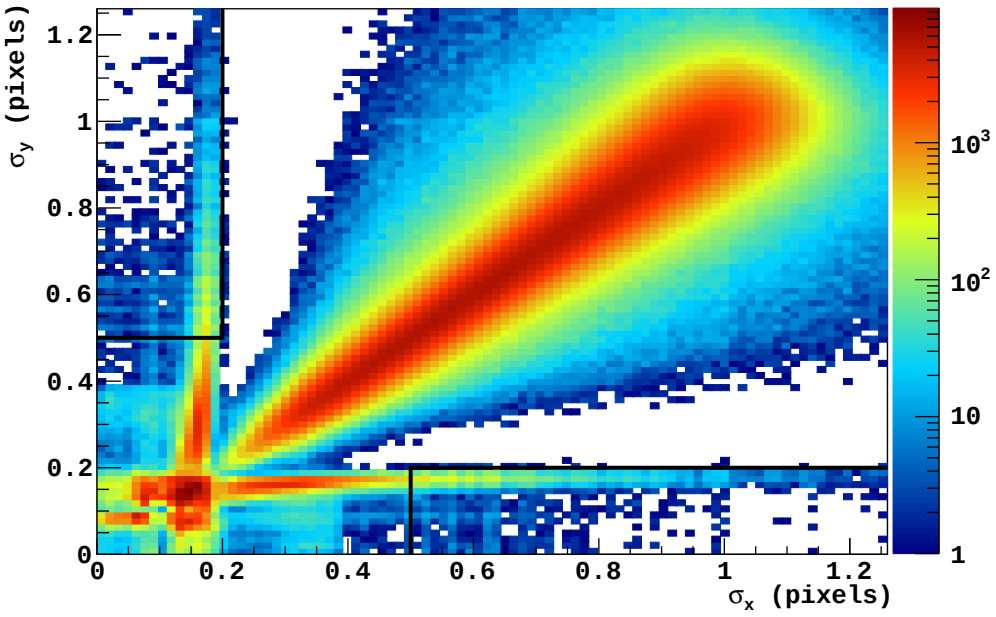

Figure 3.14: σ_y vs. σ_x distribution of simulated bulk events. The serial register cuts are shown by the black lines.

3.3.7.5 Other Considerations

Finally we considered "clean" regions of the CCD with expected and well-behaved charge densities. We excluded clusters below 1 keV_{ee} where the fraction of pixels in a horizontal line, ± 50 pixels outside the center of the cluster window, ≥ 1 e^- is > 0.08. This conditions occurs at a negligible rate in the blanks and is often correlated with charge from an unmasked, higher energy event that leaks out of the fitting window, or some other detector artifact. Regardless, events occurring in these regions are not consistent with real pixel array ionization events.

3.3.8 Detector Efficiency

To compute the detector efficiency, we pasted simulated Gaussian clusters with charge $q \in [2, 400]$ e^- and σ_{xy} corresponding to events uniformly distributed in z through the CCD on

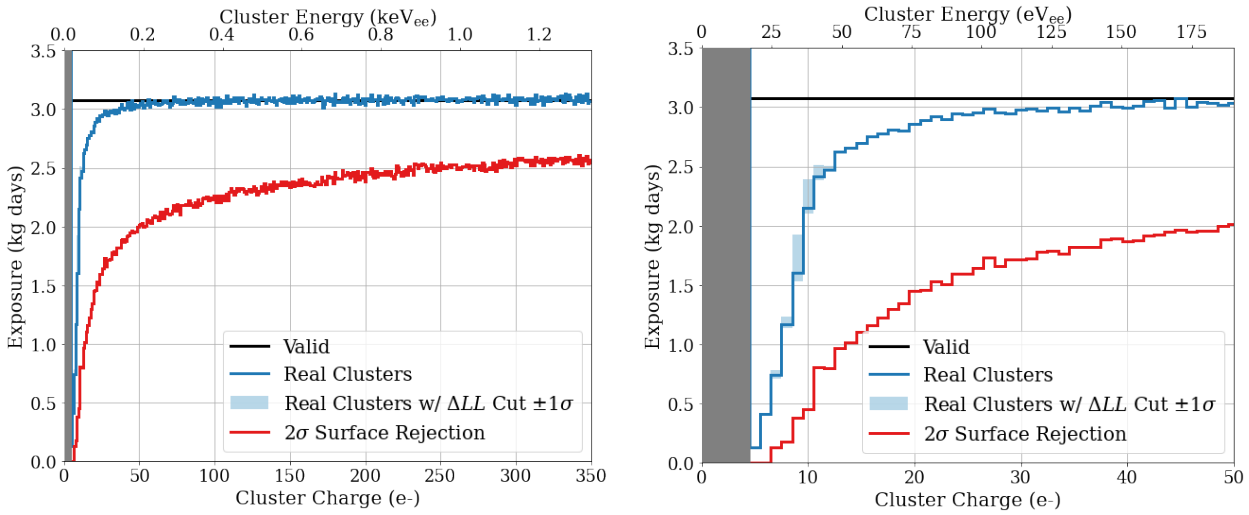

(a) (b)

Figure 3.15: Reconstruction efficiency of simulated clusters after all selection cuts discussed in Section 3.3.7 are applied. The total experiment exposure was 4.81 kg days. We show the efficiency up to (a) 350 e^- and (b) 50 e^-.

blank images. We kept a ledger of the simulated event energies. We performed the likelihood clustering on these simulated events, applied the cuts in Section 3.3.7, and computed the efficiency as the ratio of the number of reconstructed events over simulated events in a given charge bins times the total experimental exposure. The resulting efficiency is shown in Figure 3.15.

The total exposure is 4.81 kg days. We included the efficiency of valid (3.08 kg days, black) as a fit to events ≥ 20 e^-, as for lower charge noise events become a factor. The loss of efficiency compared to the total exposure is largely due to the size of the mask. Better sensors with fewer defects and hot columns would improve the efficiency of the cut. The blue curve in Figure 3.15 shows the efficiency for "real" events, meaning the ΔLL is below the threshold value and the clusters are not horizontal/vertical streaks of charge. With this cut, we achieved 10% efficiency at 5 e^-, 50% at 9 e^-, and 90% at 17 e^-. Lower readout noise

(and therefore fewer skips) and lower dark current sensors could dramatically improve this threshold. The uncertainty of the real clusters arises from applying the uncertainty on the ΔLL cut in Section 3.3.7.2. Finally we included the efficiency (red) of applying the "bulk" cluster selection by rejecting $\sim 95\%$ of surface events. This cut is more impactful at low energies where the stochastic nature of the charge distribution impacts the σ_{xy} reconstruction. The efficiency increases to ~ 2.5 kg days at 300 e^-.

3.3.9 Low Energy Analysis

During data acquisition, we routinely inspected ionization clusters > 500 eV_{ee} (outside our main ROI) and noise like events < 10 e^- (unlikely to contain much signal), but kept the region in between blinded. On February 2nd 2023 we unblinded the full data set.

3.3.9.1 Distribution of Event

Figure 3.16 shows the distribution of events in E-σ_{xy} space. The x-projection shows the energy spectrum of the **bulk events** only, and the y-projection the σ_{xy} distribution for events below 1 keV_{ee}. The black dotted lines and grey shaded regions represent the σ_{xy} cuts to reject 2σ ($\sim 95\%$) of the front and back surface events. The color of the bulk events represent the amplifier in which they were recorded.

I want to bring the readers attention to the density of points below a few hundred eV_{ee}. We observed 11 (29) bulk (surface) events below 200 eV_{ee} and 15 (40) below 400 eV_{ee}. The number of bulk events at low energy is a fascinating measurement. If we consider a quick counting experiment where we take 5% of the measured surface events as leakage, and extrapolate the roughly flat Compton and Tritium bulk events between 1-6 keV_{ee}, we only expected 2.05 events in the bulk. The probability of randomly measuring 11 or more events from a Poisson distribution with $\lambda = 2.05$ is 1.6×10^{-4}. This population of events is statistically unlikely to occur randomly.

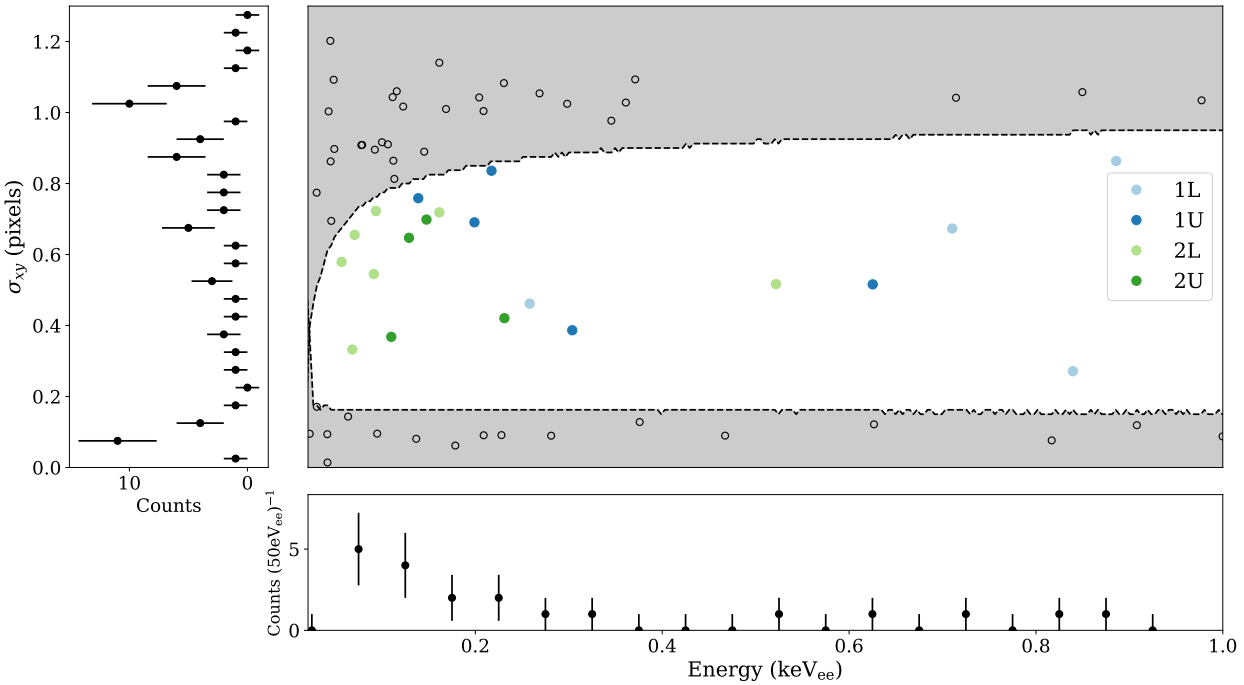

Figure 3.16: Distribution of lower energy ionization events, including the energy projection of the bulk clusters and σ_{xy} projection of all points in the plot. Grey regions are considered surface events.

3.3.9.2 Systematic Checks

We began by inspecting all low energy clusters. A gallery of bulk clusters < 200 eV$_{ee}$ is included in Appendix B. The events were consistent with charge distributed with a 2D Gaussian distribution, located in clean regions of the CCD, and did not appear to be artifacts of other ionization events occurring in the images.

We checked that distribution of low energy events was consistent with randomly distributed in space and time. Here we considered all (including surface) events with energy < 400 eV$_{ee}$. We compared the variables derived from simulated events (distributed uniformly) to the data in Figure 3.17.

We performed this comparison for time of events ((a), p-value=0.53), amplifier the event

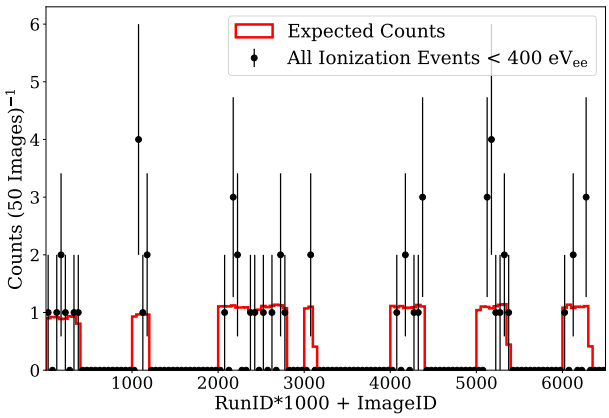

(a) Time distribution of events.

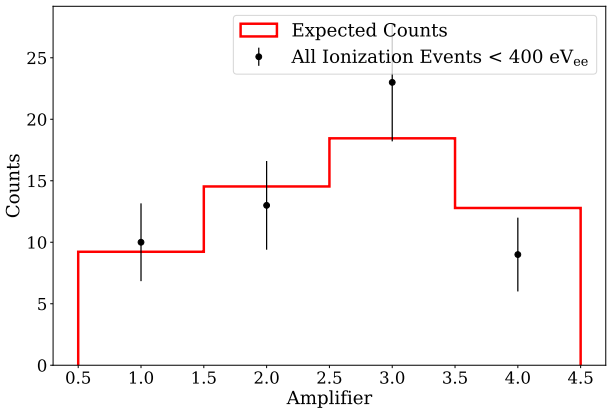

(b) Amplifier distribution.

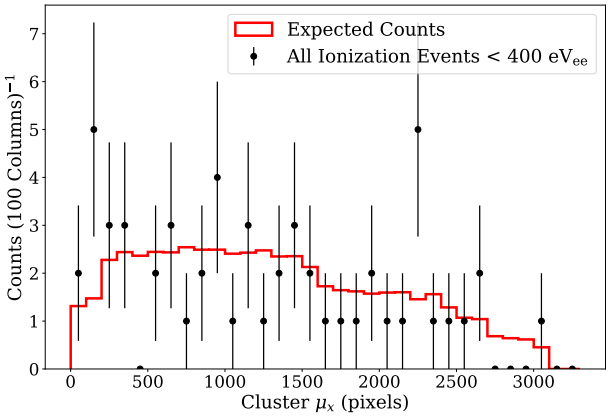

(c) Position distribution.

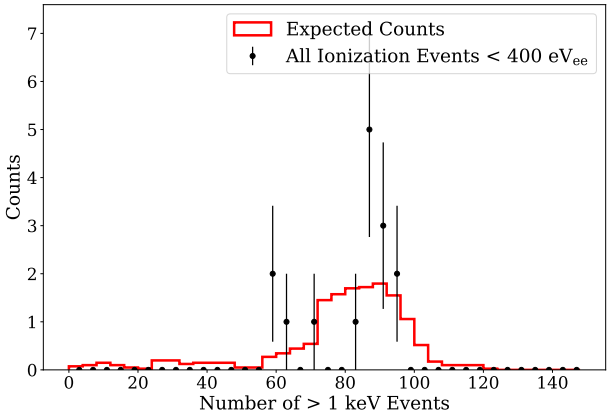

(d) Number of possible time coincident events.

Figure 3.17: Systematic check of events below 400 eV$_{ee}$. We compare the distribution of simulated events (red) with data (black points) for different variables described in the text. In all cases, the data is consistent with the simulated distributions.

was recorded in ((b), p-value= 0.36), x position ((c), p-value= 0.78), and number of potentially coincident events ((d), p-value= 0.41). Note the variable 1000∗runID + imageID is a proxy for the time of events. For the coincident events, we counted the number of ionization events $>$ 10 keV$_{ee}$ recorded within ±4000 rows of the low energy events. This included any

events that could have occurred at the same time as the low energy event and a high number of coincidences could have been due to some underlying event, such as backgrounds from a cosmic muon shower. Unfortunately we do not have better timing resolution due to the nature of continuous readout, so this is not a particularly sensitive variable. The p-values listed above were computed from a Kolmogorov-Smirnov test, with the exception of the amplifier number where such coarsely binned data is inappropriate and we used a χ^2 goodness-of-fit test. There are no statistical abnormalities in the low energy data set.

3.3.9.3 Low Energy Fits

For a complete result, a full radiogenic simulation with a detailed detector response must be performed. However, we completed some analysis to characterize the population of events. We investigated the spectral characteristics of the **bulk** events and performed an unbinned likelihood fit on the data

$$\log \mathcal{L}(b, s, \epsilon|\vec{E}) = -(b+s) + \sum_{i=1}^{n} \left(b f_b(E_i) + s f_s(E_i|\epsilon)\right), \tag{3.17}$$

where b is the number of background events described by a flat spectral component f_b and s is the number of signal events described by a decaying exponential, f_s, with decay length ϵ. The spectral components, f_b and f_s had the bulk efficiency applied. We performed the fit between 0 and 6 $\mathrm{keV_{ee}}$ and the results are shown in Figure 3.18. The fit preferred 12.3 ± 3.9 low energy exponential events and $\epsilon = 89 \pm 30$ $\mathrm{eV_{ee}}$. There is some systematic uncertainty on the low energy number due to potential surface events that leak into the bulk. We estimated, based on the bulk efficiency and number of low energy clusters outside the fiducial region, that 1.2 of the low energy events should be surface events, which is much smaller than the number preferred by the fit. The bulk background rate corresponded to 4.4 ± 0.6 counts/kg/day/$\mathrm{keV_{ee}}$.

Furthermore, we examined the full E-σ_{xy} parameter space and performed a fit where the different depth regions (front/back/bulk) were treated as different fit components. We

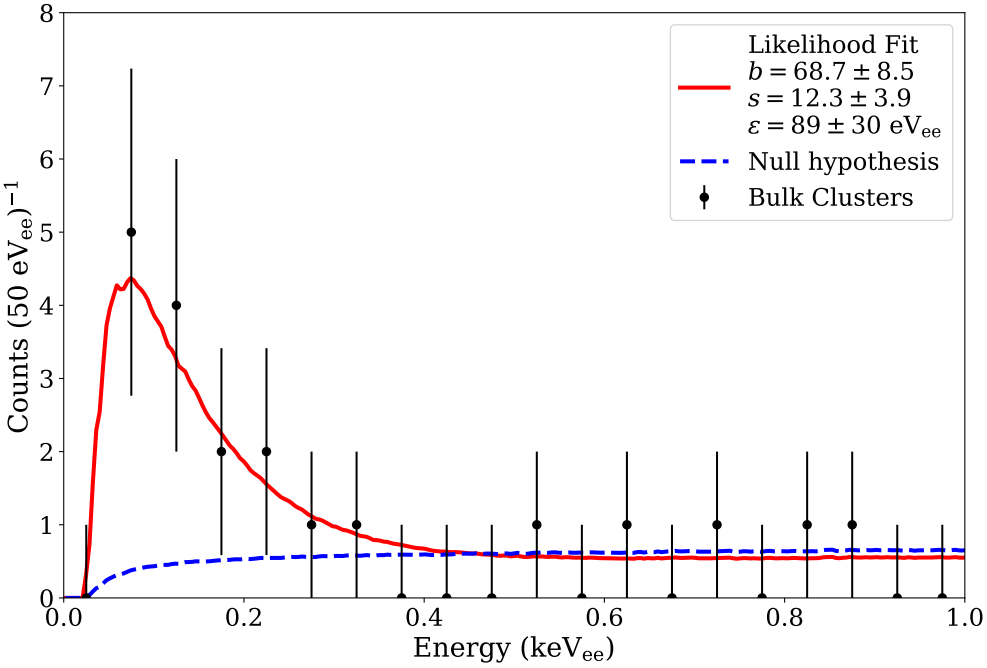

Figure 3.18: Results of the bulk fit with the global (red) and null hypothesis minimum (blue dashed). The fit prefers a low energy component with $s = 12.3 \pm 3.9$ events and decay length $\epsilon = 89 \pm 30$ eV$_{ee}$.

defined a generic model where each of the front/back/bulk populations were comprised of a flat (amplitude b) and decaying exponential (amplitude s and shape ϵ) component, giving nine free parameters to define the model. We used the E-σ_{xy} templates from Section 3.13 including ΔLL and valid cuts for the component templates. We then defined an extended unbinned $\log \mathcal{L}$ function in 2D (E-σ_{xy}) space

$$\log \mathcal{L}(\vec{b}, \vec{s}, \vec{\epsilon} | \vec{E}, \vec{\sigma_{xy}}) = -\sum_{k=1}^{3} (b_k + s_k) + \sum_{i=1}^{n} \sum_{k=1}^{3} \left(b_k f_{b_k}(E_i, \sigma_{xy_i}) + s_k f_{s_k}(E_i, \sigma_{xy_i} | \epsilon_k) \right), \quad (3.18)$$

where we summed over the $k = 3$ components, each with amplitudes for the flat (b_k) and exponential component (s_k). $f_{b_k}(E, \sigma_{xy})$ is the PDF of E-σ_{xy} for the kth component and $f_{s_k}(E, \sigma_{xy})$ is the same template scaled by a decaying exponential with decay length ϵ_k in

the energy axis and normalized to be a probability distribution. Note that the exponential part of the surface components are not strictly "signal," but we referred to the exponential amplitude as s_k to keep the notation consistent with equation 3.17. We minimized the $-\log \mathcal{L}$ using `Minuit` in the energy range 0-6 kev_{ee}. The results of this fit are shown in Figure 3.19 and summarized in Table 3.4.

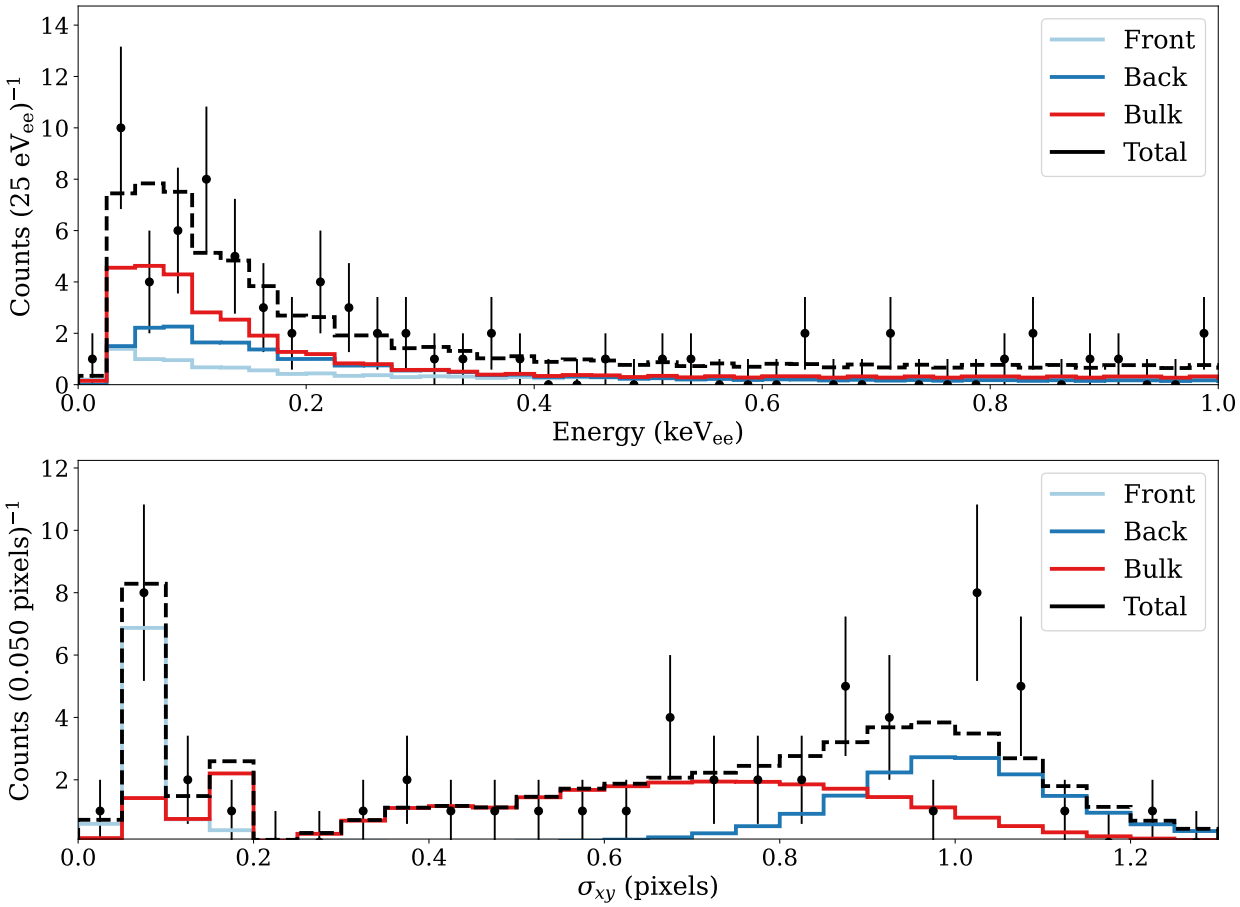

Figure 3.19: Joint fit to the three CCD components (front/back surface and bulk events), each including a flat and decaying exponential spectral piece. The fit was performed in the E-σ_{xy} space, but the projections of the individual components and total spectrum are shown here. The top plot is the energy projection and bottom plot σ_{xy} of energies below 400 eV_{ee}.

	Component		
	Front	Back	Bulk
b_k	61.5 ± 8.3	37.3 ± 6.9	72.0 ± 9.0
s_k	4.7 ± 3.1	15.3 ± 6.2	23.3 ± 6.5
ϵ_k ($\mathrm{eV_{ee}}$)	89 ± 85	130 ± 35	81 ± 23

Table 3.4: Fit parameters to the low energy data.

The fit preferred to add some low energy exponential to the front, back, and bulk of the CCD, which is consistent with the initial impressions of the low energy in Figure 3.16. The fit added the largest number of events to the bulk (23.3) with the shortest decay length (81 $\mathrm{eV_{ee}}$), though all the decay lengths are consistent within uncertainties. We can see with this spectral-depth model we see good agreement in the energy and σ_{xy} projections between the fit and data.

3.3.10 Discussion

The results presented here mark a fascinating data set from the largest skipper CCD exposure acquired to date. We observed an excess of events on both the front and back CCD surfaces and the bulk, with respect to the hypothesis of a flat spectral background. We observed 11 (15) events in the bulk (after surface rejection cuts) below 200 (400) $\mathrm{eV_{ee}}$. A fit to the bulk data preferred $s = 12.3 \pm 3.9$ events with decay length $\epsilon = 89 \pm 30$ $\mathrm{eV_{ee}}$.

While the analysis here is simplified, we can compare the bulk excess parameter space between this result and the 11 kg day exposure in Section 2.2.2. We accounted for differences in exposure and efficiency between the two datasets; we converted the number of events observed into the total interaction rate per kg day of events in the detector, including the impact of efficiency. The resulting parameter space is shown in Figure 3.20.

While we observed a higher event rate in the skipper CCD search presented here, the two

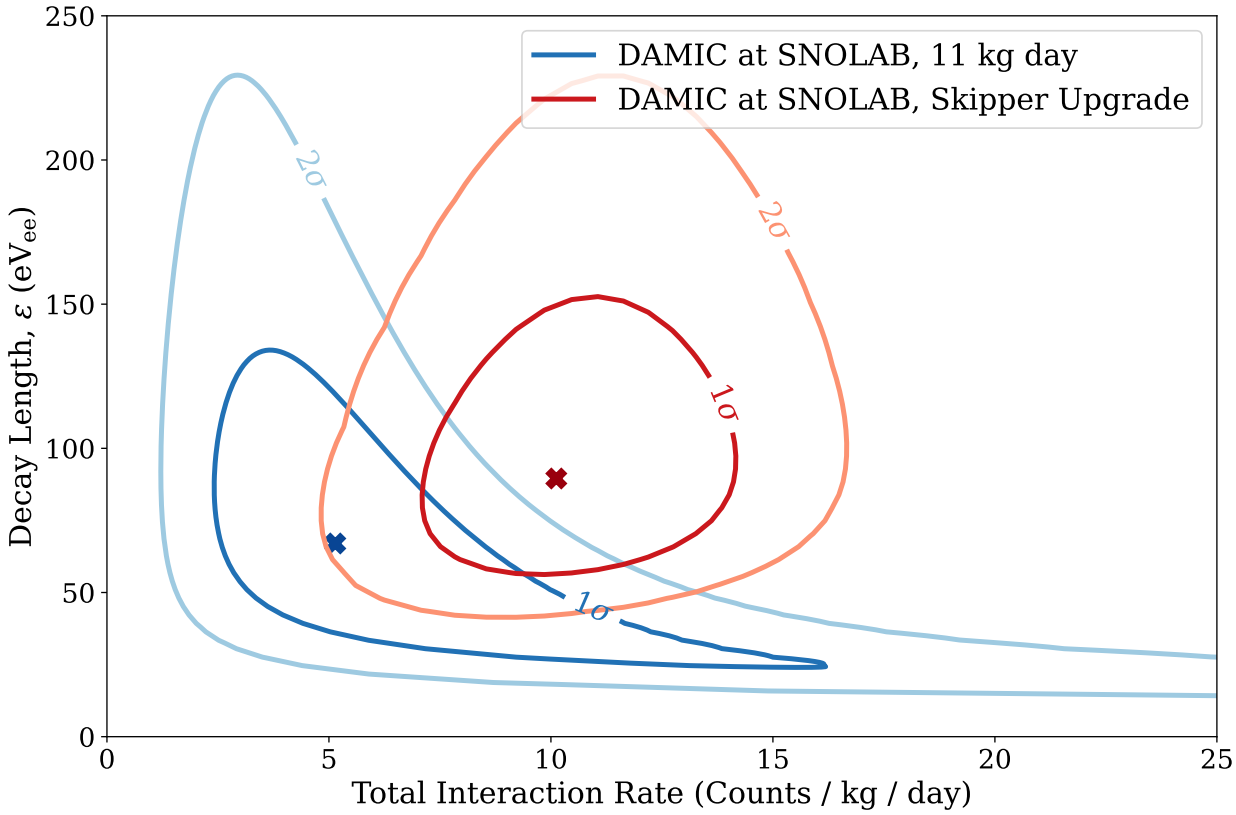

Figure 3.20: Comparison of the allowed parameter space of the bulk component measured in the 11 kg day data set and the bulk component of the fit in Section 3.3.9.3. The x-axis is expressed in total interaction rate (i.e. accounting for efficiency differences) so that the two datasets can be compared.

bulk populations are statistically compatible with one another, suggesting a common origin of the excess.

Of course, the important question is what is this origin. The two experiments operated in roughly the same radiogenic environment, so if we missed a major component to the background model, it would manifest in both experiments. The skipper upgrade also experienced higher surfaces backgrounds, as evidence by the higher α rate on the CCD surfaces, and so **if** this bulk population is really correlated to surface backgrounds, this could explain the

higher event rate we observed with the skipper CCDs. However, it is difficult to explain the σ_{xy} distribution of the measured data from only surface events. We observed many events with $\sigma_{xy} \in [0.3, 0.7]$ pixels, which under the current diffusion model, cannot be explained by surface events. There would need to be a significant unmodeled effect on the front surface of the CCD that skews the reconstructed σ_{xy} to much larger values. So far, we have not found a detector response to explain this; however, we are actively calibrating the surface response of an identical CCD with comparable noise parameters to a ^{14}C source to understand the diffusion response of low energy electrons.

Ultimately, the progression to DAMIC-M with larger mass, lower backgrounds, and a different radioactive environment will be a critical probe to measure (or not observe) this effect. For the time being, we remain uncertain on the origins of this excess of events.

3.4 DAMIC-M and the Low Background Chamber at LSM

DAMIC at Modane (DAMIC-M) is the next generation of the DAMIC experiment [86][84] that will be located at the Modane Underground Laboratory (LSM). The experiment will be composed of 52 modules (Figure 3.21(a)) with four 9 MegaPixel skipper CCDs ($\sim$ 3.5 g each) on a silicon pitch adapter per module for a total mass of $\sim$ 700 g. The array of modules will be constructed from ultra-low background materials to reach a target background rate of 0.1 counts/kg/day/keV$_{\text{ee}}$. DAMIC-M will aim for a 2-3 e$^-$ ionization threshold and a 1 kg year exposure, which will provide significant reach into unexplored DM parameters space for dark sector (hidden photon, DM-e$^-$ scattering) and WIMP-nucleon interactions.

As an intermediate detector, we constructed a Low Background Chamber (LBC) at LSM to further understand skipper CCD operations, environmental backgrounds, and perform dark matter searches. Here we briefly discuss the construction of the LBC and exclusion limits on light dark matter electron scattering.

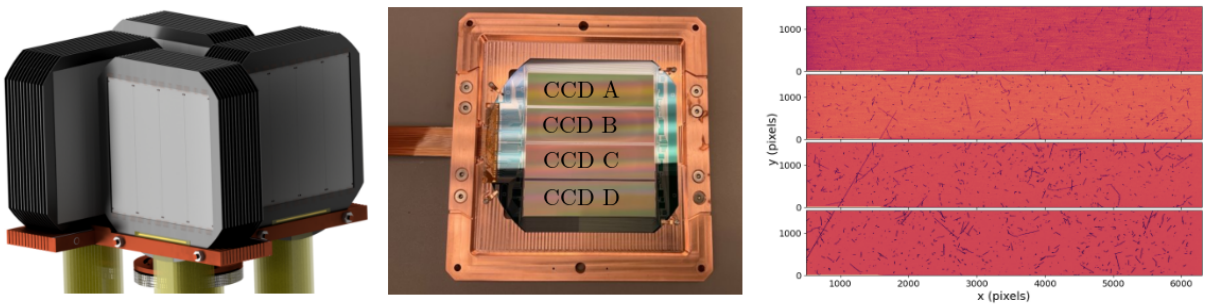

(a) (b) (c)

Figure 3.21: (a) DAMIC-M CCD module array design. Designed by R. Roehnelt. (b) Prototype DAMIC-M module with 4 CCDs connected to a silicon pitch adapter to distribute/read CCD signals. Packaged and tested at UW. (c) Test images taken with the CCD module. Muons can be see traversing across multiple CCDs.

3.4.1 LBC Experimental Setup

The LBC was constructed between October and December of 2021 and was commissioned between December 2021 and March 2022.

Figure 3.22 shows some of the components that make up the LBC. An OFHC copper cryostat houses the experimental apparatus; the cryostat is split into an upper section for the inner detector and shielding and lower section for instrumentation and feedthroughs. The inner detector, like the SNOLAB setup, consists of two 6k x 4k skipper CCDs held in an OFHC copper box, made from two frames that hold the CCD and a top and bottom lid. The box is connected to four cold "prongs" with brass screws that in turn connect to a cold table and cold head of the cryocooler in the lower section of the cryostat. The cold table sits on teflon standoffs to thermally isolate from the cryostat. The inner detector is surrounded by $\sim$ 2 cm of ancient lead and 5-10 cm of low background lead. Each CCD cable (2 cables per CCD) pass through teflon cable guides held in the lead castle and connect to an amplifier and clock shaping board. 39 cm flexible PCB cables are joined in a "2-1" board and connected to 50-pin electronic feedthroughs to the external electronics. The system is

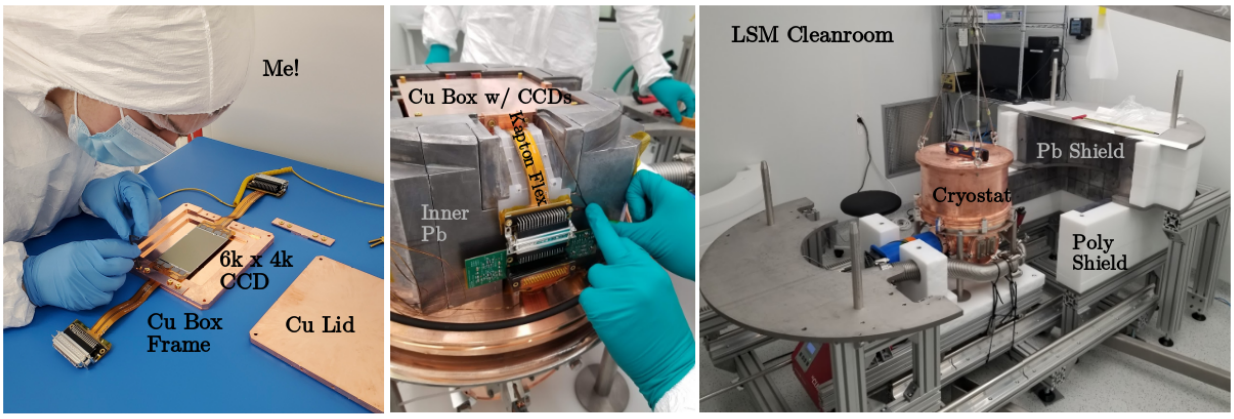

(a) (b) (c)

Figure 3.22: LBC experimental setup. (a) Installation of 6k x 4k CCD in a clean copper frame. The inner detector consists of two 6k x 4k sensors, packaged and tested at UW. (b) Inside the cryostat. The copper box connects to cold copper arms and is surrounded by ancient and low background lead. Kapton cables deliver signals to/from the CCD. (c) The closed cryostat with the partial shield shown. In science operation, the entire detector is surround by lead and polyethylene shielding.

cooled by a Cryotel GT cryocooler and temperature control is performed by a Lakeshore 336 with a heater installed near the cold finger of the cryocooler. Temperature is monitored at the cold finger, on the "prongs" near the CCD, and on the lead shielding (to ensure no unintended thermal path to the lead). A Pfeiffer HiCube Eco80 pump brings the vacuum to $\mathcal{O}(10^{-6}$ mbar), which is monitored by two pressure gauges, though the gauge nearest to the detectors is often turned off during data acquisition.

The cryostat is further shielded by $\sim 4\pi$ coverage of 15 cm of lead and 21 cm of polyethylene to shield from external γs and neutrons, respectively. A Rad7 device monitors the radon level in the cleanroom.

CCD control and readout is performed by two independent Leach electronic systems from Astronomical Research Cameras, which have been previously used for CCD calibration

[76][74][101], each independently controlled by a separate computer. The CCD substrate bias is applied by DC205 precision voltage sources from Standford Research Systems. The data is mirrored to the IN2P3 computing clusters in Lyon.

The entire apparatus is contained in an ISO Class 5 cleanroom. More details on the design and assembly can be found in Ref. [102].

The full commissioning of the LBC CCDs is beyond the scope of this thesis, but details can be found again in Ref. [102]. The SNOLAB and LSM systems were commissioned in conjunction with each other and similar tests and procedures were performed to minimize the leakage current across the CCDs.

3.4.2 Light Dark Matter-Electron Scattering

We searched for sub-GeV dark matter scattering of electrons in the silicon atoms following the signal models in Ref. [33]. The details of the analysis can be found in Ref. [103].

3.4.2.1 CCD Operation

We acquired two datasets of ~ 100 g days each in two operation modes. In both datasets, we measured 650 skips per pixel and acquired images with 10×10 binning (150×150 μm^2 super-pixel size) to hardware bin any DM signal diffused over multiple pixels. The binning is much larger than the event diffusion ($\sigma_{xy} \sim 1$) so any signal would most likely contained in the single binned super-pixel. For the data in Science Run 1 (SR1), images of 840 rows $\times$ 640 columns were taken continuously one after another and every pixel in a given column, after the first 413 rows, experienced the same exposure time and $\lambda \sim i_r t_r$ value. In Science Run 2 (SR2), only a quarter of the CCD, 110 rows $\times$ 640 columns, was readout and the CCD was cleaned (quickly clock all the charge out of the pixel array) in between images. The partial read reduced the average pixel exposure time to $t_r/8$, which reduces the shot noise during readout by a factor of 8. With the reduced λ, the number of a pixel with q electrons scales like

$$n_q = n_p \frac{\lambda^q e^{-\lambda}}{q!} \sim \frac{n_p \lambda^q}{q!} \tag{3.19}$$

since $\lambda << 1$. We therefore expected a reduction in the number of pixels with q charge of $\left(\frac{1}{8}\right)^{q-1}$ between SR1 and SR2, which is significant for the 3 and 4 electron pixels which drive the limit in large regions of parameter space. In reality the reduction in λ was not quite that significant as there are other contributions to the shot noise, such as the clock induced charge component, which affects all pixels equally. We measured an reduction in the shot noise by ~ 4. The trade off for the SR2 operating conditions is 8 times more pixels must be read, thus increasing data acquisition time for the same total exposure.

Images were compressed by taking the average value of all the pixel skips. We performed the following analysis on the pixel distribution of all the average images.

3.4.2.2 Masking

We collected a dedicated data set of 13 images at a temperature of 120 K with 420 rows $\times$ 640 columns, 10×10 hardware binning, 3 hr exposure, and ~ 40 minutes readout time and generated a median image, as in Section 3.3.4.1, from these images. Only charge that was persistent in the same location across multiple images was present in the median image. We grouped contiguous pixels with $> 3\sigma_r$, the readout noise, in the median image and defined a cluster if the total charge was $> 5\sigma_r$. We excluded any columns where a high charge defect was located. We also masked any columns where the 1 e^- rate in the science data was $> 2\sigma$ above a parameterized function of the baseline 1 e^- rate.

We masked any clusters—groups of contiguous pixels $> 3\sigma_r$ that contained at least one pixel ≥ 2 e^- and had a total charge of > 7 e^-—to exclude known ionization events and their diffused halos. We additionally masked 10 pixels in the trailing vertical and horizontal direction to capture any CTI from high energy events.

Finally, we excluded regions after large ($> 2\sigma$) downward fluctuations in the column λ value that were followed by regions of worse charge transfer. These were possibly traps in

the serial register that could distort the DM signal. We excluded all columns in UW6415D and columns > 74 in the UW6414D L amplifier.

After masking, the total exposure was 85.23 g days, with 45.26 (39.97) g days for SR1 (SR2).

3.4.2.3 Results

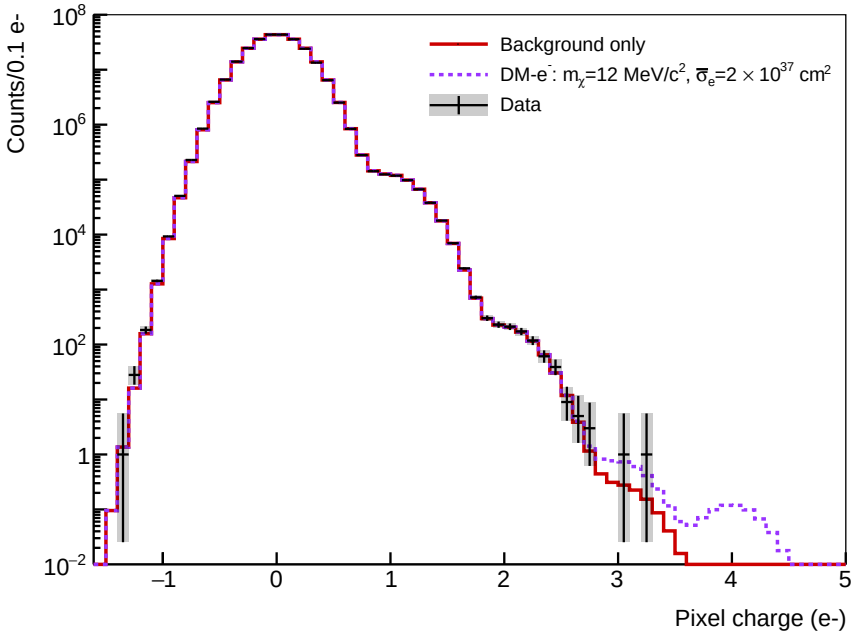

Figure 3.23: Pixel distribution of UW6414D U amplifier in the SR2 data set, after the cuts described in the text. The expected signal for DM-e^- scattering from a 12 MeV/c^2 at the 90% C.L. cross section is shown on top of the background model. Figure from Ref. [103].

We performed a binned likelihood fit to the pixel distribution where the probability of measuring the pixel value p_i is a contribution of a dark matter template $S_\chi(q|m_\chi, \sigma_e)$ and the shot noise λ_i at the pixel. To include the detector response to a DM signal S_χ, we converted the energy deposition in Si to e-h pairs created using the ionization efficiency in

Ref. [95], simulated 2D Gaussian clusters with uniform z distribution following a $\sigma_{xy}(z)$ relationship similar to in Section 3.3.7.3, but with a V_{sub} of 70 V, pasted the clusters on images, and binned the simulated images with 10×10 hardware binning. We performed this procedure for the range of DM masses we were interested in. We modeled the shot noise by creating a λ map as a function of pixel position, $\lambda(x)$ ($\lambda(x, y)$), for SR1 (SR2 where pixels in the y direction experience different exposures) similar to in Section 3.3.4.1. We fit all pixels measured in a given column for SR1 or position for SR2 to a Gaussian convolved with a Poisson distribution to generate the map which acted as our background model. The full fit function is stated in Ref. [103]. We maximized the binned log-likelihood of the data compared to the model and found no preference for a DM signal (sample pixel distribution in Figure 3.23). Therefore we placed exclusion limits on the DM-e^- cross section by scanning over the cross section for a given mass until the test statistic in the likelihood ratio test exceeds the value corresponding to the 90% C.L. (see Section 2.2.2 for more details on the procedure).

The limits for sub-GeV are shown in Figure 3.24 for both an (a) ultra-light and (b) heavy mediator. The derived limits are within the $\pm 1\sigma$ sensitivity. We excluded additional parameter space on the DM-e^- scatter cross section between 1.6-1000 MeV/c^2 for the ultra-light and 1.5-15.1 MeV/c^2 for the heavy mediator.

3.4.2.4 Systematic Checks

For each stage of the analysis, multiple groups checked the results with independent pieces of software and achieved consistent results. At UW we replicated the analysis up to the pixel distribution.

We processed the raw images in an identical matter to Section 3.3.2 and created independent λ maps to those used in the analysis above. We developed a data driven mask from the λ maps. First we generated a λ pedestal by calculating the moving median in 41 column window (5 row $\times$ 41 column window) for SR1 (SR2). We subtracted the pedestal from the λ, and masked any single pixels in the resulting distribution $\pm 5\sigma$ fluctuations or columns with

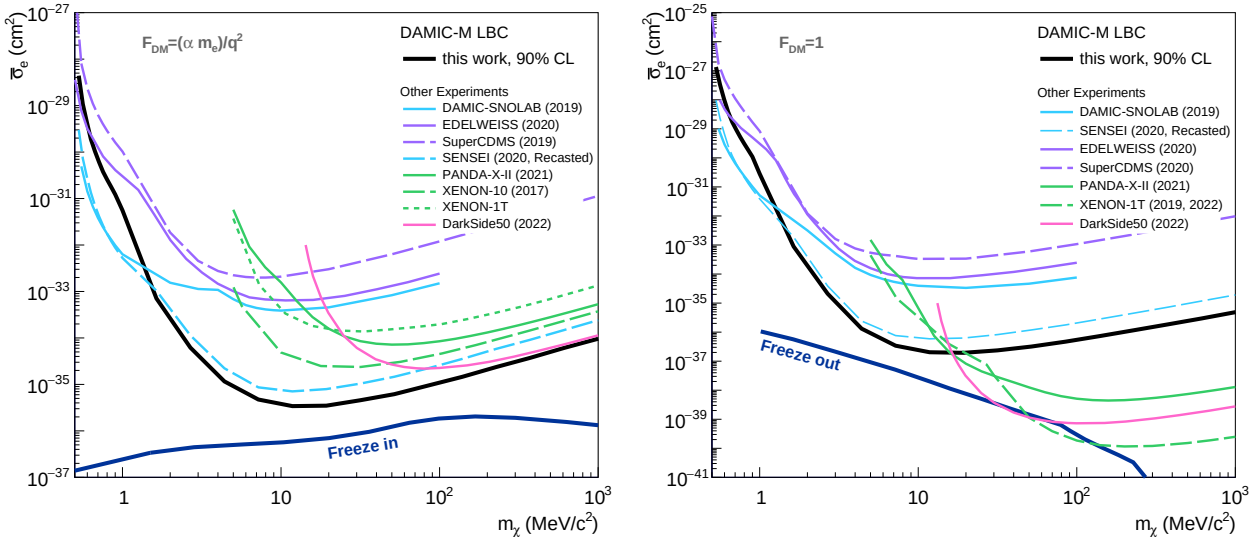

(a) (b)

Figure 3.24: Limits from the LBC data for a (a) ultralight (bottom, $F \sim 1/q^2$) and (b) heavy (top, $F \sim 1$) mediator[103]. Other experiments [104, 80, 105, 106, 83, 107] and the freeze in/out milestones [33] are also shown. The SENSEI limit was originally published in Ref. [83], but here has been recast [86] using the standard halo model parameters that the community has agreed upon [30].

≥ 7 pixels with $\pm 2.5\sigma$ deviations. Finally we masked a region ± 10 pixels around any single pixels ≥ 10 e$^-$. We masked trailing horizontal and vertical pixels—the number masked was dependent on the charge of the pixel—to account for potential CTI.

The resulting probability distribution of the measured pixels between the "official" data and this systematic check were compatible, indicating this stage of the analysis was robust. Other collaborations cross-checked the signal distribution creation and likelihood fit and also achieved consistent results.

Chapter 4

THE SELENA NEUTRINO EXPERIMENT

4.1 Conceptual Design

The Selena Neutrino Experiment is a proposed 100 ton year exposure of enriched amorphous ^{82}Se coupled to pixelated CMOS imagers. The material properties, excellent position reconstruction and event discrimination with track topology, and realizable technologies make Selena a promising candidate for the next generation of neutrino physics.

4.1.1 ^{82}Se Properties

^{82}Se has several useful properties for $0\nu\beta\beta$ and neutrino spectroscopy. The natural abundance of ^{82}Se is 8.7%, which while respectable, for large scale detectors will need to be enriched. ^{82}Se also undergoes $\beta\beta$ decay with a $Q_{\beta\beta}$ value of 2998 keV and half life of $T^{2\nu}_{1/2} = 10^{20}$. The $Q_{\beta\beta}$ is above most background lines from primordial ^{238}U and ^{232}Th, which results in an inherent background suppression in the region of interest.

Furthermore ^{82}Se can capture electron neutrinos with a threshold of 172 keV. The event will release an electron with $E_\nu - 172$ keV of energy an leave a ^{82}Br in the 1+, which will then undergo three decays before ending at ^{82}Kr as shown in Figure 4.1(a). The first two decays are separated by a half life of only 7.2 ns and will be inseparable by any reasonable detector. Therefore we expect a triple coincidence of events located in the same position in the detector; if this sequence can be identified—and the following sections will outline a detector that can efficiently tag them—then a background free ν_e spectroscopy with a 172 keV threshold is possible.

Selenium in general has been used as a photoconductor for many years and its properties are well characterized [108][109]. The ubiquity as a target in flat-panel x-ray detectors means

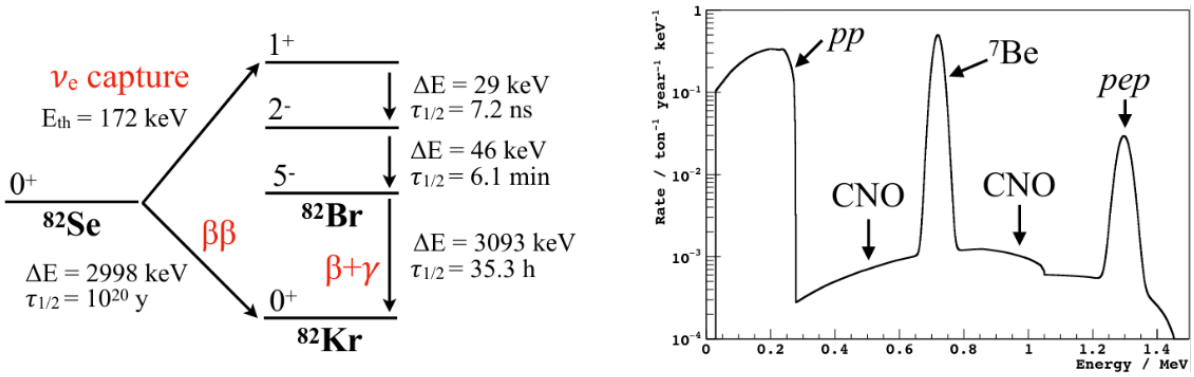

Figure 4.1: (a) Decay sequence following a ν_e capture in ^{82}Se with decay energies and half-lives (b) Expected solar neutrino spectrum from a 100 ton year exposure with efficient ν_e tagging.

the deposition technology is mature and scalability for a large physics experiment is possible.

4.1.2 Amorphous Selenium as a Radiation Sensor

Amorphous selenium (aSe) is commonly used as a photoconductor for x-ray imaging in the medical field, but more generally is sensitive to any ionizing radiation interacting with the target material. A schematic of the procedure to measure ionization energy is shown in Figure 4.2 and described below.

In the simplest case, aSe is placed between an anode and cathode. A bias potential is applied to the cathode and the anode is connected to some charge sensitive amplifier (CSA), such as a Op-Amp with feedback capacitor [110], that integrates the current flowing through the selenium. When energy is deposited in the detector, electron-hole (e-h) pairs are created in the aSe when the electrons in the valence bad are promoted to the conduction band (separated by a 2.3 eV band gap). In aSe, the average energy to create an e-h pair is theoretically predicted to be a few times the band gap energy, $w_0 \sim$ 4-7 eV [111]. However, experimentally measured values are much higher. This is due to the possible recombination of

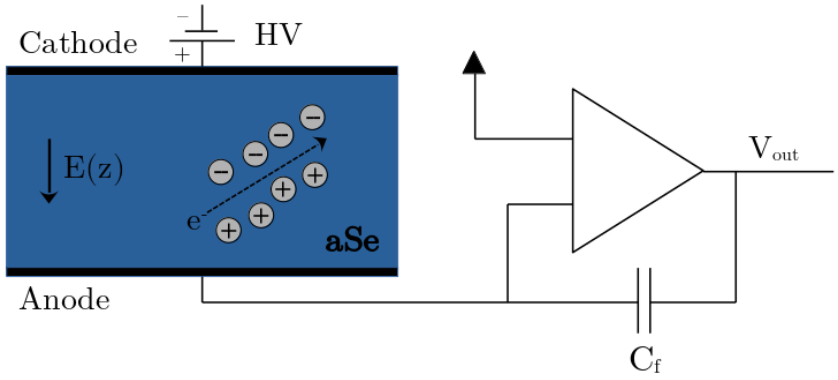

Figure 4.2: Schematic of the procedure to measure energy in aSe. An ionizing event interacts in the aSe detector and generates e-h pairs. These charge carriers drift in the electric field created by the high voltage (HV) and induce a charge on the anode. This induced charge builds up on the feedback capacitor C_f, which can be converted to a voltage v_{out} that is proportional to the initial ionization event energy.

electrons in the conduction band with vacancies (holes) in the valence band. Either geminate (electrons combining with their initial hole) or columnar (combining with other holes while drifting through the semiconductor) can occur during high energy interactions when many e-h pairs are created. Significant work has gone into understanding the amount of charge that is collected for a given incident energy, the effective work function w_{ehp} [112, 113]. For our purposes, we use a model based on Ref. [113] and recombination in liquid argon—another disordered system with stochastic recombination—that ultimately well describes data we took in Ref. [114].

$$w_{\text{ehp}} = w_0 \left(1 + \frac{E_k \alpha}{8\pi r_0^2 w_0 E_b \mu(E_b)}\right) \tag{4.1}$$

The effective work function (w_{ehp}) depends on the theoretical work function (w_0), the length scale (r_0) over which energy (E_k) is deposited, the mobility (μ) of the carriers in the bias field (E_b), and a material dependent scaling factor (α). Notably the work function

decreases with increasing field, resulting in better SNR for a given interaction at higher fields.

The fluctuations of the number of charge carriers created is particularly important for a $0\nu\beta\beta$ experiment as it contributes to the experimental resolution at $Q_{\beta\beta}$. Experimental results have shown the intrinsic resolution to be larger than just Fano fluctuations, and this again results from higher order recombination effects in the presence of ionization events. The dependence of the recombination as a function of stopping power, dE/dx, along the charge track well describes the energy resolution for $\mathcal{O}(100$ keV) events [115]; this model is extrapolated to $\mathcal{O}(1$ MeV) events to inform the scientific potential of aSe in Section 4.2.

After e-h pairs are created, they drift in opposite directions due to the field created by the applied bias voltage at velocity $\vec{v} = \mu_{(h/e)}\vec{E}$. The mobility of holes is ~ 100 times larger than of electrons in aSe [115]. Holes drift to the anode and electrons to the cathode. As they drift, each ith charge carrier induces a surface charge on the anode

$$Q_i(t) = \oiint_{\text{elec}} \epsilon \vec{E}_i(r_i(t)) \cdot d\vec{S}, \tag{4.2}$$

i.e., is the surface integral over the anode of the normal component of the electric field generated by the ith charge at position r_i, to enforce that $\vec{E} = 0$ inside the metallic anode. The total charge induced on the anode is then

$$Q(t) = \sum_{i}^{N} Q_i(t), \tag{4.3}$$

the sum over all charge generated by the incident radiation. The charge induced on the the anode results in a build up of charge on the feedback capacitor of a charge amplifier which results in a measurable voltage, $V = Q/C_f$, where C_f is the feedback capacitance, and typically $\mathcal{O}$(fF-pF). Therefore the measured voltage is proportional to Q which is proportional to the amount of energy deposited.

The charge drifting in the $\hat{z}$ direction will also diffuse in all directions which manifests as a lateral spread on the xy plane that follows a 2D Gaussian distribution with $\sigma_{xy}^2 \propto t_{\text{drift}} \propto 1/|E| \sim \mathcal{O}(1\ \mu\text{m}^2/\text{mm})$ for the typical $\mathcal{O}(10\ \text{V}/\mu\text{m})$ fields at which aSe detectors are

operated. For a pixelated detector, such as that described in Section 4.1.3, the low diffusion results in excellent fidelity of the track topology and high SNR as the event is spread over fewer pixels. The σ_{xy} can also be used for depth reconstruction as in Ref. [69]; however, the lower diffusion impacts the ability to extract the z coordinate. Advanced analysis techniques for depth reconstruction of the proposed Selena detector are still under investigation.

This simplified picture leaves out the details of the geometry of the charge sensitive anode. Depending on the application, this could be a single metallic layer, coplanar detector for unipolar sensing [116], or a more complex pixel structure made up of many anodes as will be discussed in the remainder of this chapter. Furthermore, the amplifier and readout scheme must be optimized for the specific scenario, but that is beyond the scope of this document. Regardless of the details of the readout scheme, the underlying physics of the charge generation outlined here remain the same.

4.1.3 Selena Detector Properties

The Selena experimental design was originally proposed in Ref. [117] and has been expanded in Ref. [118].

The core detector, shown Figure 4.3, is modules of thick, ~ 6 mm, layers of aSe deposited on a standard 300 mm silicon wafer packed with 2.5×2.5 cm^2 complimentary metal oxide semiconductor (CMOS) active pixel sensors (APS) to cover the wafer. Each sensor is made up of $\sim 10^6$ tightly packed hexagon pixels of an electrode surrounded by a metal guard ring for electrical isolation and calibration (see Section 4.3.5.1). We selected hexagonal to eliminate sharp angles in the design to reduce the electric fields resulting from extremely high bias voltages needed for good energy resolution. A gold electrode of a few nm thickness will be deposited on top of the aSe to apply the bias voltages. Low radioactivity cables will connect to the wafer and traces/vias etched onto the wafer will deliver the necessary control and readout signals to each individual sensor. Each module will consist of ~ 2 kg of selenium, and the experiment will ultimately be an ensemble of modules—the number of which is dependent on the ultimate target mass.

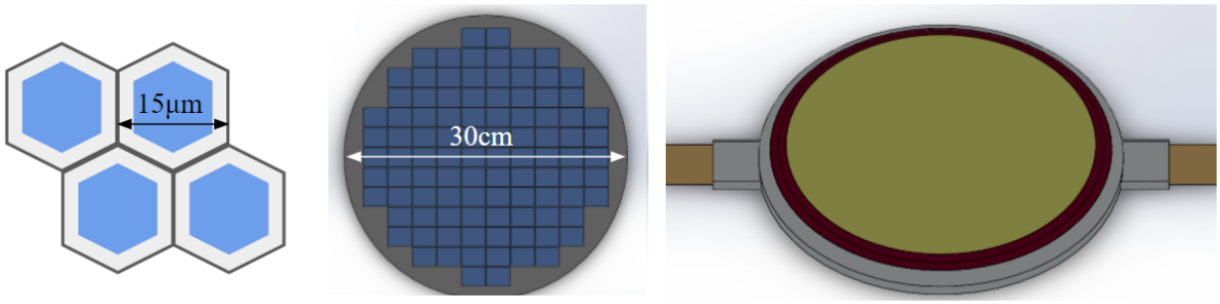

(a) (b) (c)

Figure 4.3: Selena Neutrino Experiment module concept. (a) Hexagonal pixels with 15 μm pitch and a charge sensitive amplifiers make up the CMOS APS reticle. (b) A 300 mm wafer is packed with square reticles. (c) $\sim$ 6 mm of aSe is deposited on the wafer with a thin gold electrode on top.

As each pixel is sensitive to the charge create above it, we measure the xy projection of the energy depositions in the track, binned into 15 μm pixels. This excellent xy resolution is the crux of the background reduction as we can topologically reject different background species.

For example, the stopping power of α particles is orders of magnitude higher than βs for the same energy, so the α will exhibit as a dense region of charge, compared to a "worm" track of a β as it deposits its energy over many pixels. This is the simple application that easily allows rejection of all α events. β decay, such as those from ^{214}Bi and ^{208}Tl (daughters of the primordial chains with high enough endpoint to deposit energy in the ROI), will start from a point and deposit energy with approximately constant $\frac{dE}{dx}$ while it is minimum ionizing before increasing the energy density as it slows down, forming a Bragg peak at the end. `Geant4` simulations have clearly shown this effect. Now compare this to a $\beta\beta$ where two electrons start from a vertex, deposit their energy in a similar many as the single electron, but each electron creates a Bragg peak. Previous work suggests that based on the Bragg peak information we could expect 10^{-3} suppression on the single β events while keeping

50% of the $\beta\beta$ signal [117]. High energy γ-rays interacting with the aSe via photoelectric absorption or Compton scattering would be similarly discriminated versus the $\beta\beta$ signature.

Another form of background rejection relies on the spatial-temporal correlation of energy depositions, similar to the technique leveraged in the DAMIC CCDs to constrain the quantity of radioactive contaminants of ^{32}Si, ^{210}Pb, ^{238}U, and ^{234}Th intrinsically in the detector [98]. We look at a single pixel, or group of pixels, that are hit by multiple ionization events. The expected number of background events in a pixel

$$\lambda_b = R_b m_p \Delta E \Delta t, \tag{4.4}$$

is a product of the background rate (R_b), mass of the pixel (m_p)—which is the density (ρ) of aSe times the pixel volume volume (V)—energy range (ΔE), and exposure time (Δt). Using a background rate of 10^{-2} counts/kg/day/keV—a value already achieved the low-background, solid state detector of the Majorana Demonstrator[119]—$\mathcal{O}(1\ \mu\text{g})$ pixel mass, the full $Q_{\beta\beta}$ value of 3 MeV, and a 10 year run time, we find $\lambda_b \sim \mathcal{O}(10^{-4})$. Since $\lambda_b << 1$, the probability of finding multiple background events in a given pixels scales like λ_b^n, where n is the number of background events, and becomes extremely small for $n \geq 3$. Even considering the $\sim 10^{13}$ pixels that will make up the 10 ton detector, for $n = 3$ we would expect $\mathcal{O}(10)$ accidentals over the entire lifetime of the experiment. We gain additional suppression power when considering chains of radioactive decay within the detector where the half-life and energy of the daughters of some radioactive contaminant constrain the ΔE and Δt and still contain nearly all of the radioactive coincidence. This allows heavy suppression on certain backgrounds [117], such as the ^{214}Po and ^{216}Po chains that can emit single βs in the $0\nu\beta\beta$ region of interest, and also allows for a unique probe of neutrino captures (Section 4.2).

4.2 Science Reach

The science capabilities of a 100 ton-year exposure of the detector describe above are detailed in the following section.

For $0\nu\beta\beta$, we expect sensitivities of $T^{0\nu}_{1/2} \sim \mathcal{O}(10^{28})$ years. The current lower limit of the of $0\nu\beta\beta$ half life from ^{82}Se to ^{82}Kr is $T^{0\nu}_{1/2}(^{82}Se) > 4.6 \times 10^{24}$ years, set by CUPID-0 [56]. This limit is quite a bit lower than the $\mathcal{O}(10^{26}$ yrs) limits from ^{136}Xe and ^{76}Ge experiments suggesting there is significant room for development with respect to selenium, and we could achieve comparable sensitivity with just a few kg years exposure of ^{82}Se. Figure 4.4 shows MC trial for 100 ton year exposure of a $0\nu\beta\beta$ signal with $T_{1/2} = 10^{28}$ years over the $2\nu\beta\beta$ signal, assuming the no other backgrounds [117] in the region of interest other than the $2\nu\beta\beta$ signal. For simplicity, if we consider the energy region $> Q_{\beta\beta}$, we expect 50% of the signal and 0.069 counts / ton / year of $2\nu\beta\beta$ background, which as a counting experiment, yields an expected sensitivity of 5.9 $0\nu\beta\beta$ events corresponding to a limit 2.1×10^{28} years (90% C.L.) for the full 100 ton year exposure, assuming a 50% acceptance rate of $\beta\beta$ events. A full profile likelihood ratio test with spectroscopic information would improve the sensitivity.

For neutrino capture spectroscopy, the Selena detector could efficiently tag ν_e captures above the 172 keV threshold with no other background expected to leave the specific triple coincidence in a given spatial region. For the full 100 ton exposure, we expect to measure $\mathcal{O}(1000)$ neutrinos from each of the *pp* and ^{7}Be processes and $\mathcal{O}(100)$ from *pep*, CNO, and ^{8}B processes; precise number can be found in Ref. [118]. The improved uncertainty on the counts of the different neutrino species would place a strong constraint on the neutrino luminosity, probe the onset of the Mikheyev-Smirnov-Wolfenstein (MSW) effect [120], and resolve the solar metallicity problem [121]. Furthermore, the temperature of the suns core distorts the solar neutrino lines allowing the first direct measurement of the core temperature from our measured neutrino capture spectrum [122].

Finally, the Selena detector could probe parameter space in the existence of light sterile neutrinos [65][123]. Recently the BEST collaboration reported a statistically significant 20% deficiency with of the ν_e capture rate in ^{71}Ga giving the best and strongest evidence for the "gallium anomaly." This could be interpreted as sterile neutrinos in a 3+1 mixing model with an $\mathcal{O}(1$ eV$^2)$ Δm^2_{14}, and is roughly consistent with weaker statistical evidence observed by T2K [124]. By placing a high radioactivity (3.5 MCi) ^{51}Cr source in the center of the 10 ton

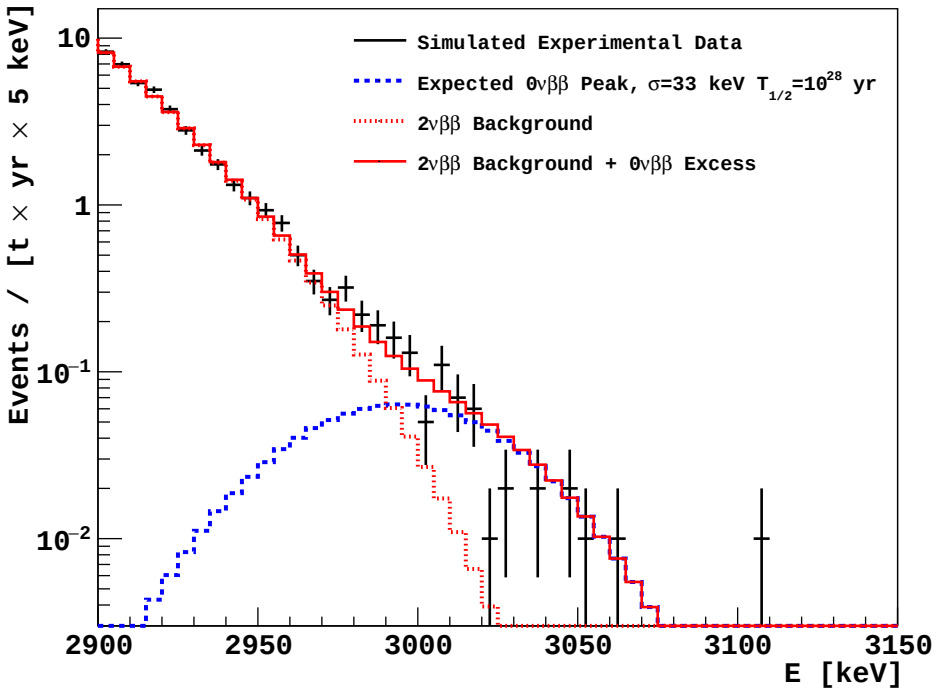

Figure 4.4: A toy MC experiment (black) of $0\nu\beta\beta$ with $T_{1/2} = 10^{28}$ in a 100 ton year exposure of ^{82}Se. The expected distribution of the $2\nu\beta\beta$ background (red-dashed) and $0\nu\beta\beta$ signal (blue) assuming the detector performance described in the text are shown. While there is overlap between the distributions, a clear "skew" of the spectrum is evident in the presence of $0\nu\beta\beta$, which would be discoverable with a sufficiently calibrated and understood detector. $T_{1/2} = 10^{28}$ years corresponds to $m_{\beta\beta} \sim 10\ meV$, depending on the nuclear matrix elements used.

detector for 60 days, we would expect 2.3×10^4 ν_e captures [118], which, using the excellent position reconstruction in the detector, could measure oscillation patterns characteristic of sterile neutrino oscillations. The 3σ sensitivity to the exposure above is shown in Figure 4.5 along with other current experimental results. We could fully explore the BEST parameter space and this would act as the best probe of the sterile neutrino interpretation of the

gallium data. No evidence of oscillation pattern would suggest the problem lies in the realm of nuclear physics and not a beyond the standard model process.

The Selena experiment offers many interesting science probes that will be competitive with next generation neutrino physics!

4.3 First Realization of an aSe Pixelated Detector

While pixelated aSe detectors do exist in the medical field [136], their noise and pixel size are outside the requirements demanded by a large-scale neutrino physics experiment. Here, we demonstrate the ability to couple aSe to the high performance *Topmetal-II-* CMOS APS.

4.3.1 Topmetal-II-

Topmetal-II- is a pixelated CMOS charge sensor composed of a 72×72 grid of 83 μm pitch pixels; full details of the operation and capabilities can be found in Ref. [137]. The hallmark of the *Topmetal-II-* is an exposed metal electrode connected to a charge sensitive amplifier (CSA) for each pixel. This allows charge generated in a separate detector medium to drift through an applied bias field to the *Topmetal-II-* and be collected by the individual pixels; the charge at each pixel can be measured, providing an excellent spatial map of the charge generation.

Previous experiments have coupled the *Topmetal-II-* to a CdZeTe crystal via a conductive adhesive [138][139] and a Ne-Dimethyl Ether (DME) mixture in a gas electron multiplier [140] to directly measure charge in their detector material. Furthermore, several other proposals have been suggested to incorporate the *Topmetal-II-* chips in high pressure time projection chambers (TPCs) for $0\nu\beta\beta$, such as in the PandaX-III ^{136}Xe TPC [141] or a potential $^{82}SeF_6$ gaseous TPC [142] for the the 3D particle reconstruction of events.

We present here the first work to developing a pixelated aSe sensor using the *Topmetal-II-* readout as a proof-of-concept for further development of dedicated ASICs for the Selena Neutrino Experiment.

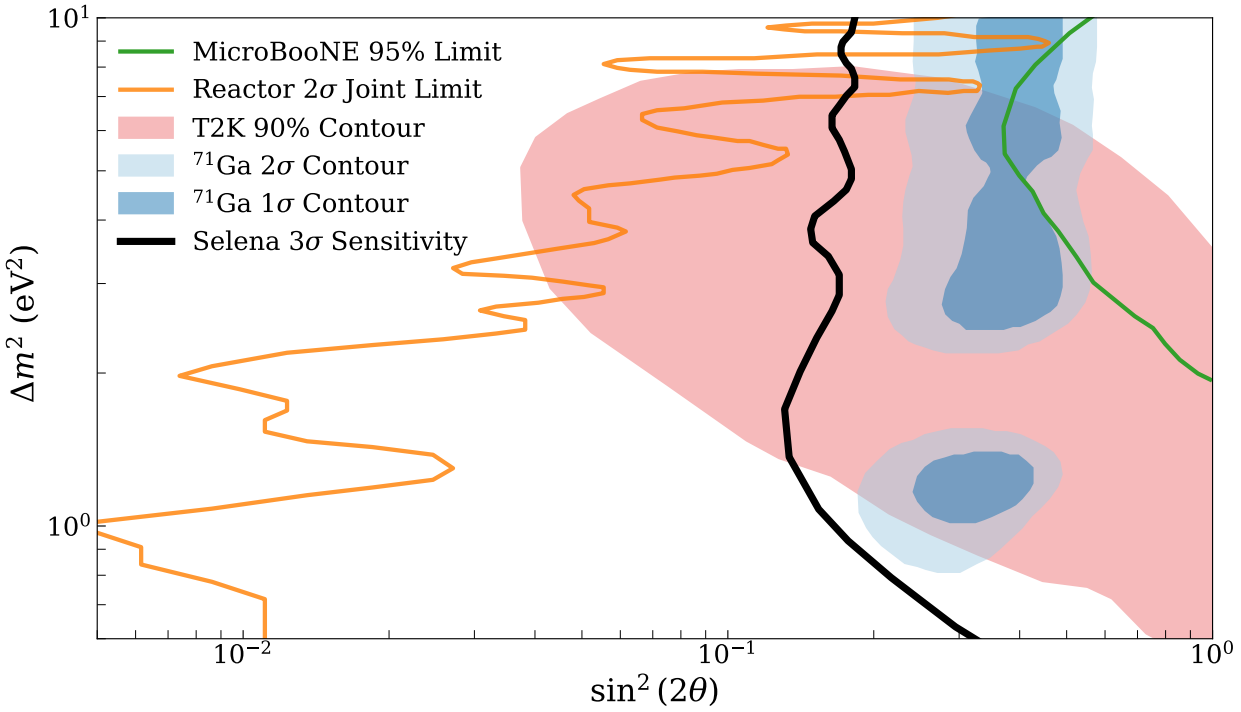

Figure 4.5: Current experimental results on sterile neutrino mixing angle ($\sin^2 2\theta_{41}$) and mass difference (Δm^2_{41}) squared in a 3+1 sterile neutrino model. The joint ^{71}Ga [125] (computed from BEST [126], SAGE [127], and GALLEX [128], the so-called "Gallium Anomaly" experiments) and T2K [124] experiments find some preference for a sterile neutrino and thus are shown as contours (shaded regions) in the parameter space. A joint analysis with full Feldmann-Cousins treatment of reactor data [129] (from the DANSS [130], NEOS [131], PROSPECT [132], STEREO [133], and Neutrino-4 experiments [134]) and MicroBoone neutrino appearance/disappearance data [135] finds no statistical significant preference for sterile neutrinos and place limits on the $\sin^2 2\theta_{14}$-Δm^2_{14} parameters (solid line, region to the right is excluded). The 3σ sensitivity for the 10 ton Selena detector expose to a 3.5 MCi ^{51}Cr for 60 days is shown in black [118]; this represents a direct probe the sterile neutrino interpretation of the ^{71}Ga experiments.

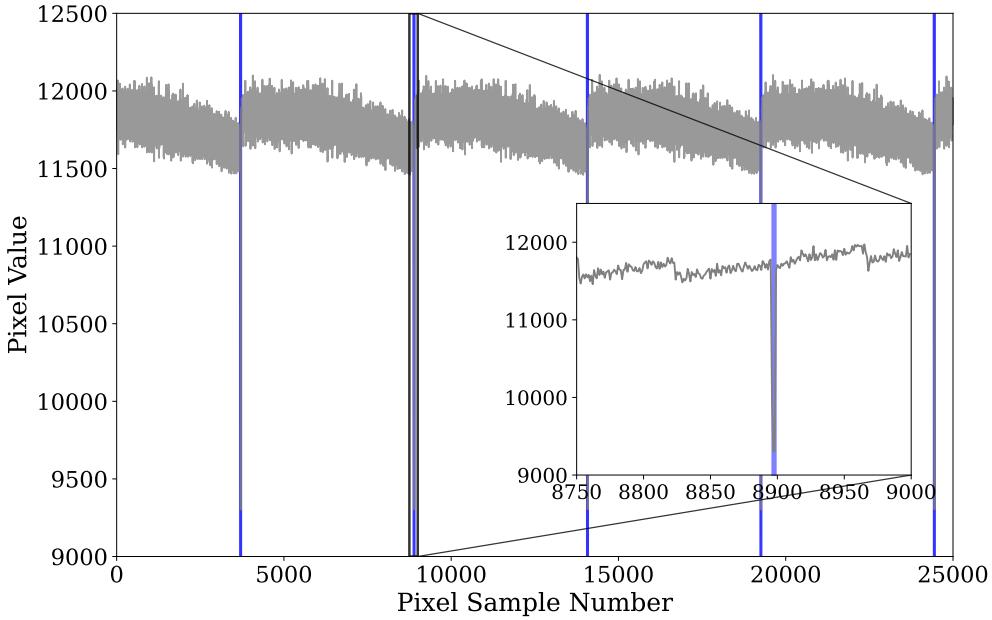

Figure 4.6: Pixel values measured by *Topmetal-II⁻*. The blue regions indicate the locations of the marker pixels.

4.3.2 Topmetal-II⁻ *Rolling Shutter Mode*

Topmetal-II⁻ can be operated under a variety of modes [137], but we exclusively used the analog or "rolling shutter" mode, which will be described here.

The charge measurement from each pixel is multiplexed into a single time series data stream. We start by reading p_1, switch to p_2 and continue this trend until we readout $p_{72\times72}$, the last pixel in the array. The chip then returns to p_1 and the cycle continues indefinitely. A sample of the readout pixel values are shown in Figure 4.6, where a clear periodic pattern is evident indicating the repeated measurements of the same pixel, separated by 5184 measurements. The first three pixels, $p_{1\text{-}3}$, are referred to as marker pixels, and have a significantly lower baseline. They are useful for identifying the start of a frame from the raw waveform. The marker pixels are highlighted in blue in Figure 4.6, and the inset zooms into the region around the marker pixels.

4.3.3 Topmetal-II$^-$ *with aSe Deposition*

The bare die were epoxied to a carrier printed circuit board (PCB) and the pads wirebonded from die to carrier board. The boards edge is standard 0.1" semi-through-hole vias to easily connect to pins on an external breakout board; this carrier board was designed at LBNL.

We covered the wirebonds with a layer of Master Bond EP30HT-LO epoxy. This epoxy was selected for its low outgassing (to meet specifications from Hologic, a company that manufactures aSe flat panel detectors and performs the selenium deposition for us) and high dielectric strength of 440 V/mil (17 V/μm). While the dielectric strength of the epoxy is on the order of the intended field through the aSe bulk, $\mathcal{O}$(10 V/μm), the epoxy is laterally separated from the HV electrode and thus we only expect suppressed fringe fields through the epoxy, making this a suitable choice. After the epoxy was applied, the chips were tested according to procedure outlined in Sec. 4.3.5.1, to verify they were still functional.

Finally the prepared chips were sent to Hologic Inc. for aSe deposition. While their precise recipe is proprietary, the deposition consisted of a 500 μm layer of amorphous selenium deposited on the *Topmetal-II$^-$* chips, followed by a specialized hole blocking layer to prevent charge carriers being injected by the HV electrode, and finished with a gold electrode of $\mathcal{O}$(10 nm) thickness covering an $\sim 5 \times 5$ mm^2 inner area of the aSe. A sketch of the cross section of an individual pixel after deposition is included in Figure 4.9(a).

4.3.4 Experimental Setup

Figure 4.8 provides an overview of the experimental components to run the aSe-*Topmetal-II$^-$* chips. The following sections will discuss each piece in detail.

4.3.4.1 Analog Voltages

Power and control voltages were applied to the *Topmetal-II$^-$* chip by variable DC power supplies through SMA connectors on the breakout board. A list of DC voltages, their purpose, and nominal operating value follows; `avdd` is the analog amplifier bias voltages (3.3

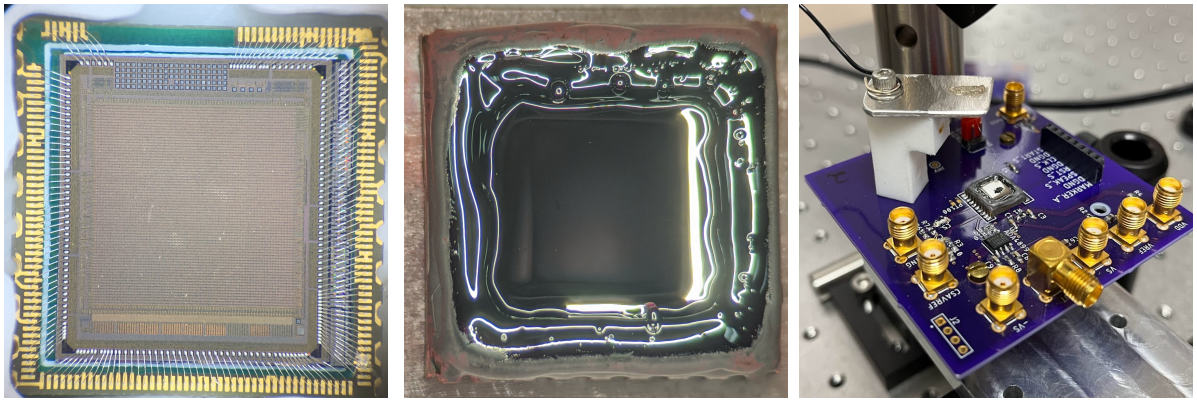

(a) (b) (c)

Figure 4.7: (a) *Topmetal-II⁻* chip wirebonded to carrier board. (b) 500 μm aSe deposited on *Topmetal-II⁻* and epoxy covering the wirebond. (c) Carrier board mounted on our test board to deliver analog and digital signals and readout the chip output. The HV connection discussed in Section 4.3.4.5 is shown on the left portion of the board.

V); `dvdd` the digital components bias voltages (3.3 V); `csa_vref` the reference voltage for each individual CSA and sets the baseline value (810 mV); and `vref` the feedback voltage on amplifier feedback FET (900 mV) [142]. Figure 4.8(b) shows a sketch of the pixel output amplifier. A feedback capacitor C_f integrates the charge arriving at the pixel, and a FET, M_f, acts as a feedback resistor and allows the charge to dissipate off of the electrode. The difference between `csa_vref` and `vref` sets the gate-source voltage, V_{gs} = `vref - csa_vref`, controlling the effective resistance of M_f and setting the decay time, τ, of the charge arriving at the *Topmetal-II⁻* electrode. Increasing (decreasing) V_{gs} decreases (increases) the amplifier decay time.

One final analog connection is to the pixel guard ring (`gring`). The guard ring is a metallic layer surrounding the active pixel sensor. This allows for electrical isolation, DC biasing to shape the electric field in the detector medium, and injection of calibration pulses. The `gring` to electrode structure forms a capacitor of 5.5 fF, verified by the IC design

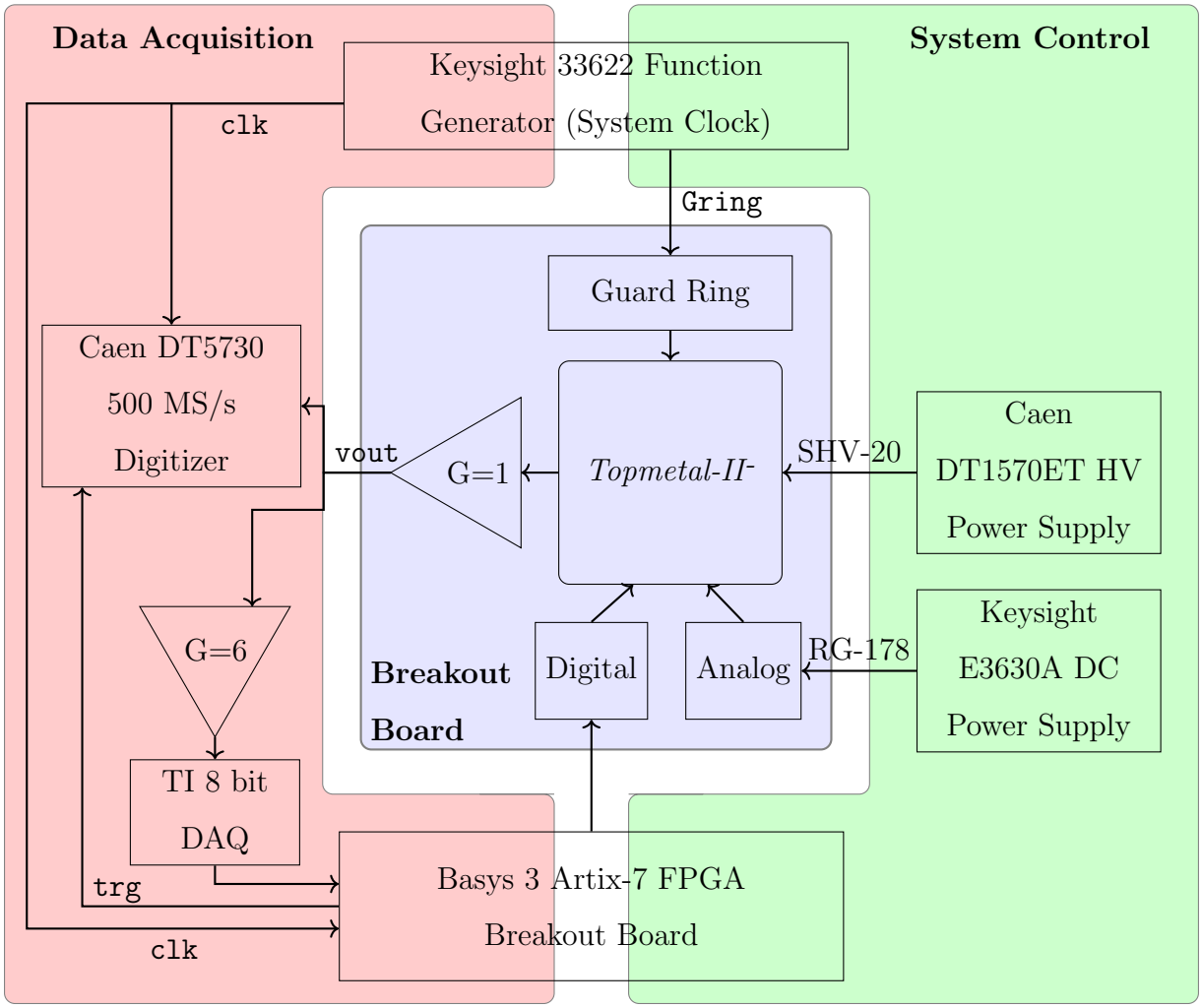

Figure 4.8: *Topmetal-II-* operation schematic. The pads on the carrier board are soldered to a breakout board. The HV is delivered by a Caen DT1570ET directly to the detector electrode. Analog and digital signals are applied via the breakout board from DC power supplies and an Artix-7 FPGA. The output of the chip is split: one signal goes to a Caen DT5730 8 channel, 14 bit, 500 MS/s digitizer; the other goes to a rough 8 bit digitizer used for triggering. The FPGA monitors the output of this 8 bit DAQ and compares the current pixel value to the pixel value in the previous frame, triggering if difference is above a customizable threshold. One channel of the Keysight 33622A Function generator acts as the clock to synchronize the system.

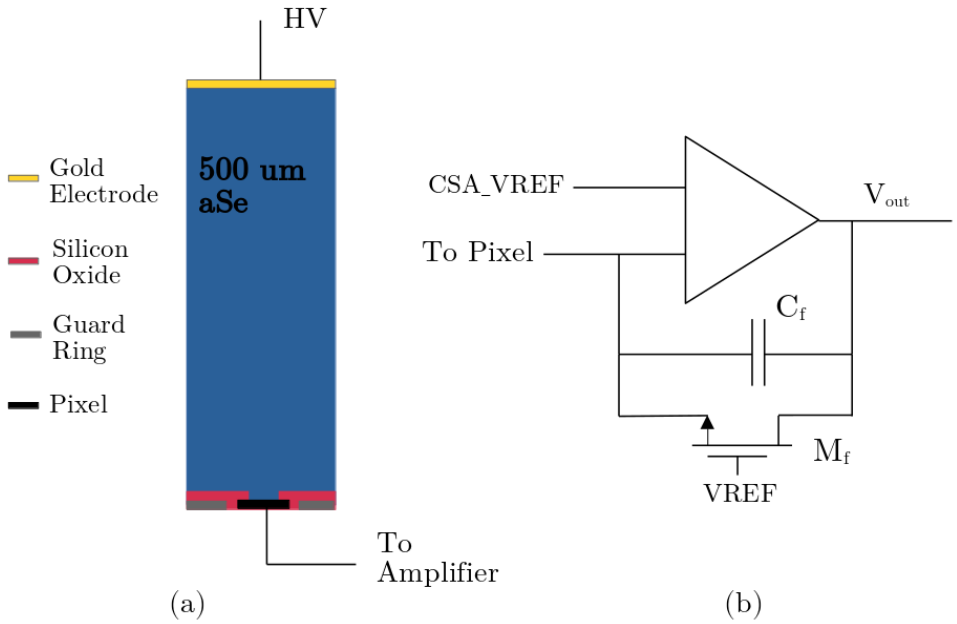

Figure 4.9: Sketch of (a) the cross section of a *Topmetal-II-* pixel after aSe deposition and (b) a simplified schematic of the *Topmetal-II-* CSA connected to each pixel when operated in analog mode.

software and COMSOL finite element analysis (FEA) simulation. Therefore, we can inject a known and calibrated pulse on the electrode and measure the properties of the amplifier on an individual pixel by measuring the output waveform of that pixel. This structure is extremely useful when testing and characterizing the chip/pixels.

4.3.4.2 Digital Voltages

For our measurements, we operated the *Topmetal-II-* in "analog mode," meaning we scan through the pixels, reading the analogue output voltage of the CSA of each pixel. However, there is still a skeletal digital operation to start-up the chip and switch pixels. We used three digital signals for the startup sequence: `RST`, `START`, and `clk`. All digital logic is controlled on a Basys 3 Artix-7 FPGA test board and the signals are sent to the *Topmetal-II-* chip via

the breakout board.

A central clock, `clk`, controls the timing of all digital operations. This can either be the FPGA internal clock (100 MHz, typically used in debugging) or an external clock from the Keysight 33622A Function (variable frequency up to 120 MHz, typically in the 10-50 MHz range) when used with the DAQ hardware. Logic is processed on the falling edge of the clock pulse.

The control logic can be summarized by the state machine diagram shown in Fig. 4.10. During initialization, `RST` and `START` are held low for a clock cycle, `RST` is held high for the next clock pulse to initialize the scan module, both are low for the next clock pulse, and finally `START` is set high for a clock cycle to start the scan at pixel (0, 0). After initialization `RST` and `START` are held low. During normal operation (s_4), each falling edge does not change the system state, instead it moves the pointer of the output amplifier to the next pixel. For example, if we are currently reading the output voltage of pixel n, the falling edge of the clock changes the readout to pixel $n + 1$. This cycle continues indefinitely, returning to the first pixel after all pixels in the detector have been read. Finally, since the Artix-7 FPGA tracks the current pixel address, we implemented the option (s_5) to stop all clock cycles once a specific pixel number is reached; this allows us to measure the performance of specific pixels, which was paramount for detector calibration (see Sec. 4.3.5.1).

4.3.4.3 Data Acquisition

Data was acquired on a single channel of a 8 channel, 14 bit, 500 MSample / s, 2 V_{pp} dynamic range Caen DT5730 Digitizer. While the digitizer generates its own internal 50 MHz clock, we supplied an external 50 MHz signal from the Keysight 33622A Function Generator to synchronize with the other system clocks. The maximum buffer capacity for a single channel is 640 kS.

The output values were sampled and stored in a circular buffer. When the digitizer triggered (see Section 4.3.4.4), a user defined fraction of the buffer is reserved for pre-trigger values, and the rest for post-trigger. This functionality allows us to capture the detector

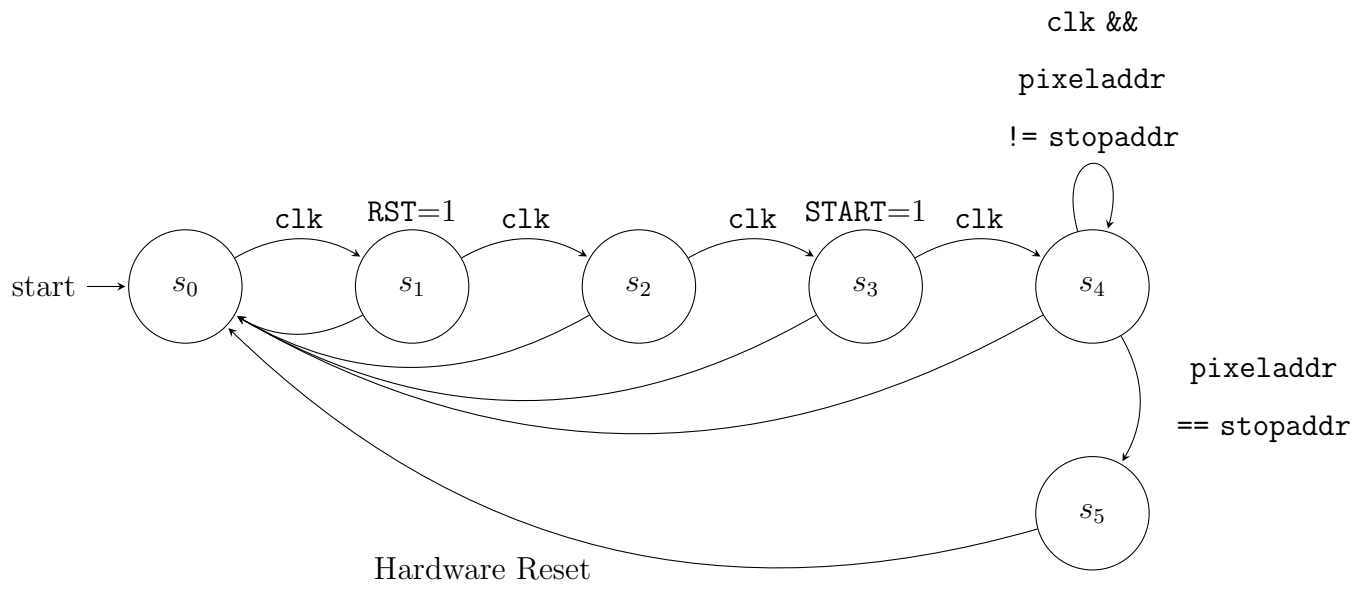

Figure 4.10: State machine digital logic for controlling the *Topmetal-II⁻* chip. In each state s_i, all digital signals are set low unless explicitly stated otherwise. The falling edge of the `clk` signal transitions between states. $s_{0\text{-}3}$ are initialization states, s_4 is the nominal operating states, and s_5 is a "freeze" on an individual pixel. Transition back to the start is accomplished by a reset on the Artix-7 FPGA.

status immediately before and after a trigger. After a trigger, the data was transferred to the DAQ computer at $\sim$ 30 MB/s; if the buffer is full, no data can be acquired during this transfer.

The digitizer readout schema is easily configurable in a custom wrapper around the Caen Software Development Kit (SDK) developed for this experiment; the code to control the readout can be found at https://github.com/selena0vbb/UWTopMetalDrone

4.3.4.4 Triggering

While the Caen digitizer comes with out-of-the-box triggering options, the nature of multiplexing 72×72 different pixels with slight variations in their baseline values (see Figure

4.6 for example) into a single data stream, triggering on changes in pixel values is impossible with that hardware. Furthermore, continuously recording and dumping data to disk to search for events in software is not suitable as the data creation rate is much faster than the data transfer rate, resulting in a paltry 2% duty cycle. Therefore, we designed an external pixel-level trigger. We split the signal from the output with a 50 Ω RF splitter, sending one signal to the digitizer and another to a secondary trigger amplifier. The trigger amplifier has a DC offset input to trim the baseline of the *Topmetal-II⁻* output and amplify (with a gain of six) the signal around the baseline value. The amplified trigger signal is sent to a fast, 8 bit TI analog-to-digital converter (ADC) breakout board; this ADC uses the same 50 MHz clock that is synchronizing the rest of the system. The 8 bit digital value is passed in parallel to the Artix-7 FPGA.

The FPGA interprets the 8 bit TTL signals from the TI ADC as the voltage of the current pixel. We compare the difference of this value to the previous value of the specific pixel stored in the FPGA DRAM to a user defined trigger threshold. In other words, the trigger condition is

$$p_{ij}[t] - p_{ij}[t-1] < T_{\text{trig}}, \tag{4.5}$$

where p_{ij} is the pixel in the ith row and jth column in the current or previous frame (t or $t-1$) and T_{trig} is the trigger threshold. We trigger when the current value is less than the previous value as the charge from the aSe results in a negative polarity pulse. When we trigger we transfer data from the entire sensor, not just the triggered pixel.

4.3.4.5 High Voltage

The charge generation, and therefore the signal-to-noise ratio at each pixel, in aSe is highly dependent on the electric field applied [114]. We aimed to operate at $\mathcal{O}(10\ \text{V}/\mu\text{m})$, corresponding to a bias voltage of $\mathcal{O}(5\ \text{kV})$ for the 500 μm samples. A Caen DT1570ET High Voltage Power Supply with an upper limit voltage ripple of $\pm 20\ \text{mV}_{\text{pp}}$ provides the high

voltage potential. An RG-213 coaxial cable with a Lemo FFB.3S.415.CTAC11 HV a SHV-20 connection brings the HV from the power supply to a vacuum chamber that the chip is installed in. For any voltage over $\sim$ few kV, operate the detector under vacuum with a pressure $< 10^{-4}$ mbar.

Inside the vacuum chamber, a stainless steel cable with kapton sheath runs from the feedthrough to an aluminum plate on top of a $\sim$ 5 cm tall Teflon stand mounted on the breakout board. A 1 mil aluminum wire designed for wirebonds is connected to the aluminum plate with silver epoxy and to the gold electrode on the aSe sample with conductive carbon paint. We found this design limited mechanical pressure on the soft aSe surface and was robust to vibrations around the lab that could cause discharge.

The resistivity of this aSe sample was measured to be 3.4×10^{13} Ωm at an electric field strength of 40 V/μm [115]; using the cross sectional area under the 5×5 mm^2 electrode we can estimate an upper limit of 30 pA of current through the detector at a voltage of 20 kV. The 1 mil wire is suitable for these low levels of current.

4.3.5 Results

We performed detailed testing of the pixel electronic performance, trigger efficiency, and response to radioactive sources on our workhorse chip TM02.

4.3.5.1 Pixel Calibration

For calibration, we injected a known pulse on the guard ring and measured the response on the pixel array. The stray capacitance between the guard ring and pixel, C_{gs}, was calculated with a Finite Element Analysis (FEA) as 5.5 fF [137]. The charge on the *Topmetal-II-* electrode is $q = C_{gs}V$.

We scanned over the pixel array, stopping at each individual pixel to inject a pulse with 30 mV_{pp} at 5 Hz with a 50% duty cycle. We made a fast measurement, $\mathcal{O}(10\ \mu\text{s})$ with the Caen digitizer, triggering on the rising edge of the pulse and centering the trigger in the recorded waveform to get the pixel baseline, gain, and rise time of the signal for the given

pixel. We also made a slow measurement $\mathcal{O}(10\text{ ms})$ with an oscilloscope to fit the pixel decay time of the pixel. For the rise time we fit the function

$$V(t) = C + A\Theta(t - t_0)\left(1 - e^{-\tau_r(t-t_0)}\right), \tag{4.6}$$

where C is the pixel baseline, A is the pulse amplitude, τ_r is the rise time, t_0 the pulse injection time, and Θ is the Heavenside step function. Since the time scale of this rise is $<< \tau_d$, the pulse decay time, we do not need to consider decay as part of this function. However, for the decay time measurement, we modify the fit function to

$$V(t) = C + A\Theta(t - t_0)\left(1 - e^{-\tau_r(t-t_0)}\right)\left(e^{-\tau_d(t-t_0)}\right), \tag{4.7}$$

with the addition of τ_d. The distributions of the calibration parameters across all pixels in the detector for `vref` = 900 mV and `csa_vref` = 810 mV are shown in Figure 4.11. These are the same voltage parameters used in the remaining sections of this chapter. For the results in Section 4.3.5.3, we perform our search in "well behaved pixels," meaning the baseline, gain, and τ_r are within $\pm 3\sigma$ of the mean values; this cut keeps $\sim 98\%$ of pixels. Notably though, τ_f varies widely between pixels and is extremely sensitive to the amplifier voltages values.

Finally, we can use the results here to compute the image calibration constant

$$k = \frac{A}{V_{in}} C_{gs} = \frac{30.56\text{ mV}}{30\text{ mV}} \times \frac{5.5 \times 10^{-15}\text{ C}}{1\text{ V}} \times \frac{1\text{ e}^-}{1.6 \times 10^{-19}\text{ C}} = 35.0\text{ e}^-/\text{mV} \tag{4.8}$$

that we will use in the following sections to characterize the detector and ionization events in units of electrons.

4.3.5.2 Trigger Efficiency

To measure the trigger efficiency, we injected variable amplitude signals in rolling shutter mode where the pulse width was much greater than the pixel switching frequency. We

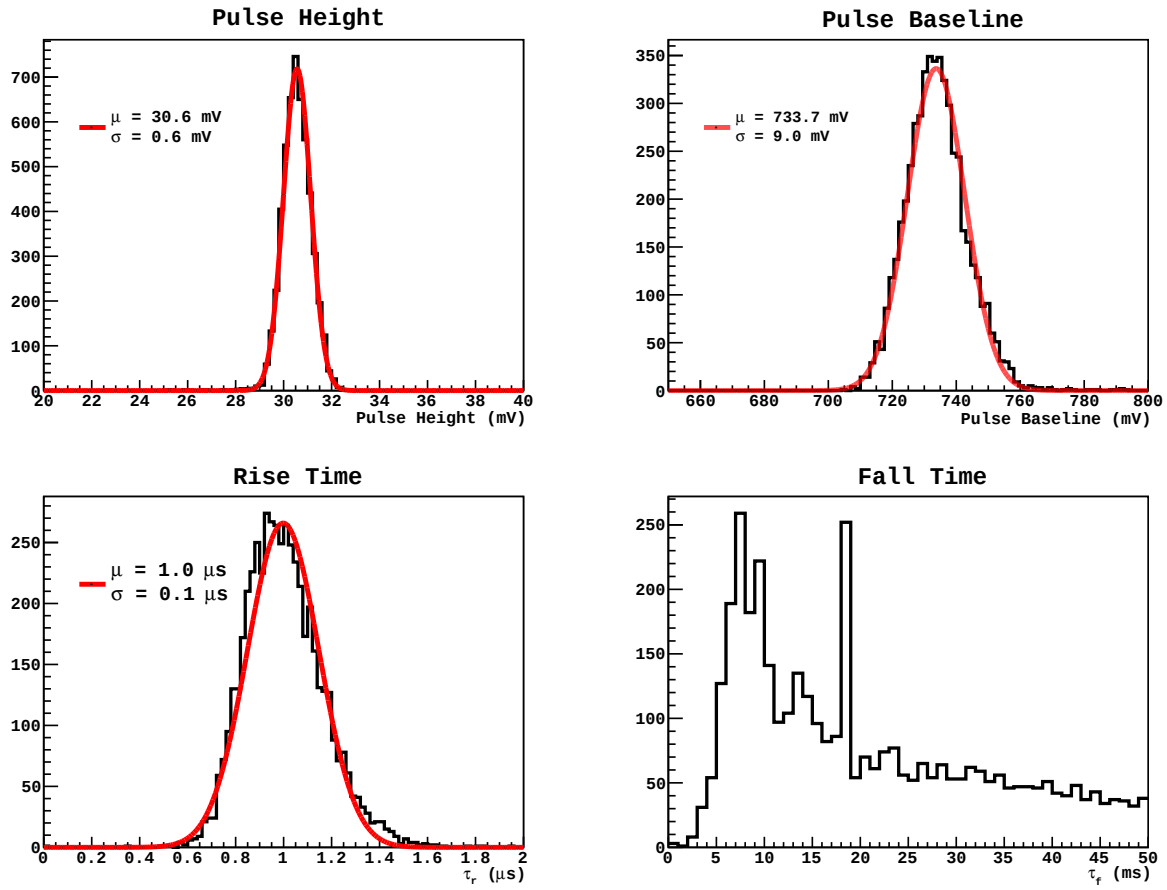

Figure 4.11: Calibration of TM-02 at operation voltages of `vref`=900 mV and `csa_vref`=810 mV. We characterized the pulse amplitude ($A = 30.6 \pm 0.6$ mV), baseline ($C = 734 \pm 9$ mV), rise ($\tau_r = 1.0 \pm 0.1$ μs) and decay (τ_d) time to a 30 mV square pulse injected on the guard ring. Based on the large spread and distribution of τ_d, it does not make sense to characterize the parameter with a Gaussian distribution.

counted the number of pixels triggered compared to the number of pixels readout while the injected pulse was high. We split a square wave from the function generator, sending one signal to the guard ring and the other to the digitizer, allowing us to trigger the digitizer on this injected pulse and centered the DAQ window around it. We also recorded the `vout` from the *Topmetal-II*$^-$ chip and the external trigger out signal from the FPGA.

We fit the output *Topmetal-II*$^-$ waveform to a sawtooth wave [143] (electronic transient) plus a negative square pulse (injected signal) convolved with the detector rise/fall time response. The mathematical fit function is for the output waveform is

$$V(t) = C + \frac{2A_1}{\pi}\arctan\left(\cot\left(\frac{(t-t_0)\pi}{T}\right)\right) - A_2\left(\Theta(t-t_1)\left(1-e^{-\tau_1(t-t_1)}\right) - \Theta(t-t_2)\left(1-e^{-\tau_2(t-t_2)}\right)\right), \quad (4.9)$$

where C is the waveform baseline, A_1 the amplitude of the sawtooth waveform, t_0 the sawtooth offset, T the sawtooth period defined by the pixel scan rate, A_2 the injected pulse amplitude, $t_{1(2)}$ the pulse rising (falling) edge times, and $\tau_{1(2)}$ the rising (falling) time constants. In the range of $[t_1, t_2]$ we counted the number of pixels (n_t) where the trigger out value from the FPGA is > 600 mV (i.e. trigger signal is high) and compared to the total number of pixels readout in the injected pulse window (n_p). We calculated the efficiency, ϵ, as

$$\epsilon = \frac{n_t}{n_p} \quad (4.10)$$

We varied the amplitude of the injected signal to compute the efficiency as a function of electrode charge. For each voltage, we injected 100 pulses uniformly distributed in time, but asynchronous to the pixel scan clock, to hit all pixels in the array; each pixel was hit on average of ten times. The trigger efficiency as a function of injected charge is shown in Figure 4.12 for different trigger thresholds. For each trigger threshold, we fit the efficiency to a Gaussian CDF multiplied by a free amplitude; the mean (μ) and standard deviation (σ) fit parameters are also shown in Figure 4.12. For a threshold of 3 ADU, the 50% efficiency occurs for a pixel charge of 625 e^- with an 88 e^- RMS value. This noise is higher than the *Topmetal-II*$^-$ noise performance [137] because there no data processing of the pixel value, we take the difference of pixel value in two adjacent frames increasing the noise by $\sqrt{2}$, and the 8-bit TI DAQ is not a particularly high performance digitizer. Ultimately,

the higher noise on the trigger DAQ causes some penalty on the efficiency, but the event reconstruction is completed with lower noise in software so this does not effect the quality of the energy reconstruction. Figure 4.12 also shows a trigger plateau < 1 for all thresholds. *Topmetal-II⁻* was designed to collect electrons [137], and while it works when collecting holes, the rise/decay time is not the same for each polarity. The falling edge (start of the injected signal) responds more slowly than the rising edge (end of injected signal), so the time the output is above the trigger threshold is $< t_2 - t_1$.

We additionally measured the number of false-triggers, that is triggers occurring outside the $[t_1, t_2]$ window, and found that for a trigger threshold of ≥ 3 ADU, there were no false triggers. For the spectroscopy measurements in Section 4.3.5.3 we used a 3 ADU threshold.

4.3.5.3 Radioactive Sources

For energy calibration to radioactive sources, we exposed the *Topmetal-II⁻* with aSe to a ^{57}Co γ and ^{90}Sr β source. We operated with at 2 kV high voltage (4 V/μm field strength) to be careful with the chip. The sampling rate $f_s = 500$ MHz and pixel scan rate $f_p = 25$ MHz resulted in 20 samples per pixel per frame, a frame rate of $f_p/n_{pix} \sim 5$ kHz, and 5 complete frames stored per trigger. We biased the detector at `vref` = 900 mV, `csa_vref` = 810 mV, `gring` = 0 V, and $V_{hv} = 2$ kV. We recorded 640 kS per trigger, and 50 triggers per file.

Data processing began by converting the raw waveform into pixel values. After a pixel switch, marked by a positive spike in the waveform due to the pixel switching electronics, we discarded the first 10 samples and took the mean of the next 10 to obtain the pixel value. An example of this procedure on a few pixels can be seen in Figure 4.13(a). Using the marker pixels to locate the beginning pixels of the image we converted these pixel values into image frames. We took the median image (i.e. med(p_{ij}) across all k frames created in a single file) to create a low noise pedestal image which we then subtracted off individual frames to remove the spatial transient from the current into the column buffer. For the five recorded frames, the first is pre-trigger and should be only noise, and in the next four we search for persistent low pixel values in all frames sufficiently far (4σ) from the noise distribution. We

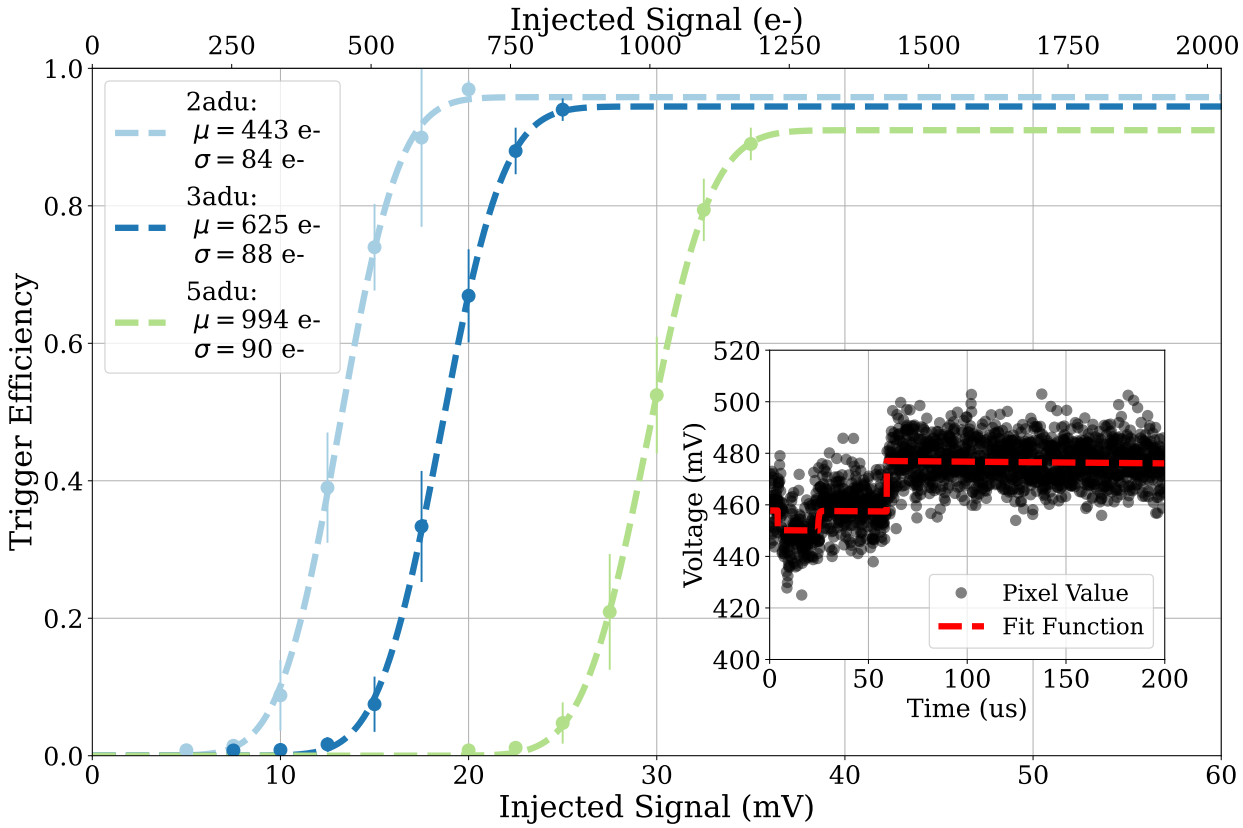

Figure 4.12: *Topmetal-II*$^-$ trigger efficiency as a function of injected voltage (and charge, using the calibration performed in Section 4.3.5.1) via pulses on the `gring`. Different trigger thresholds are shown. A sample pulse with amplitude of 10 mV and t_1 (t_2) of 4 μs (24 μs) injected on the guard ring for the trigger test, as described in the text, is shown as the inset.

cluster contiguous pixel that satisfies the $> 4\sigma$ threshold; the position and charge of these clustered pixels were recorded as events. The sum of the clustered pixels in each of the four frames were fit with a step pulse convolved with decaying exponential; the peak amplitude was converted to charge using the calibration from Section 4.3.5.1 and represented the event energy.

For the ^{57}Co data, we were searching for the monoenergetic 122 (136) keV γ peak with 85.6% (10.7%) intensity [144] to replicate and expand on the measurements made in Ref.

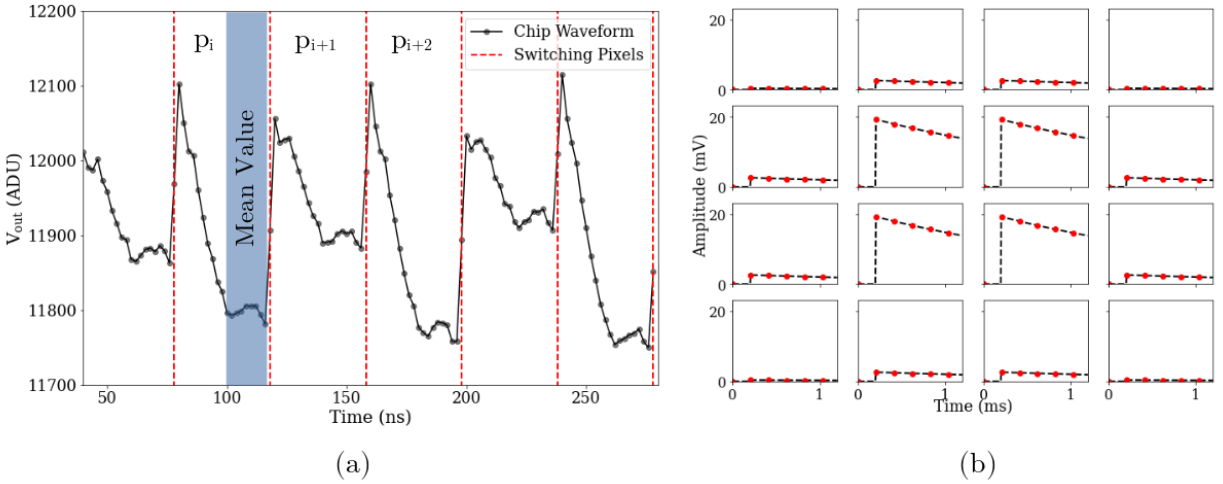

Figure 4.13: *Topmetal-II⁻* waveform and image processing. (a) $\sim$ 200 ns of the *Topmetal-II⁻* waveform. The spike and decay in the waveform is an electronic transient from switching between pixels being readout. We waited 10 samples for the output to settle, and then took the mean of the next 10 sample to be the value of p_i at the given time. (b) The pixel values were de-multiplexed into into the correct ij location in the image. Each pixel records a time series with the frame sampling rate. Shown here is a toy example of the data (red) and fit (black) of multiple pixels being hit with an ionization event.

[114]. We placed a $\sim$ 0.5 μCi ^{57}Co source $\sim$ 5 cm above the detector. We acquired data in a number of different operation conditions, but we took several days of exposure in the aforementioned configuration. Unfortunately, the investigation into the ^{57}Co spectrum never yielded a clear 122 keV γ photoelectric absorption peak. We posited that insufficient charge collection efficiency distorted the mono-energetic peak; see Section 4.3.5.4 for a more detailed investigation.

We also irradiated the detector with a $\sim$ 25 μCi ^{90}Sr-^{90}Y β source. ^{90}Sr undergoes β decays with a long half life (29 years) with endpoint 546 keV into ^{90}Y with a short half life (64 hours) into stable ^{90}Zr with endpoint energy of 2279 keV. The isotopes are in secular

equilibrium since $T_{1/2}(^{90}\text{Sr}) >> T_{1/2}(^{90}\text{Y})$ and so we expected the same number of decays from each isotope. The MeV scale βs of ^{90}Y are have an mean range of ~ 1.4 mm, meaning they will likely span multiple pixels in the xy plane. We clearly observed single electron events with with Bragg peaks—characteristic of electron tracks—spanning multiple pixels in the detector. The ^{90}Y βs are minimum ionizing similar to $Q_{\beta\beta}$ events in ^{82}Se, so in principle we could study the resolution effects of charge fluctuations along a track with this source; however, we did not operate at high enough HV, with sufficient charge collection, or small enough pixel pitch to measure this effect.

Some sample tracks from the ^{57}Co and ^{90}Sr exposures are shown in Figure 4.14. This is the first demonstration of single electron/photon sensitivity with an amorphous selenium imager.

4.3.5.4 Collection Efficiency

We tested the charge collection hypothesis with an FEA electrostatic simulation completed in COMSOL Multiphysics. A sketch of the pixel geometry is included in Figure 4.17(a); the pixel geometry was generated from an image provided by the foundry and input from the chip designer, but we were asked to not publicly share it. The pixel is a 25×25 μm metallic square electrode, surrounded by 1 μm layer of SiO_2 and another 1.5 μm metallic layer for the `gring`. There are various other oxide and metallic structures (held at the same potential as the `gring`) included in the sketch. Below the pixel is 5 μm of SiO_2 before a ground plane, and above is 500 μm of aSe topped by a gold electrode. We applied periodic boundary conditions on the edges of the pixel. The potential and field lines for the yz plane at $x = 0$ for an increasing guard ring voltage is shown in Figure 4.15.

For the simulation, we set the potential of the HV electrode to 1 V, collection electrode to 0 V, and guard ring to potentials between $[0, 1]$ V. To measure the collection efficiency we simulated a test charges in a grid on the xy plane starting at $z = 500$ μm, drifted them through the aSe in the $-\hat{z}$ direction following the dynamics that the charge velocity is proportional to the electric field, and tabulated where the charge ended. The ratio of charge

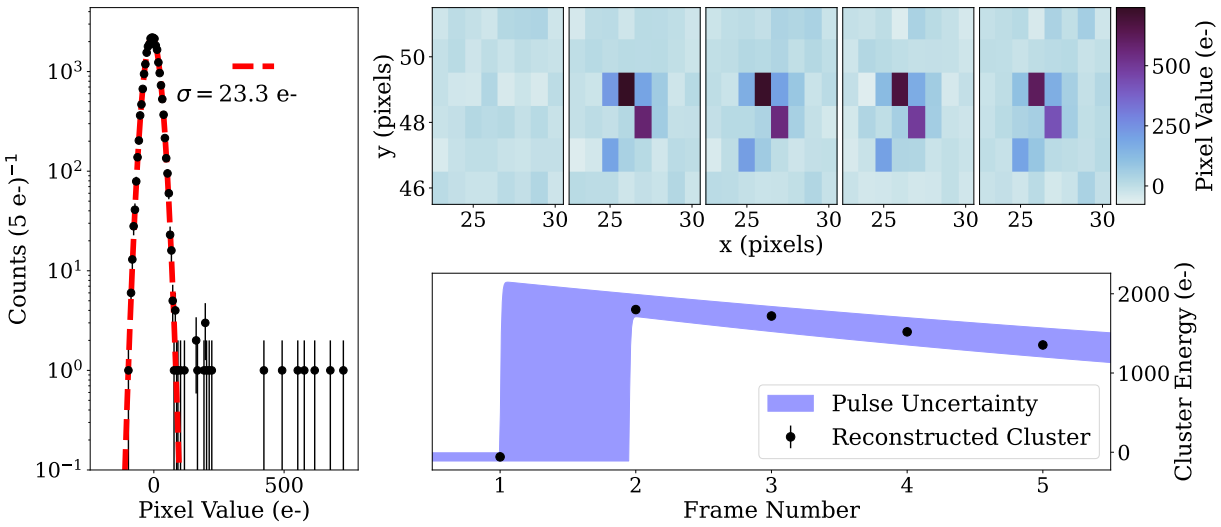

(a) ^{90}Sr-^{90}Y β track.

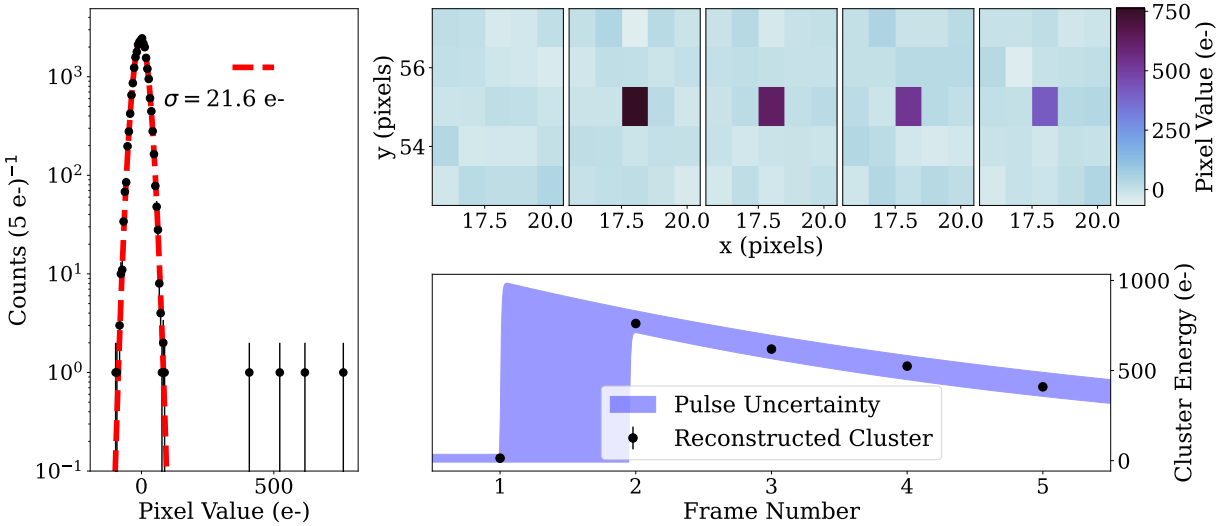

(b) ^{57}Co γ track.

Figure 4.14: Sample events. The left pane is the distribution of all pixel values recorded for a trigger. Pixels without charge are distributed as a Gaussian with ~ 23 e$^-$ of noise; values far from this distribution are the event pixels. The top frames are a zoomed region around the event for five consecutive frames. The first frame is pre-trigger and represents noise only and the remaining show persistent charge in hit pixels. The bottom frame is the cluster energy (e$^-$) vs. frame number and the reconstruction parameters with uncertainty.

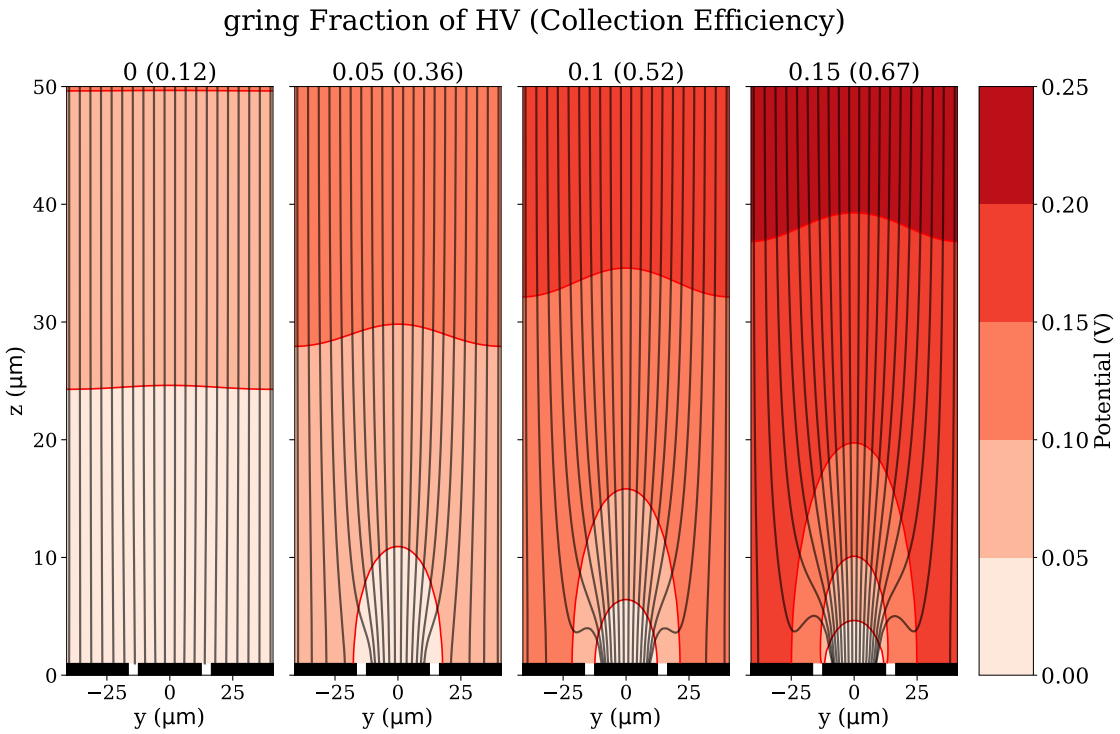

Figure 4.15: yz plane at $x = 0$ of the electrostatic simulation of the *Topmetal-II⁻* chip at various guard ring voltages. The potential (contour) and electric field (lines) show the increasing voltage relative to the HV increases the collection efficiency of the pixel. At the bottom of each plot is the electrode (centered) and the guard ring (sides). The distance between the electrode and guard ring is artificially increased for viewing purposes—the spacing in the simulation is 1 μm.

ending at the collection electrode to total charge simulated is the collection efficiency. We found that for a guard ring potential of 0 V (the mode of operation in the previous section), the collection efficiency is $\sim 10\%$. Figure 4.16 shows the relationship between `gring` potential and collection efficiency. In the COMSOL simulation, we also computed the weighting potential ($V_{\text{collect}} = 1$, all other electrodes grounded) which gave us the charge induced at the electrode by a test charge drifting through the detector following the framework of the Shockley-Ramo Theorem [145][146][147]. The detector response to a 122 keV γ-ray is the

convolution of the energy deposited along the track with this detector response. The stopping power of the γ-rays is 2.2 MeV cm^2/g [148] resulting in an electron with ~ 110 μm range and can easily traverse between the high/low collection regions. Thus when the contributions to the signal from energy depositions along the track are summed, the charge that does not get collected degraded the energy reconstruction and and limit the ability to accurately measure the event energy.

4.4 Future Work

We demonstrated the ability to couple a low noise CMOS APS sensor to amorphous selenium and measured single photons and electrons in a 500 μm sample of aSe. This was a crucial demonstration for the feasibility of the Selena experiment and an important benchmark in the path to a large neutrino experiment.

The next critical step is improvement in the detector collection efficiency and γ/β energy measurements. While the *Topmetal-II*$^-$ has been an immensely useful tool, it was not specifically designed for amorphous selenium operation or our science goals. Therefore, we are designing a dedicated CMOS sensor with the Google/SkyWater open source design kit of integrated circuits, which provides us with complete control over the chip design. We will leverage components of the *Topmetal-II*$^-$ structure to achieve the same excellent noise parameters, but will alter the pixel geometry to improve the collection efficiency and reduce the pixel pitch needed for the science goals. The ratio of electrode and guard ring area to the total pixel area is the critical geometric parameter to design; for good collection efficiency, we aim to maximize the former and minimize the latter. We performed a similar electrostatic simulation discussed earlier on two possible pixel designs shown in Figure 4.17. The first is a 35 μm pitch pixel with 25 μm electrode length, surrounded by 4 μm of oxide and then 1 μm of metal layer for the guard ring. While the oxide width could be reduced to marginally increase the collection efficiency, the spacing reduces the parasitic capacitance contribution of the guard ring and increases the allowable applied voltage before the oxide starts to break down. This geometry yields a base 69% and full collection efficiency at a

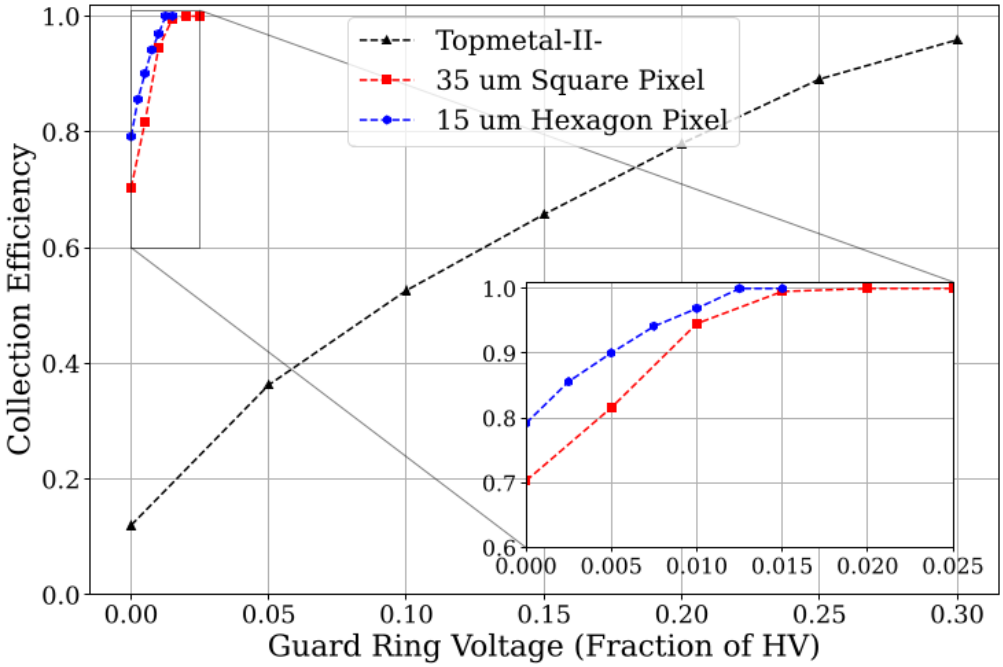

Figure 4.16: Collection efficiency as a function of `gring` voltage for different pixel geometry using the procedure described in the text. The `gring` fraction is specifically for a 500 μm sample—for other thickness the electric fields would need to be rescaled. The small size of the electrode relative to the pixel pitch of the *Topmetal-II*$^-$ hurts the collection efficiency and even relatively high `gring` potentials struggle to yield sufficient collection efficiency. However, with the freedom to design our own pixel structure, we could create the geometries shown in Figure 4.17 which yield much better collection efficiencies (red and blue points) for `gring` potentials of $\sim 1\%$.

guard ring potential of 2% of the HV electrode (for a 500 μm sample of aSe). Additionally, we simulated a hexagonal 15 μm pixel pitch, which is what we proposed in Ref. [118] for the final experiment pixel design. The electrode was 12 μm long surrounded by 1 μm of oxide and a 500 nm metal `gring`, which gives a base efficiency of 75.3% and full collection at a

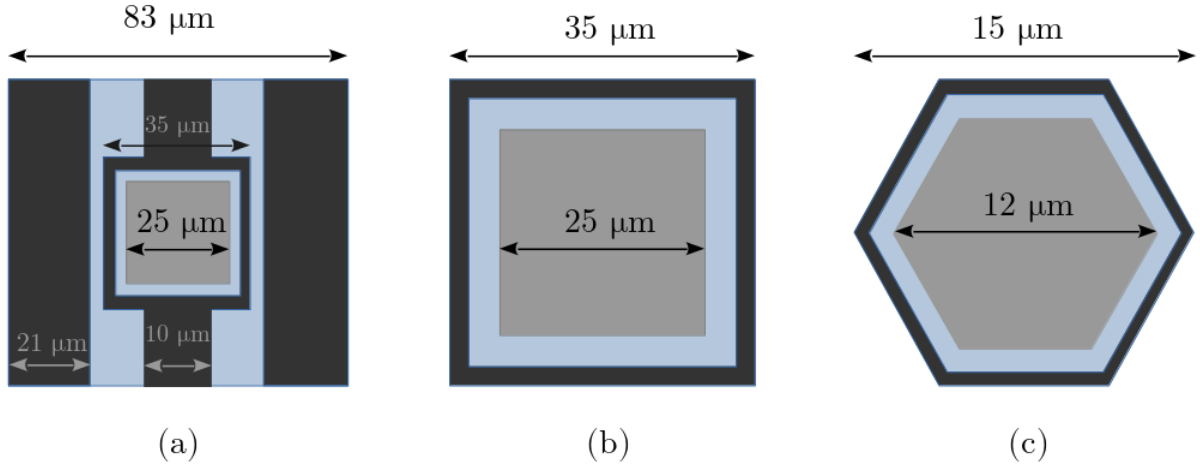

Figure 4.17: Pixel structures for current and future CMOS detectors showing the electrode (light grey), SiO_2 (blue), and `gring` (dark grey). (a) The existing *Topmetal-II⁻* chip, (b) a proposed 25 μm square electrode surrounded by 4 μm of Si oxide and a 1 μm guard ring, and (c) the final 12 μm hexagonal pixel surrounded by 1 μm of Si oxide and a 0.5 μm guard ring.

`gring` bias of 1.2% of the HV.

Upon improving the charge collection, we will continue the calibration campaign of aSe. We plan to expose the samples to different γ energies across the neutrino spectroscopy energy range to understand the energy response in the full ROI. Additionally, the smaller pixel pitch will allow us to study positional energy fluctuations along track position to verify the model proposed in Ref. [115], which is critically important to understand for the final 1.1% resolution we are targeting at the $Q_{\beta\beta}$ energy.

Finally, future generations of CMOS chips will incorporate more features to help with energy reconstruction and event identification. Some examples include onboard signal digitization, onboard pixel level triggering, time of flight recording, sample and hold measurement, and DAC tuning of the CSA effective τ per pixel[118][149].

Chapter 5

CONCLUSION

We have shown significant progress on beyond the Standard Model searches with semiconductor detectors.

With DAMIC at SNOLAB, using the largest CCD exposure (10.93 kg days) ever acquired for a dark matter search, we made considerable progress on the CCD DM campaign. We developed a strong understanding of the CCD response, including a previously unconsidered partial charge collection region on the backside of the CCD, which was one of the main systematic uncertainty for the WIMP search. We created a robust background model based on radioactive assays, activation studies, and the measured ionization spectrum above 6 $\mathrm{keV_{ee}}$. We used this model for $E \in [0.05, 6]$ $\mathrm{keV_{ee}}$ for our final WIMP search where an unexpected population of 17.1 ± 6.7 ionization events, consistent with a decaying exponential bulk population with decay length 67 ± 37 $\mathrm{eV_{ee}}$, was observed. None of the systematic checks we performed gave an indication of the origins of these events. Despite the excess, we used this data to set the most stringent limit on the $\sigma_{n-\chi}$ cross section with a silicon target below 9 $\mathrm{GeV/c^2}$ and further constrained the WIMP interpretation of the CDMS-II silicon excess.

Additionally, we deployed four, ~ 9 g, skipper CCDs in two independent, low background environments at SNOLAB and LSM to take dark matter data with $\mathcal{O}(0.1\ \mathrm{e^-})$ readout noise and $\mathcal{O}(10^{-3}\ \mathrm{e^-/pix/day})$ dark current. We used the SNOLAB CCDs to take the most massive **skipper** CCDs exposure of 3.1 kg days to better understand the previously observed excess at SNOLAB. We developed an analysis procedure to perform a noise free DM search with 10% clustering efficiency at 6 $\mathrm{e^-}$. We found another conspicuous increase in the event rate in both the CCD bulk and on the surfaces that was consistent with events spatially and temporally uniformly distributed. We measured 11 (15) bulk events below 200 (400) $\mathrm{eV_{ee}}$.

We found the bulk events could be characterized by a decaying exponential of 12.3 ± 3.9 events with decay length 89 ± 30 eV_{ee}. This excess was consistent with the bulk events measured in the 11 kg day exposure and suggests a common origin of the two excesses. This is a fascinating result and important for the future of CCD dark matter experiments. Further studies are underway to attempt to understand underlying cause of the events. At LSM, we set limits on light DM-e^- scattering with an 85.23 g day data set and robust analysis with many cross-checks by different institutions. This data resulted in world leading limits the bewteen 1.6-1000 MeV/c^2 for the ultra-light and 1.5-15.1 MeV/c^2 for the heavy mediator. We continue to demonstrate the power of CCD technology in sub-GeV dark matter searches.

On the neutrino physics side, we demonstrated the ability to couple amorphous selenium to a pixelated CMOS readout sensor. We leveraged the properties of the *Topmetal-II-* with exposed electrodes and deposited 500 μm of amorphous selenium on the pixel array. We built a system to control and readout the sensors and trigger on the detector output in response to ionization events. We showed the ability to measure individual β and γ interactions from a ^{90}Sr and ^{57}Co source with a pixel noise of $\sim$ 22 e^-. Unfortunately, the limited charge collection of the *Topmetal-II-* pixel limited our ability to make spectroscopic measurements. Future work on improving the pixel charge collection, readout, and scalability is underway, but this was still a critical first demonstration in the path of creating a ton scale enriched ^{82}Se detector.

Appendix A

SNOLAB UPGRADE AMPLIFIER CALIBRATION CONSTANTS

We compute the calibration constant, k (ADU / e-), for each image individually. The mean value and standard deviation (computed by a Gaussian fit to the distribution of values) of k values for each science run and amplifier are shown in Table A.1. The uncertainty listed in the table is one tool used to identify bad images in the science data.

Run	Calibration k (ADU / e^-)			
	1U	1L	2U	2L
Run0	755.2 ± 1.1	718.3 ± 1.1	726.9 ± 0.9	731.4 ± 1.5
Run1	755.1 ± 1.1	718.6 ± 1.2	727.3 ± 0.9	732.2 ± 1.7
Run2	757.6 ± 2.1	723.4 ± 1.5	732.6 ± 1.5	736.3 ± 2.1
Run3	757.0 ± 2.3	723.6 ± 1.6	730.6 ± 1.0	735.7 ± 1.5
Run4	758.7 ± 1.6	724.0 ± 1.6	732.5 ± 1.4	736.5 ± 1.8
Run5	757.1 ± 1.5	724.3 ± 1.3	732.9 ± 1.2	737.0 ± 1.8
Run6	757.8 ± 1.7	723.9 ± 1.6	732.5 ± 1.1	736.3 ± 1.9

Table A.1: Science run calibration constants.

Appendix B

SNOLAB UPGRADE LOW ENERGY CLUSTER GALLERY

Below are the 11 clusters identified as "bulk" events below 200 eV_{ee} in the skipper CCD dataset. Each plot is a snapshot of a single cluster. The upper left plot shows the image region, centered on the clusters, with ± 200 pixels in the x-direction and ± 20 pixels in the y-direction. The lower left is the mask for the same region, where red is a masked region of the CCD and blue is clear. Finally the right inset is the fit window with x and y projections of the charge and the Gaussian parameters from the likelihood clustering.

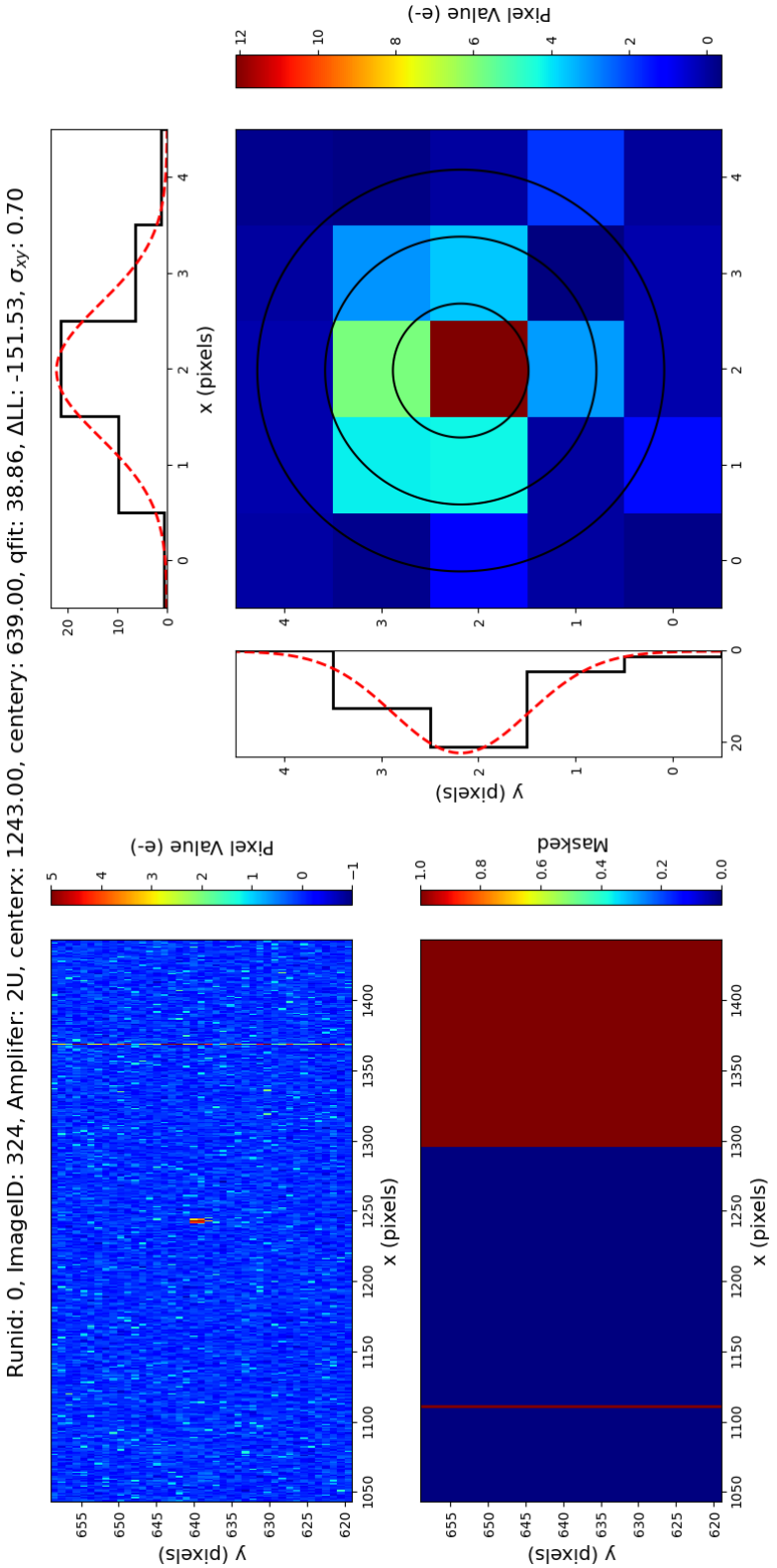
Runid: 0, ImageID: 324, Amplifer: 2U, centerx: 1243.00, centery: 639.00, qfit: 38.86, ΔLL: -151.53, σ_{xy}: 0.70
y (pixels)
x (pixels)
Pixel Value (e-)
Masked
y (pixels)
x (pixels)
Pixel Value (e-)

Figure B.1

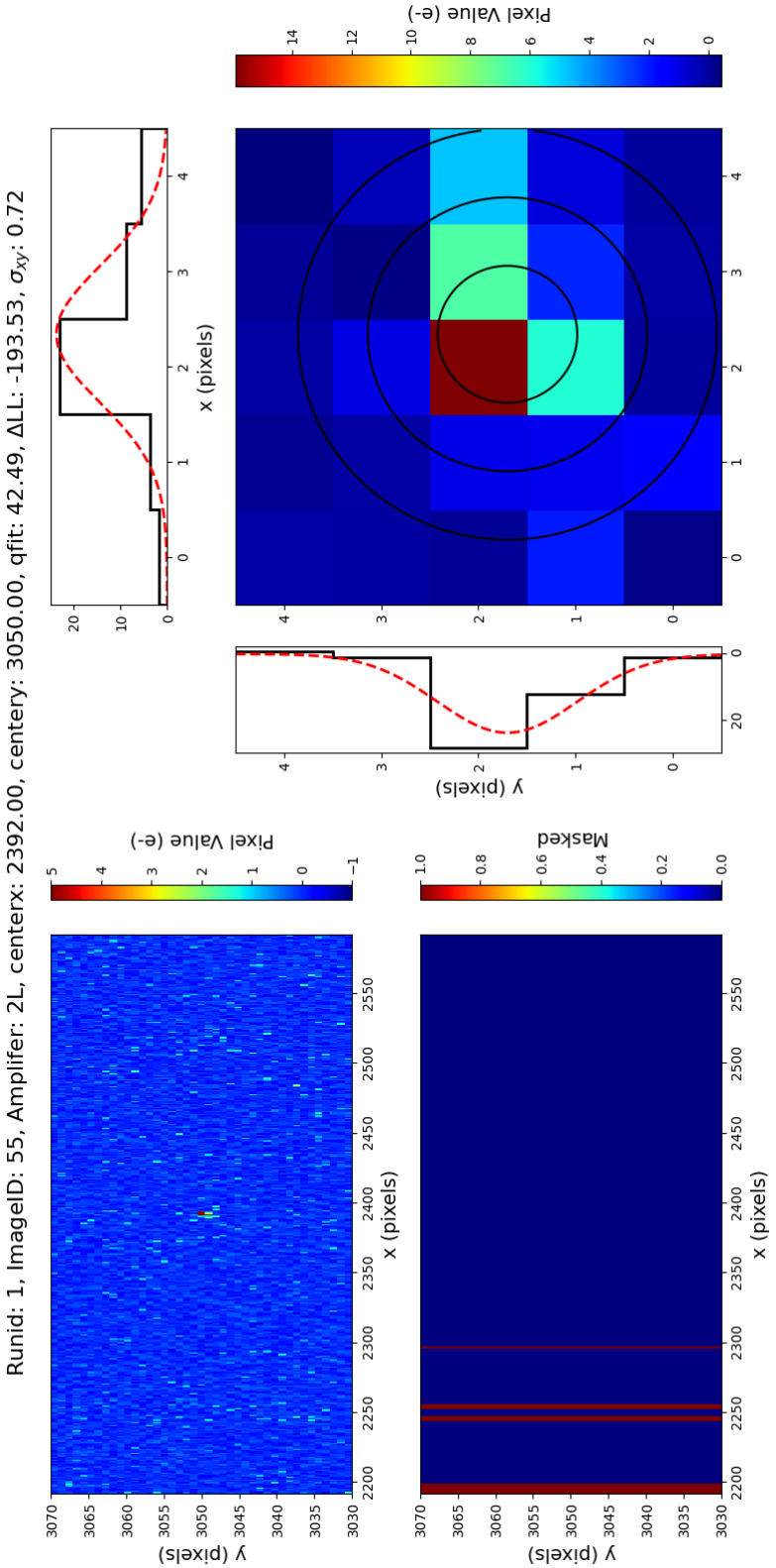
Runid: 1, ImageID: 55, Amplifer: 2L, centerx: 2392.00, centery: 3050.00, qfit: 42.49, ΔLL: -193.53, σ_{xy}: 0.72
Pixel Value (e-)
Masked
y (pixels)
x (pixels)

Figure B.2

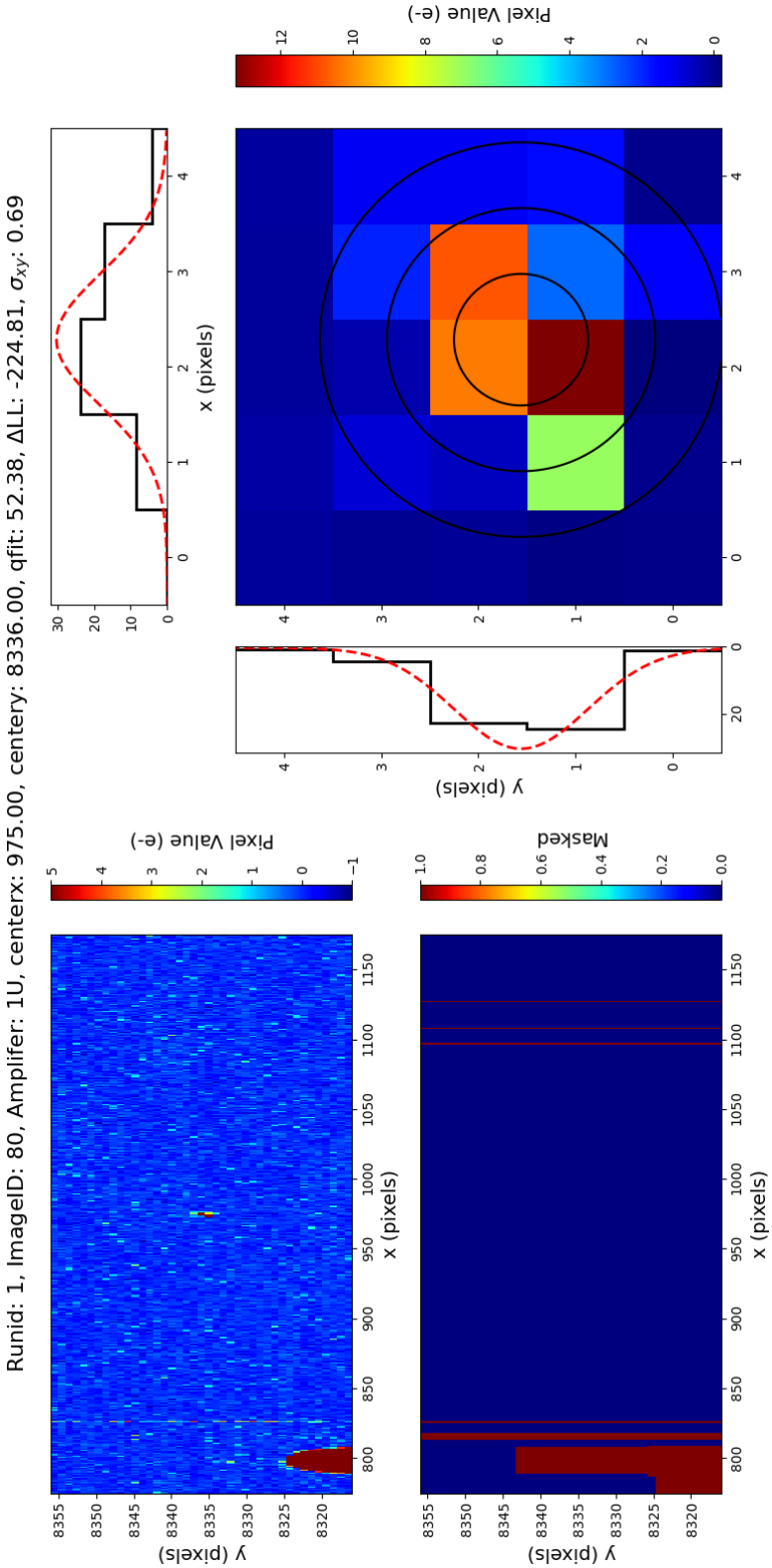
Runid: 1, ImageID: 80, Amplifier: 1U, centerx: 975.00, centery: 8336.00, qfit: 52.38, ΔLL: -224.81, σ_{xy}: 0.69
y (pixels)
x (pixels)
Pixel Value (e-)
Masked
Pixel Value (e-)
y (pixels)
x (pixels)

Figure B.3

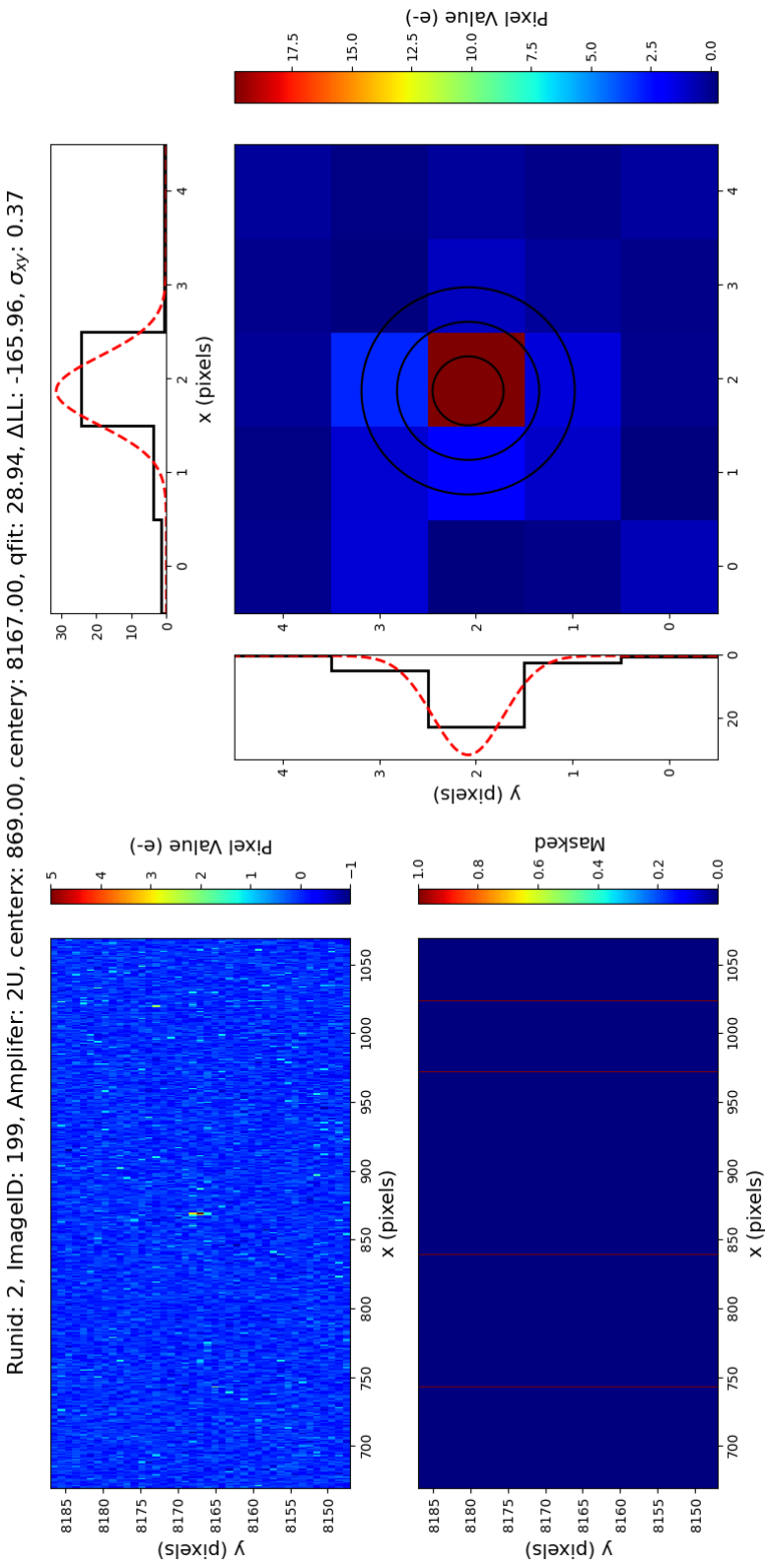
Runid: 2, ImageID: 199, Amplifer: 2U, centerx: 869.00, centery: 8167.00, qfit: 28.94, ΔLL: -165.96, σ_{xy}: 0.37
y (pixels)
x (pixels)
Pixel Value (e-)
Masked

Figure B.4

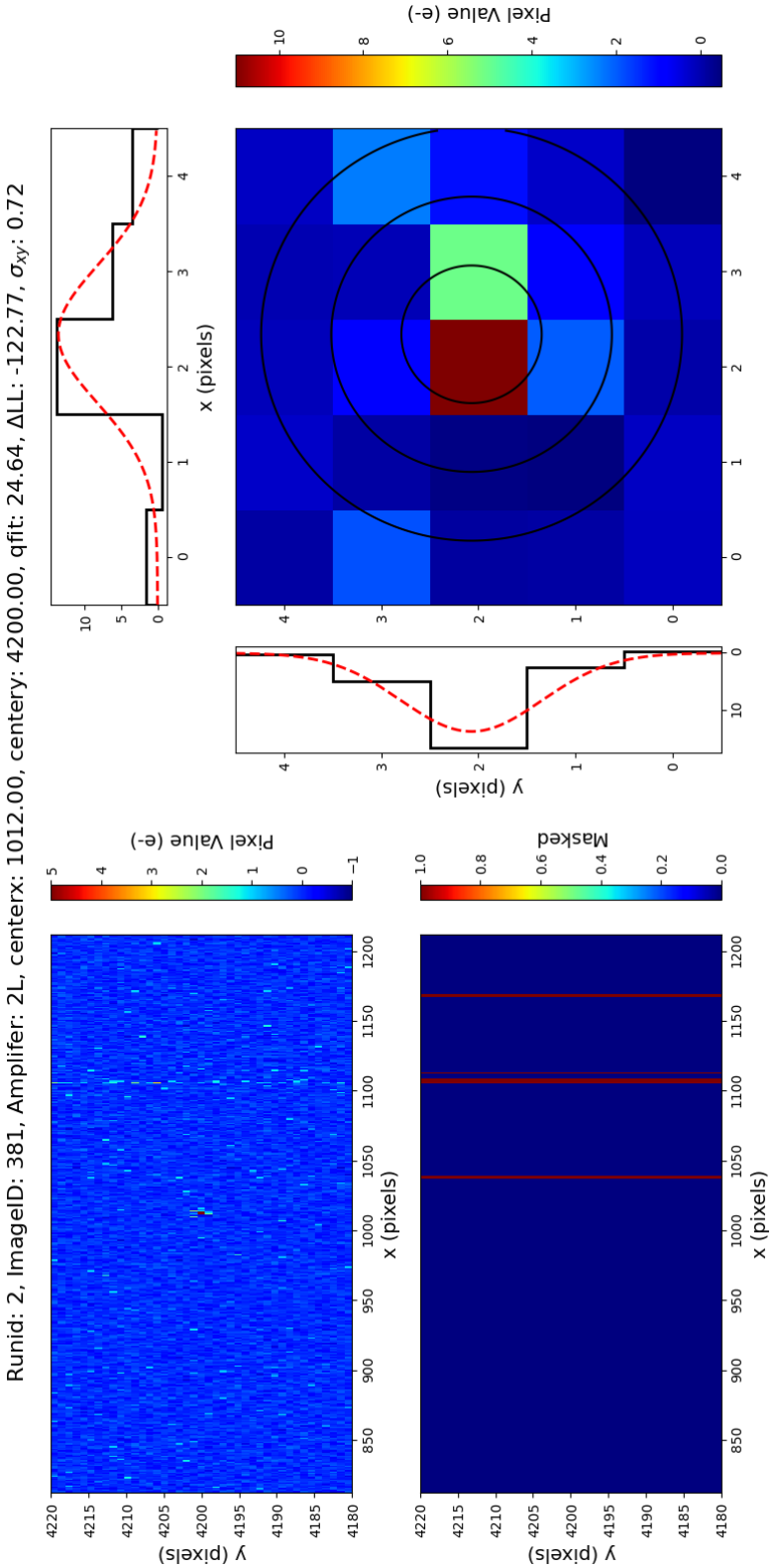
Runid: 2, ImageID: 381, Amplifer: 2L, centerx: 1012.00, centery: 4200.00, qfit: 24.64, ΔLL: -122.77, σ_{xy}: 0.72
y (pixels)
x (pixels)
Pixel Value (e-)
Masked
y (pixels)
x (pixels)
Pixel Value (e-)

Figure B.5

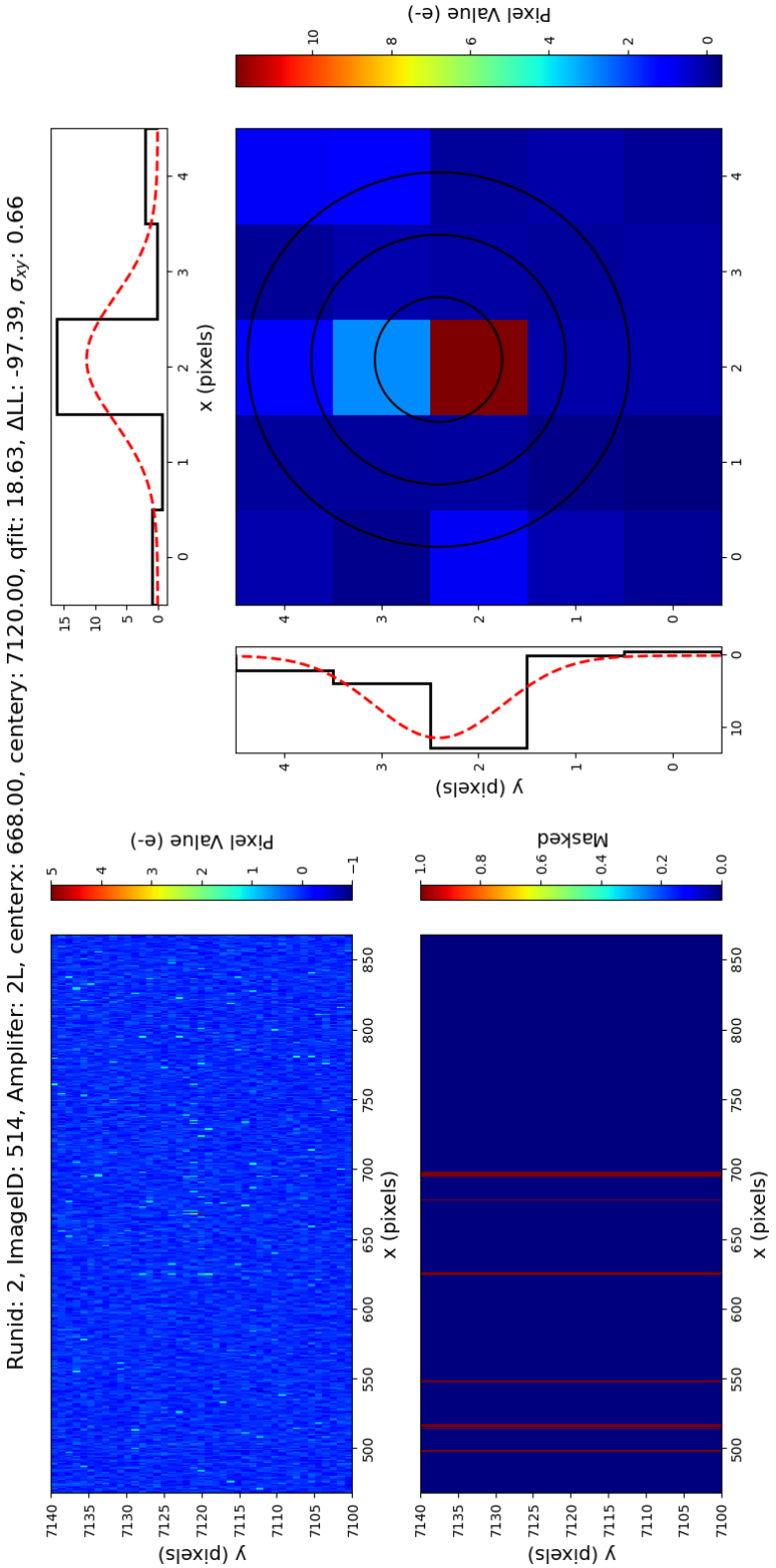
Runid: 2, ImageID: 514, Amplifer: 2L, centerx: 668.00, centery: 7120.00, qfit: 18.63, ΔLL: -97.39, σ_{xy}: 0.66
y (pixels)
x (pixels)
Pixel Value (e-)
Masked
Pixel Value (e-)
y (pixels)
x (pixels)

Figure B.6

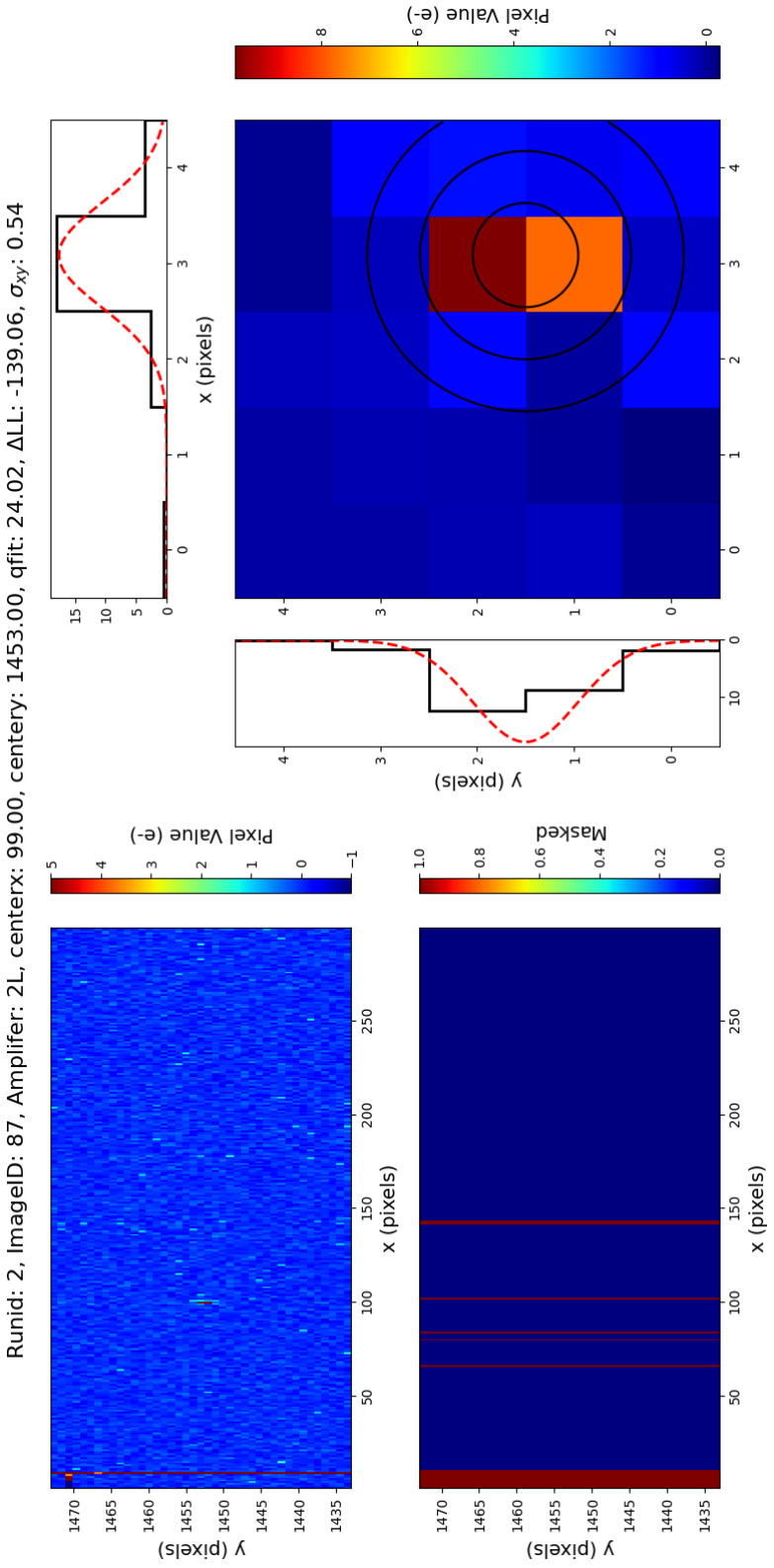
Runid: 2, ImageID: 87, Amplifer: 2L, centerx: 99.00, centery: 1453.00, qfit: 24.02, ΔLL: -139.06, σ_{xy}: 0.54
y (pixels)
x (pixels)
Pixel Value (e-)
Masked
y (pixels)
x (pixels)
Pixel Value (e-)

Figure B.7

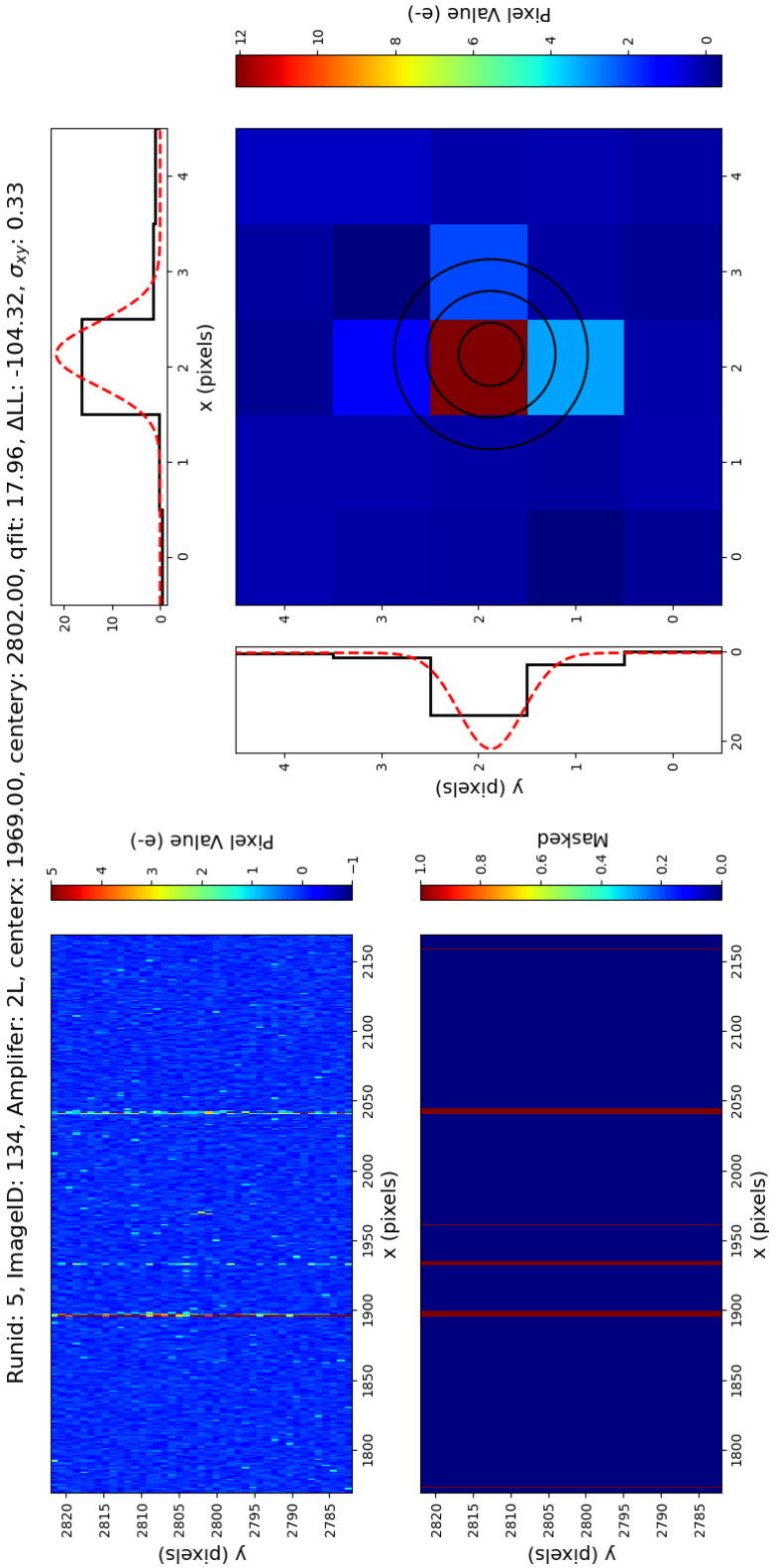
Runid: 5, ImageID: 134, Amplifer: 2L, centerx: 1969.00, centery: 2802.00, qfit: 17.96, ΔLL: -104.32, σ_{xy}: 0.33
Pixel Value (e-)
Masked
y (pixels)
x (pixels)

Figure B.8

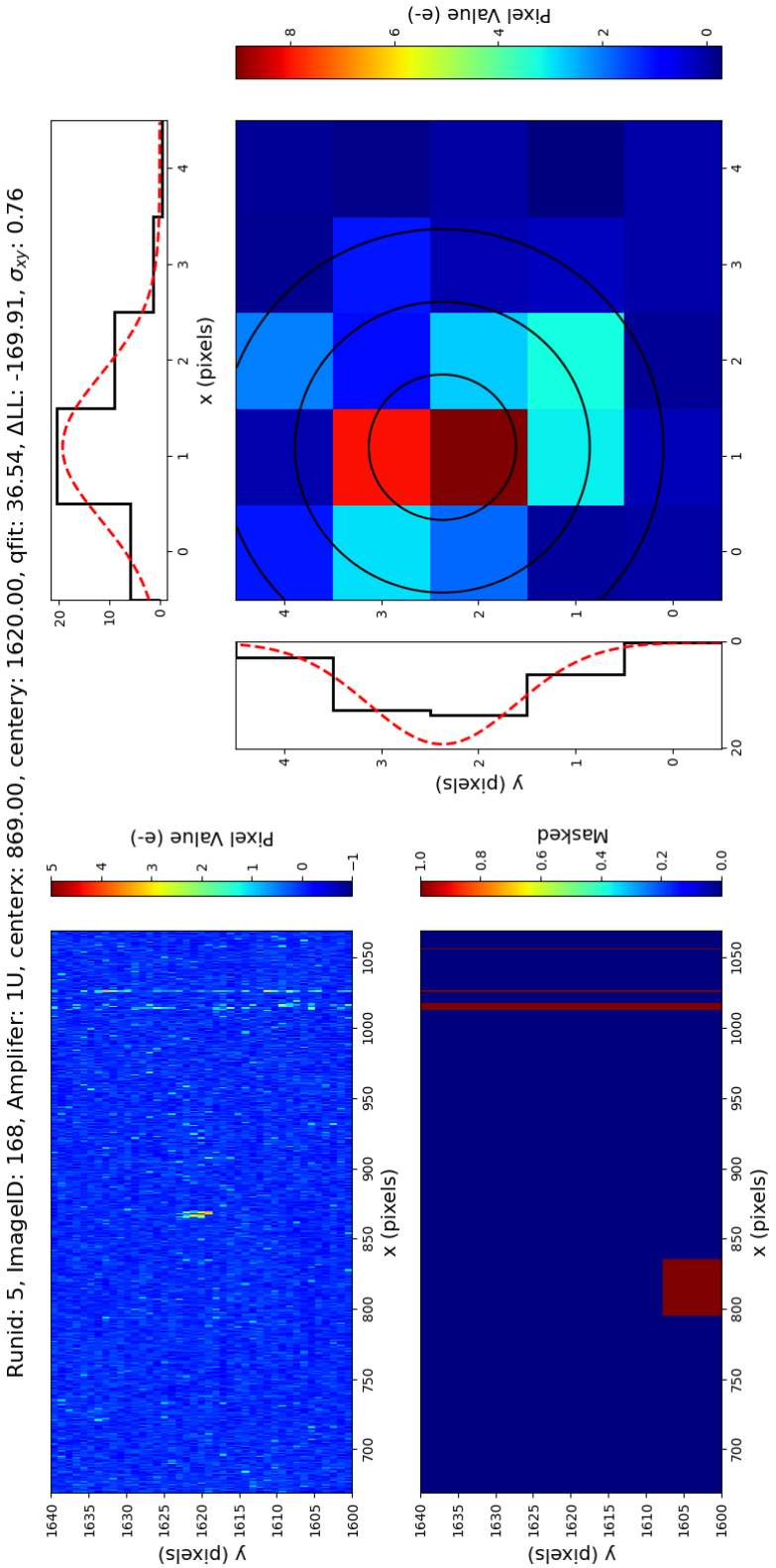
Runid: 5, ImageID: 168, Amplifer: 1U, centerx: 869.00, centery: 1620.00, qfit: 36.54, ΔLL: -169.91, σ_{xy}: 0.76
Pixel Value (e-)
Masked
y (pixels)
x (pixels)

Figure B.9

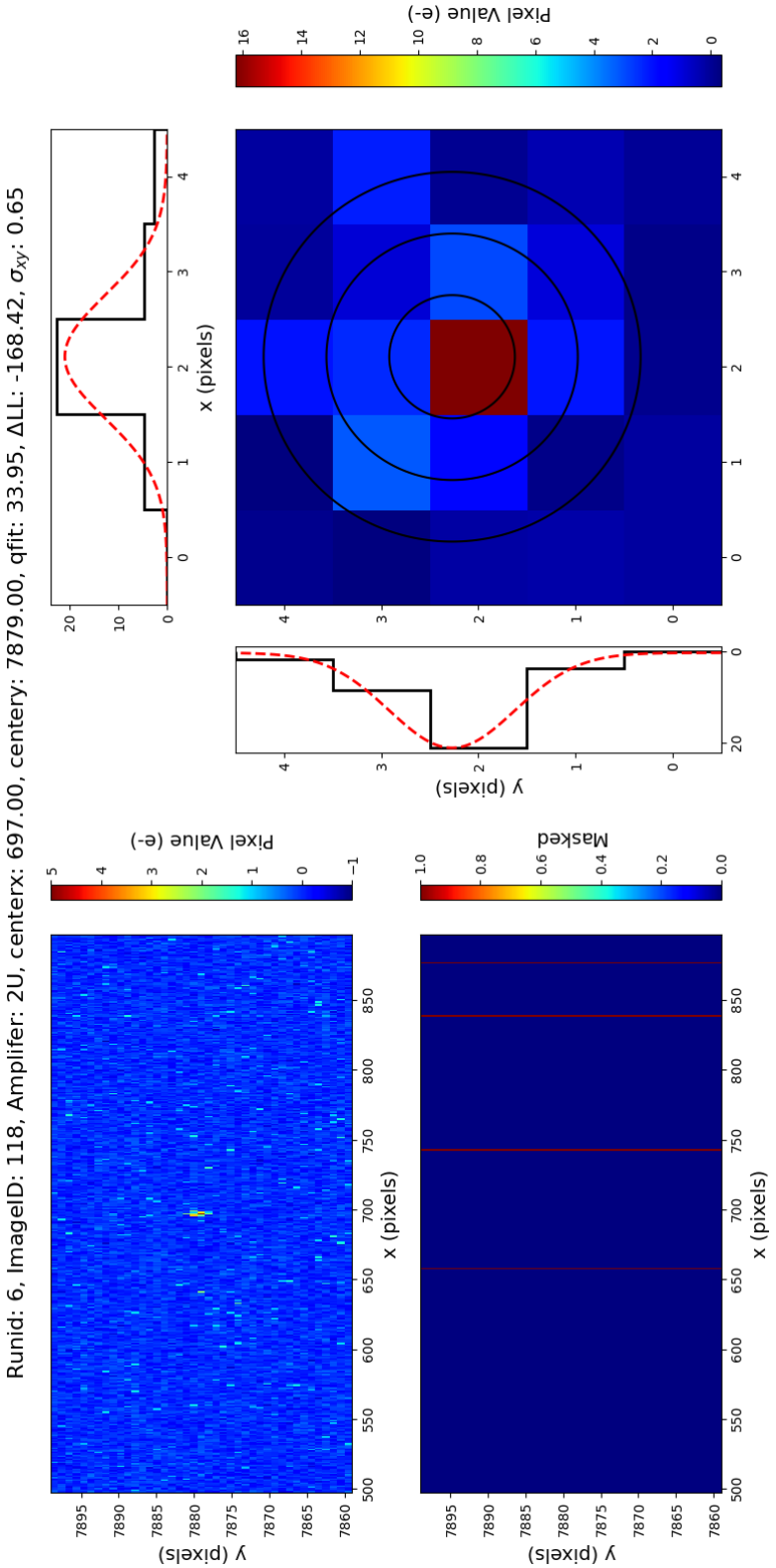
Runid: 6, ImageID: 118, Amplifer: 2U, centerx: 697.00, centery: 7879.00, qfit: 33.95, ΔLL: -168.42, σ_{xy}: 0.65
y (pixels)
x (pixels)
Pixel Value (e-)
Masked
Pixel Value (e-)
y (pixels)
x (pixels)

Figure B.10

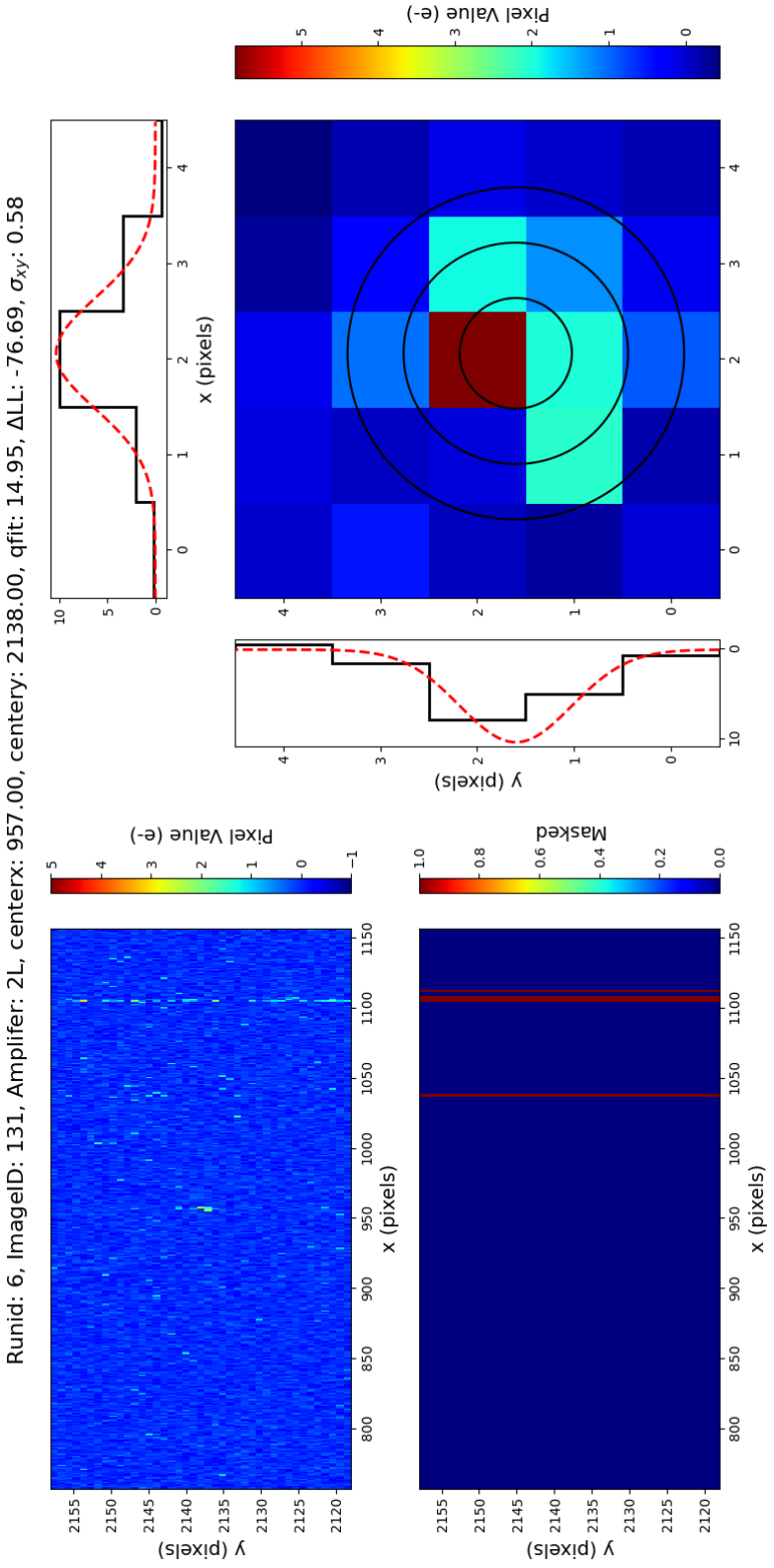
Runid: 6, ImageID: 131, Amplifer: 2L, centerx: 957.00, centery: 2138.00, qfit: 14.95, ΔLL: -76.69, σ_{xy}: 0.58
Pixel Value (e-)
Masked
x (pixels)
y (pixels)

Figure B.11

BIBLIOGRAPHY

[1] Mary K Gaillard, Paul D Grannis, and Frank J Sciulli. The standard model of particle physics. *Reviews of Modern Physics*, 71(2):S96, 1999.

[2] Tomio Kobayashi. Experimental verification of the standard model of particle physics. *Proceedings of the Japan Academy, Series B*, 97(5):211–235, 2021.

[3] J-E Augustin, Adam M Boyarski, Martin Breidenbach, F Bulos, JT Dakin, GJ Feldman, GE Fischer, D Fryberger, G Hanson, B Jean-Marie, et al. Discovery of a narrow resonance in e+ e- annihilation. *Physical Review Letters*, 33(23):1406, 1974.

[4] Shahriar Abachi, B Abbott, M Abolins, Bannanje Sripath Acharya, I Adam, DL Adams, M Adams, S Ahn, H Aihara, J Alitti, et al. Observation of the top quark. *Physical review letters*, 74(14):2632, 1995.

[5] Fumio Abe, H Akimoto, A Akopian, MG Albrow, SR Amendolia, D Amidei, J Antos, C Anway-Wiese, S Aota, G Apollinari, et al. Observation of top quark production in p p collisions with the collider detector at fermilab. *Physical review letters*, 74(14):2626, 1995.

[6] SW Herb, DC Hom, LM Lederman, JC Sens, HD Snyder, JK Yoh, JA Appel, BC Brown, CN Brown, WR Innes, et al. Observation of a dimuon resonance at 9.5 gev in 400-gev proton-nucleus collisions. *Physical Review Letters*, 39(5):252, 1977.

[7] Ch Berger, H Genzel, R Grigull, W Lackas, F Raupach, A Klovning, E Lillestöl, E Lillethun, JA Skard, H Ackermann, et al. Evidence for gluon bremsstrahlung in e+ e- annihilations at high energies. *Physics Letters B*, 86(3-4):418–425, 1979.

[8] DP Barber, U Becker, H Benda, A Boehm, JG Branson, J Bron, D Buikman, J Burger, CC Chang, HS Chen, et al. Discovery of three-jet events and a test of quantum chromodynamics at petra. *Physical Review Letters*, 43(12):830, 1979.

[9] Po Bagnaia, M Banner, R Battiston, Ph Bloch, F Bonaudi, K Borer, M Borghini, J-C Chollet, AG Clark, C Conta, et al. Evidence for z0→ e+ e- at the cern pp collider. *Physics Letters B*, 129(1-2):130–140, 1983.

[10] G Arnison, A Astbury, B Aubert, C Bacci, G Bauer, A Bezaguet, R Böck, TJV Bowcock, M Calvetti, P Catz, et al. Experimental observation of lepton pairs of invariant mass around 95 gev/c2 at the cern sps collider. *Physics Letters B*, 126(5):398–410, 1983.

[11] Serguei Chatrchyan, Vardan Khachatryan, Albert M Sirunyan, Armen Tumasyan, Wolfgang Adam, Ernest Aguilo, Thomas Bergauer, M Dragicevic, J Erö, C Fabjan, et al. Observation of a new boson at a mass of 125 gev with the cms experiment at the lhc. *Physics Letters B*, 716(1):30–61, 2012.

[12] Francesco Vissani. Do experiments suggest a hierarchy problem? *Physical Review D*, 57(11):7027, 1998.

[13] Sacha Davidson, Enrico Nardi, and Yosef Nir. Leptogenesis. *Physics Reports*, 466(4-5):105–177, 2008.

[14] James M Cline. Baryogenesis. *arXiv preprint hep-ph/0609145*, 2006.

[15] Horace W Babcock. The rotation of the andromeda nebula. *Lick observatory bulletin*, 19:41–51, 1939.

[16] Vera C Rubin, W Kent Ford Jr, and Norbert Thonnard. Rotational properties of 21 sc galaxies with a large range of luminosities and radii, from ngc 4605/r= 4kpc/to ugc 2885/r= 122 kpc. *The Astrophysical Journal*, 238:471–487, 1980.

[17] Douglas Clowe, Maruša Bradač, Anthony H Gonzalez, Maxim Markevitch, Scott W Randall, Christine Jones, and Dennis Zaritsky. A direct empirical proof of the existence of dark matter. *The Astrophysical Journal*, 648(2):L109, 2006.

[18] Charles L Bennett, Davin Larson, Janet L Weiland, N Jarosik, G Hinshaw, N Odegard, KM Smith, RS Hill, B Gold, M Halpern, et al. Nine-year wilkinson microwave anisotropy probe (wmap) observations: final maps and results. *The Astrophysical Journal Supplement Series*, 208(2):20, 2013.

[19] Nabila Aghanim, Yashar Akrami, Mark Ashdown, J Aumont, C Baccigalupi, M Ballardini, AJ Banday, RB Barreiro, N Bartolo, S Basak, et al. Planck 2018 results-vi. cosmological parameters. *Astronomy & Astrophysics*, 641:A6, 2020.

[20] C Bartram, T Braine, E Burns, R Cervantes, N Crisosto, N Du, H Korandla, G Leum, P Mohapatra, T Nitta, et al. Search for invisible axion dark matter in the 3.3–4.2 μ ev mass range. *Physical review letters*, 127(26):261803, 2021.

[21] R Cervantes, G Carosi, C Hanretty, S Kimes, BH LaRoque, G Leum, P Mohapatra, NS Oblath, R Ottens, Y Park, et al. Admx-orpheus first search for 70 μev dark photon dark matter: Detailed design, operations, and analysis. *arXiv preprint arXiv:2204.09475*, 2022.

[22] Chiara P Salemi, Joshua W Foster, Jonathan L Ouellet, Andrew Gavin, Kaliroë MW Pappas, Sabrina Cheng, Kate A Richardson, Reyco Henning, Yonatan Kahn, Rachel Nguyen, et al. Search for low-mass axion dark matter with abracadabra-10 cm. *Physical review letters*, 127(8):081801, 2021.

[23] Anne M Green and Bradley J Kavanagh. Primordial black holes as a dark matter candidate. *Journal of Physics G: Nuclear and Particle Physics*, 48(4):043001, 2021.

[24] Mordehai Milgrom. A modification of the newtonian dynamics as a possible alternative to the hidden mass hypothesis. *The Astrophysical Journal*, 270:365–370, 1983.

[25] Jacob D Bekenstein. Relativistic gravitation theory for the modified newtonian dynamics paradigm. *Physical Review D*, 70(8):083509, 2004.

[26] Scott Dodelson. The real problem with mond. *International Journal of Modern Physics D*, 20(14):2749–2753, 2011.

[27] P Cushman, C Galbiati, DN McKinsey, H Robertson, TMP Tait, D Bauer, A Borgland, B Cabrera, F Calaprice, J Cooley, et al. Snowmass cf1 summary: Wimp dark matter direct detection. *arXiv preprint arXiv:1310.8327*, 2013.

[28] Marco Battaglieri, Alberto Belloni, Aaron Chou, Priscilla Cushman, Bertrand Echenard, Rouven Essig, Juan Estrada, Jonathan L Feng, Brenna Flaugher, Patrick J Fox, et al. Us cosmic visions: new ideas in dark matter 2017: community report. *arXiv preprint arXiv:1707.04591*, 2017.

[29] Rouven Essig, Graham K Giovanetti, Noah Kurinsky, Dan McKinsey, Karthik Ramanathan, Kelly Stifter, and Tien-Tien Yu. Snowmass2021 cosmic frontier: The landscape of low-threshold dark matter direct detection in the next decade. *arXiv preprint arXiv:2203.08297*, 2022.

[30] D Baxter, IM Bloch, E Bodnia, X Chen, Jan Conrad, P Di Gangi, JEY Dobson, D Durnford, SJ Haselschwardt, A Kaboth, et al. Recommended conventions for reporting results from direct dark matter searches. *The European Physical Journal C*, 81(10):1–19, 2021.

[31] JD Lewin and PF Smith. Review of mathematics, numerical factors, and corrections for dark matter experiments based on elastic nuclear recoil. *Astroparticle Physics*, 6(1):87–112, 1996.

[32] David G Cerdeno and Anne M Green. Direct detection of wimps. *arXiv preprint arXiv:1002.1912*, 2010.

[33] Rouven Essig, Marivi Fernandez-Serra, Jeremy Mardon, Adrian Soto, Tomer Volansky, and Tien-Tien Yu. Direct detection of sub-gev dark matter with semiconductor targets. *Journal of High Energy Physics*, 2016(5):1–54, 2016.

[34] Sinéad M. Griffin, Katherine Inzani, Tanner Trickle, Zhengkang Zhang, and Kathryn M. Zurek. Extended Calculation of Dark Matter-Electron Scattering in Crystal Targets. 5 2021.

[35] A Aguilar-Arevalo, D Amidei, X Bertou, M Butner, G Cancelo, A Castañeda Vázquez, BA Cervantes Vergara, AE Chavarria, CR Chavez, JRT de Mello Neto, et al. Search for low-mass wimps in a 0.6 kg day exposure of the damic experiment at snolab. *Physical Review D*, 94(8):082006, 2016.

[36] An experiment to search for dark-matter interactions using sodium iodide detectors. *Nature*, 564(7734):83–86, 2018.

[37] P-A Amaudruz, M Baldwin, M Batygov, B Beltran, CE Bina, D Bishop, J Bonatt, G Boorman, Mark Guy Boulay, B Broerman, et al. Design and construction of the deap-3600 dark matter detector. *Astroparticle Physics*, 108:1–23, 2019.

[38] E Aprile, Jelle Aalbers, F Agostini, M Alfonsi, L Althueser, FD Amaro, Vasile C Antochi, E Angelino, JR Angevaare, F Arneodo, et al. Projected wimp sensitivity of the xenonnt dark matter experiment. *Journal of Cosmology and Astroparticle Physics*, 2020(11):031, 2020.

[39] DS Akerib, X Bai, S Bedikian, E Bernard, A Bernstein, A Bolozdynya, A Bradley, D Byram, SB Cahn, C Camp, et al. The large underground xenon (lux) experiment. *Nuclear Instruments and Methods in Physics Research Section A: Accelerators, Spectrometers, Detectors and Associated Equipment*, 704:111–126, 2013.

[40] Pl Agnes, T Alexander, A Alton, K Arisaka, HO Back, B Baldin, K Biery, G Bonfini,

M Bossa, A Brigatti, et al. First results from the darkside-50 dark matter experiment at laboratori nazionali del gran sasso. *Physics Letters B*, 743:456–466, 2015.

[41] E Armengaud, Q Arnaud, C Augier, A Benoît, L Bergé, T Bergmann, J Billard, T De Boissière, G Bres, A Broniatowski, et al. Performance of the edelweiss-iii experiment for direct dark matter searches. *Journal of Instrumentation*, 12(08):P08010, 2017.

[42] R Agnese, AJ Anderson, T Aramaki, I Arnquist, W Baker, D Barker, R Basu Thakur, DA Bauer, A Borgland, MA Bowles, et al. Projected sensitivity of the supercdms snolab experiment. *Physical Review D*, 95(8):082002, 2017.

[43] AH Abdelhameed, G Angloher, P Bauer, A Bento, E Bertoldo, C Bucci, L Canonica, Antonio D'Addabbo, X Defay, S Di Lorenzo, et al. First results from the cresst-iii low-mass dark matter program. *Physical Review D*, 100(10):102002, 2019.

[44] Antonio Ereditato. State of the art of neutrino physics, the: A tutorial for graduate students and young researchers. 2018.

[45] S Bilenky. Neutrino oscillations: from an historical perspective to the present status. In *Journal of Physics: Conference Series*, volume 718, page 062005. IOP Publishing, 2016.

[46] Carlo Giunti and Chung W Kim. *Fundamentals of neutrino physics and astrophysics*. Oxford university press, 2007.

[47] Stefano Dell'Oro, Simone Marcocci, Matteo Viel, and Francesco Vissani. Neutrinoless double beta decay: 2015 review. *Advances in High Energy Physics*, 2016, 2016.

[48] Michelle J Dolinski, Alan WP Poon, and Werner Rodejohann. Neutrinoless double-beta decay: status and prospects. *arXiv preprint arXiv:1902.04097*, 2019.

[49] M Aker, Armen Beglarian, J Behrens, A Berlev, U Besserer, B Bieringer, F Block, S Bobien, M Boettcher, B Bornschein, et al. Direct neutrino-mass measurement with sub-electronvolt sensitivity. *Nature Physics*, 18(2), 2022.

[50] A Nucciotti, B Alpert, M Balata, D Becker, D Bennett, A Bevilacqua, M Biasotti, V Ceriale, G Ceruti, D Corsini, et al. Status of the holmes experiment to directly measure the neutrino mass. *Journal of Low Temperature Physics*, 193(5):1137–1145, 2018.

[51] A Ashtari Esfahani, S Böser, N Buzinsky, MC Carmona-Benitez, C Claessens, L de Viveiros, PJ Doe, S Enomoto, M Fertl, JA Formaggio, et al. The project 8 neutrino mass experiment. *arXiv preprint arXiv:2203.07349*, 2022.

[52] J Barea, J Kotila, and F Iachello. Nuclear matrix elements for double-β decay. *Physical Review C*, 87(1):014315, 2013.

[53] Claudio Giganti, Stéphane Lavignac, and Marco Zito. Neutrino oscillations: the rise of the pmns paradigm. *Progress in Particle and Nuclear Physics*, 98:1–54, 2018.

[54] Stefano Dell'Oro, Simone Marcocci, and Francesco Vissani. New expectations and uncertainties on neutrinoless double beta decay. *Physical Review D*, 90(3):033005, 2014.

[55] Matteo Agostini, GR Araujo, AM Bakalyarov, M Balata, I Barabanov, L Baudis, C Bauer, E Bellotti, S Belogurov, A Bettini, et al. Final results of gerda on the search for neutrinoless double-β decay. *Physical review letters*, 125(25):252502, 2020.

[56] Fabio Bellini, Oscar Azzolini, Maria Teresa Barrera, Jeffrey Beeman, Mattia Beretta, Matteo Biassoni, Chiara Brofferio, Carlo Bucci, Lucia Canonica, Silvia Capelli, Laura Cardani, Paolo Carniti, Nicola Casali, Lorenzo Cassina, Massimiliano Clemenza, Oliverio Cremonesi, Angelo Cruciani, Antonio D'Addabbo, Ioan Dafinei, Sergio Di Domizio,

Fernando Ferroni, Luca Gironi, Andrea Giuliani, Paolo Gorla, Claudio Gotti, Giorgio Keppel, Maria Martinez, Silvio Morganti, Sergei Nagorny, Massimiliano Nastasi, Stefano Nisi, Claudia Nones, Donato Orlandi, Lorenzo Pagnanini, Marco Pallavicini, Vincenzo Palmieri, Luca Pattavina, Maura Pavan, Gianluigi Pessina, Valerio Pettinacci, Stefano Pirro, Stefano Pozzi, Ezio Previtali, Andrei Puiu, Claudia Rusconi, Karoline Schäffner, Claudia Tomei, Marco Vignati, and Anastasia Zolotarova. Result on the neutrinoless double beta decay search of 82 Se with the CUPID-0 experiment. *Universe*, 5(1):111801, 2019.

[57] E Armengaud, C Augier, AS Barabash, F Bellini, G Benato, Alain Benoit, M Beretta, L Bergé, J Billard, Yu A Borovlev, et al. New limit for neutrinoless double-beta decay of mo 100 from the cupid-mo experiment. *Physical review letters*, 126(18):181802, 2021.

[58] Search for majorana neutrinos exploiting millikelvin cryogenics with cuore. *Nature*, 604(7904):53–58, 2022.

[59] Zen Collaboration et al. First search for the majorana nature of neutrinos in the inverted mass ordering region with kamland-zen. *arXiv preprint arXiv:2203.02139*, 2022.

[60] S Fukuda, Y Fukuda, M Ishitsuka, Y Itow, T Kajita, J Kameda, K Kaneyuki, K Kobayashi, Y Koshio, M Miura, et al. Constraints on neutrino oscillations using 1258 days of super-kamiokande solar neutrino data. *Physical Review Letters*, 86(25):5656, 2001.

[61] Q Retal Ahmad, RC Allen, TC Andersen, JD Anglin, JC Barton, EW Beier, M Bercovitch, J Bigu, SD Biller, RA Black, et al. Direct evidence for neutrino flavor transformation from neutral-current interactions in the sudbury neutrino observatory. *Physical review letters*, 89(1):011301, 2002.

[62] T Araki, K Eguchi, S Enomoto, K Furuno, K Ichimura, H Ikeda, K Inoue, K Ishihara,

T Iwamoto, T Kawashima, et al. Measurement of neutrino oscillation with kamland: Evidence of spectral distortion. *Physical Review Letters*, 94(8):081801, 2005.

[63] Kou Abe, J Adam, H Aihara, T Akiri, Constantinos Andreopoulos, S Aoki, A Ariga, S Assylbekov, D Autiero, M Barbi, et al. Measurements of neutrino oscillation in appearance and disappearance channels by the t2k experiment with $6.6\times 1\ 0\ 20$ protons on target. *Physical Review D*, 91(7):072010, 2015.

[64] FP An, AB Balantekin, HRe Band, M Bishai, S Blyth, I Butorov, GF Cao, J Cao, WR Cen, YL Chan, et al. New measurement of antineutrino oscillation with the full detector configuration at daya bay. *Physical review letters*, 115(11):111802, 2015.

[65] Basudeb Dasgupta and Joachim Kopp. Sterile neutrinos. *Physics Reports*, 928:1–63, 2021.

[66] A Diaz, CA Argüelles, GH Collin, JM Conrad, and MH Shaevitz. Where are we with light sterile neutrinos? *Physics Reports*, 884:1–59, 2020.

[67] Alexey Boyarsky, M Drewes, T Lasserre, S Mertens, and O Ruchayskiy. Sterile neutrino dark matter. *Progress in Particle and Nuclear Physics*, 104:1–45, 2019.

[68] A Aguilar-Arevalo, D Amidei, I Arnquist, D Baxter, G Cancelo, BA Cervantes Vergara, AE Chavarria, N Corso, E Darragh-Ford, ML Di Vacri, et al. Characterization of the background spectrum in damic at snolab. *Physical Review D*, 105(6):062003, 2022.

[69] A Aguilar-Arevalo, D Amidei, Daniel Baxter, G Cancelo, BA Cervantes Vergara, AE Chavarria, JC D'Olivo, Juan Estrada, F Favela-Perez, Romain Gaior, et al. Results on low-mass weakly interacting massive particles from an 11 kg d target exposure of damic at snolab. *Physical Review Letters*, 125(24):241803, 2020.

[70] S. Agostinelli, J. Allison, K. Amako, J. Apostolakis, H. Araujo, P. Arce, M. Asai, D. Axen, S. Banerjee, G. Barrand, F. Behner, L. Bellagamba, J. Boudreau, L. Broglia,

A. Brunengo, H. Burkhardt, S. Chauvie, J. Chuma, R. Chytracek, G. Cooperman, G. Cosmo, P. Degtyarenko, A. Dell'Acqua, G. Depaola, D. Dietrich, R. Enami, A. Feliciello, C. Ferguson, H. Fesefeldt, G. Folger, F. Foppiano, A. Forti, S. Garelli, S. Giani, R. Giannitrapani, D. Gibin, J.J. Gómez Cadenas, I. González, G. Gracia Abril, G. Greeniaus, W. Greiner, V. Grichine, A. Grossheim, S. Guatelli, P. Gumplinger, R. Hamatsu, K. Hashimoto, H. Hasui, A. Heikkinen, A. Howard, V. Ivanchenko, A. Johnson, F.W. Jones, J. Kallenbach, N. Kanaya, M. Kawabata, Y. Kawabata, M. Kawaguti, S. Kelner, P. Kent, A. Kimura, T. Kodama, R. Kokoulin, M. Kossov, H. Kurashige, E. Lamanna, T. Lampén, V. Lara, V. Lefebure, F. Lei, M. Liendl, W. Lockman, F. Longo, S. Magni, M. Maire, E. Medernach, K. Minamimoto, P. Mora de Freitas, Y. Morita, K. Murakami, M. Nagamatu, R. Nartallo, P. Nieminen, T. Nishimura, K. Ohtsubo, M. Okamura, S. O'Neale, Y. Oohata, K. Paech, J. Perl, A. Pfeiffer, M.G. Pia, F. Ranjard, A. Rybin, S. Sadilov, E. Di Salvo, G. Santin, T. Sasaki, N. Savvas, Y. Sawada, S. Scherer, S. Sei, V. Sirotenko, D. Smith, N. Starkov, H. Stoecker, J. Sulkimo, M. Takahata, S. Tanaka, E. Tcherniaev, E. Safai Tehrani, M. Tropeano, P. Truscott, H. Uno, L. Urban, P. Urban, M. Verderi, A. Walkden, W. Wander, H. Weber, J.P. Wellisch, T. Wenaus, D.C. Williams, D. Wright, T. Yamada, H. Yoshida, and D. Zschiesche. Geant4—a simulation toolkit. *Nuclear Instruments and Methods in Physics Research Section A: Accelerators, Spectrometers, Detectors and Associated Equipment*, 506(3):250–303, 2003.

[71] J. Allison, K. Amako, J. Apostolakis, H. Araujo, P. Arce Dubois, M. Asai, G. Barrand, R. Capra, S. Chauvie, R. Chytracek, G.A.P. Cirrone, G. Cooperman, G. Cosmo, G. Cuttone, G.G. Daquino, M. Donszelmann, M. Dressel, G. Folger, F. Foppiano, J. Generowicz, V. Grichine, S. Guatelli, P. Gumplinger, A. Heikkinen, I. Hrivnacova, A. Howard, S. Incerti, V. Ivanchenko, T. Johnson, F. Jones, T. Koi, R. Kokoulin, M. Kossov, H. Kurashige, V. Lara, S. Larsson, F. Lei, O. Link, F. Longo, M. Maire, A. Mantero, B. Mascialino, I. McLaren, P. Mendez Lorenzo, K. Minami-

moto, K. Murakami, P. Nieminen, L. Pandola, S. Parlati, L. Peralta, J. Perl, A. Pfeiffer, M.G. Pia, A. Ribon, P. Rodrigues, G. Russo, S. Sadilov, G. Santin, T. Sasaki, D. Smith, N. Starkov, S. Tanaka, E. Tcherniaev, B. Tome, A. Trindade, P. Truscott, L. Urban, M. Verderi, A. Walkden, J.P. Wellisch, D.C. Williams, D. Wright, and H. Yoshida. Geant4 developments and applications. *IEEE Transactions on Nuclear Science*, 53(1):270–278, 2006.

[72] R Saldanha, Ryan Thomas, RHM Tsang, AE Chavarria, R Bunker, Jonathan L Burnett, Steven R Elliott, Ariel Matalon, Pitam Mitra, A Piers, et al. Cosmogenic activation of silicon. *Physical Review D*, 102(10):102006, 2020.

[73] Dario Rodrigues, Kevin Andersson, Mariano Cababie, Andre Donadon, Ana Botti, Gustavo Cancelo, Juan Estrada, Guillermo Fernandez-Moroni, Ricardo Piegaia, Matias Senger, et al. Absolute measurement of the fano factor using a skipper-ccd. *Nuclear Instruments and Methods in Physics Research Section A: Accelerators, Spectrometers, Detectors and Associated Equipment*, 1010:165511, 2021.

[74] K Ramanathan, A Kavner, AE Chavarria, P Privitera, D Amidei, T-L Chou, A Matalon, R Thomas, J Estrada, J Tiffenberg, et al. Measurement of low energy ionization signals from compton scattering in a charge-coupled device dark matter detector. *Physical Review D*, 96(4):042002, 2017.

[75] F. James and M. Roos. Minuit: A System for Function Minimization and Analysis of the Parameter Errors and Correlations. *Comput. Phys. Commun.*, 10:343–367, 1975.

[76] AE Chavarria, JI Collar, JR Peña, P Privitera, AE Robinson, B Scholz, C Sengul, J Zhou, J Estrada, F Izraelevitch, et al. Measurement of the ionization produced by sub-kev silicon nuclear recoils in a ccd dark matter detector. *Physical Review D*, 94(8):082007, 2016.

[77] R Agnese, T Aramaki, IJ Arnquist, W Baker, D Balakishiyeva, S Banik, D Barker,

R Basu Thakur, DA Bauer, T Binder, et al. Results from the super cryogenic dark matter search experiment at soudan. *Physical review letters*, 120(6):061802, 2018.

[78] R Agnese, T Aralis, T Aramaki, Isaac J Arnquist, Elham Azadbakht, W Baker, Samir Banik, D Barker, DA Bauer, T Binder, et al. Search for low-mass dark matter with cdmslite using a profile likelihood fit. *Physical Review D*, 99(6):062001, 2019.

[79] P Agnes, IFM Albuquerque, T Alexander, AK Alton, GR Araujo, David M Asner, M Ave, Henning O Back, B Baldin, G Batignani, et al. Low-mass dark matter search with the darkside-50 experiment. *Physical review letters*, 121(8):081307, 2018.

[80] Elena Aprile, Jelle Aalbers, F Agostini, M Alfonsi, L Althueser, FD Amaro, Vasile C Antochi, E Angelino, F Arneodo, Derek Barge, et al. Light dark matter search with ionization signals in xenon1t. *Physical Review Letters*, 123(25):251801, 2019.

[81] Chanpreet Amole, M Ardid, IJ Arnquist, DM Asner, D Baxter, E Behnke, M Bressler, B Broerman, G Cao, CJ Chen, et al. Dark matter search results from the complete exposure of the pico-60 c 3 f 8 bubble chamber. *Physical Review D*, 100(2):022001, 2019.

[82] Christopher Dessert, Joshua W Foster, Yonatan Kahn, and Benjamin R Safdi. Systematics in the xenon1t data: the 15-kev anti-axion. *Physics of the Dark Universe*, 34:100878, 2021.

[83] Liron Barak, Itay M Bloch, Mariano Cababie, Gustavo Cancelo, Luke Chaplinsky, Fernando Chierchie, Michael Crisler, Alex Drlica-Wagner, Rouven Essig, Juan Estrada, et al. Sensei: Direct-detection results on sub-gev dark matter from a new skipper ccd. *Physical Review Letters*, 125(17):171802, 2020.

[84] N Castelló-Mor, Damic-M Collaboration, et al. Damic-m experiment: Thick, silicon ccds to search for light dark matter. *Nuclear Instruments and Methods in Physics*

Research Section A: Accelerators, Spectrometers, Detectors and Associated Equipment, 958:162933, 2020.

[85] Alexis Aguilar-Arevalo, Fabricio Alcalde Bessia, Nicolas Avalos, Daniel Baxter, Xavier Bertou, Carla Bonifazi, Ana Botti, Mariano Cababie, Gustavo Cancelo, Brenda Aurea Cervantes-Vergara, et al. The oscura experiment. *arXiv preprint arXiv:2202.10518*, 2022.

[86] I Arnquist, N Avalos, P Bailly, D Baxter, X Bertou, M Bogdan, C Bourgeois, J Brandt, A Cadiou, N Castelló-Mor, et al. The damic-m experiment: Status and first results. *arXiv preprint arXiv:2210.12070*, 2022.

[87] Susana Cebrián. Cosmogenic activation of materials. *International Journal of Modern Physics A*, 32(30):1743006, 2017.

[88] Laura Baudis, Alexander Kish, Francesco Piastra, and Marc Schumann. Cosmogenic activation of xenon and copper. *The European Physical Journal C*, 75(10):1–9, 2015.

[89] G Fernandez Moroni, F Chierchie, M Sofo Haro, L Stefanazzi, A Soto, EE Paolini, G Cancelo, K Treptow, N Wilcer, T Zmuda, et al. Low threshold acquisition controller for skipper charge coupled devices. In *2019 Argentine Conference on Electronics (CAE)*, pages 86–91. IEEE, 2019.

[90] Liron Barak, Itay M Bloch, Ana Botti, Mariano Cababie, Gustavo Cancelo, Luke Chaplinsky, Fernando Chierchie, Michael Crisler, Alex Drlica-Wagner, Rouven Essig, et al. Sensei: Characterization of single-electron events using a skipper charge-coupled device. *Physical Review Applied*, 17(1):014022, 2022.

[91] R.S. AVERBACK and T. DIAZ DE LA RUBIA. Displacement damage in irradiated metals and semiconductors. In Henry Ehrenreich and Frans Spaepen, editors, *Solid State Physics*, volume 51 of *Solid State Physics*, pages 281–402. Academic Press, 1998.

[92] Kai Nordlund, Steven J Zinkle, Andrea E Sand, Fredric Granberg, Robert S Averback, Roger E Stoller, Tomoaki Suzudo, Lorenzo Malerba, Florian Banhart, William J Weber, et al. Primary radiation damage: A review of current understanding and models. *Journal of Nuclear Materials*, 512:450–479, 2018.

[93] E Fretwurst, N Claussen, N Croitoru, G Lindström, B Papendick, U Pein, H Schatz, T Schulz, and R Wunstorf. Radiation hardness of silicon detectors for future colliders. *Nuclear Instruments and Methods in Physics Research Section A: Accelerators, Spectrometers, Detectors and Associated Equipment*, 326(1-2):357–364, 1993.

[94] D Bechevet, M Glaser, A Houdayer, C Lebel, C Leroy, M Moll, P Roy, RD48/ROSE Collaboration, et al. Results of irradiation tests on standard planar silicon detectors with 7–10mev protons. *Nuclear Instruments and Methods in Physics Research Section A: Accelerators, Spectrometers, Detectors and Associated Equipment*, 479(2-3):487–497, 2002.

[95] Karthik Ramanathan and Noah Kurinsky. Ionization yield in silicon for ev-scale electron-recoil processes. *Physical Review D*, 102(6):063026, 2020.

[96] R G H Robertson and D A Knapp. Direct measurements of neutrino mass. *Annual Review of Nuclear and Particle Science*, 38(1):185–215, 1988.

[97] A Aguilar-Arevalo, D Amidei, X Bertou, D Bole, M Butner, G Cancelo, A Castañeda Vázquez, AE Chavarria, JRT de Mello Neto, S Dixon, et al. Measurement of radioactive contamination in the high-resistivity silicon ccds of the damic experiment. *Journal of Instrumentation*, 10(08):P08014, 2015.

[98] A Aguilar-Arevalo, D Amidei, D Baxter, G Cancelo, BA Cervantes Vergara, AE Chavarria, E Darragh-Ford, JC d'Olivo, J Estrada, F Favela-Perez, et al. Measurement of the bulk radioactive contamination of detector-grade silicon with damic at snolab. *Journal of Instrumentation*, 16(06):P06019, 2021.

[99] Stephen E Holland, Donald E Groom, Nick P Palaio, Richard J Stover, and Mingzhi Wei. Fully depleted, back-illuminated charge-coupled devices fabricated on high-resistivity silicon. *IEEE Transactions on Electron Devices*, 50(1):225–238, 2003.

[100] Guillermo Fernandez Moroni, Fernando Chierchie, Javier Tiffenberg, Ana Botti, Mariano Cababie, Gustavo Cancelo, Eliana L Depaoli, Juan Estrada, Stephen E Holland, Dario Rodrigues, et al. The skipper ccd for low-energy threshold particle experiments above ground. *arXiv preprint arXiv:2107.00168*, 2021.

[101] D Norcini, N Castello-Mor, D Baxter, NJ Corso, J Cuevas-Zepeda, C De Dominicis, A Matalon, S Munagavalasa, S Paul, P Privitera, et al. Precision measurement of compton scattering in silicon with a skipper ccd for dark matter detection. *Physical Review D*, 106(9):092001, 2022.

[102] Michelangelo Traina. *Search for light dark matter and exploration of the hidden sector with the DAMIC at SNOLAB and DAMIC-M charge-coupled devices*. PhD thesis, Laboratoire de Physique Nucleaire et det Hautes Energies, 2022.

[103] I Arnquist, N Avalos, D Baxter, X Bertou, N Castello-Mor, AE Chavarria, J Cuevas-Zepeda, J Cortabitarte Gutierrez, J Duarte-Campderros, A Dastgheibi-Fard, et al. First constraints from damic-m on sub-gev dark-matter particles interacting with electrons. *arXiv preprint arXiv:2302.02372*, 2023.

[104] A Aguilar-Arevalo, D Amidei, Daniel Baxter, G Cancelo, BA Cervantes Vergara, AE Chavarria, E Darragh-Ford, JRT de Mello Neto, JC D'Olivo, Juan Estrada, et al. Constraints on light dark matter particles interacting with electrons from damic at snolab. *Physical review letters*, 123(18):181802, 2019.

[105] Elena Aprile, K Abe, F Agostini, S Ahmed Maouloud, M Alfonsi, L Althueser, E Angelino, JR Angevaare, Vasile C Antochi, D Antón Martin, et al. Emission of sin-

gle and few electrons in xenon1t and limits on light dark matter. *arXiv preprint arXiv:2112.12116*, 2021.

[106] Chen Cheng, Pengwei Xie, Abdusalam Abdukerim, Wei Chen, Xun Chen, Yunhua Chen, Xiangyi Cui, Yingjie Fan, Deqing Fang, Changbo Fu, et al. Search for light dark matter–electron scattering in the pandax-ii experiment. *Physical Review Letters*, 126(21):211803, 2021.

[107] P Agnes, IFM Albuquerque, T Alexander, AK Alton, M Ave, HO Back, G Batignani, K Biery, V Bocci, WM Bonivento, et al. Search for low-mass dark matter wimps with 12 ton-day exposure of darkside-50. *arXiv preprint arXiv:2207.11966*, 2022.

[108] HA Gebbie and CG Cannon. Properties of amorphous selenium and its use as an optical material. *JOSA*, 42(4):277–277, 1952.

[109] Wee Chong Tan. *Optical properties of amorphous selenium films*. PhD thesis, University of Saskatchewan, 2006.

[110] Glenn F Knoll. *Radiation detection and measurement*. John Wiley & Sons, 2010.

[111] A Darbandi, É Devoie, O Di Matteo, and O Rubel. Modeling the radiation ionization energy and energy resolution of trigonal and amorphous selenium from first principles. *Journal of Physics: Condensed Matter*, 24(45):455502, 2012.

[112] IM Blevis, DC Hunt, and JA Rowlands. Measurement of x-ray photogeneration in amorphous selenium. *Journal of applied physics*, 85(11):7958–7963, 1999.

[113] O Bubon, K Jandieri, SD Baranovskii, SO Kasap, and A Reznik. Columnar recombination for x-ray generated electron-holes in amorphous selenium and its significance in a-se x-ray detectors. *Journal of applied physics*, 119(12):124511, 2016.

[114] Xinran Li, Alvaro E Chavarria, Snezana Bogdanovich, Cristiano Galbiati, Alexander

Piers, and Brad Polischuk. Measurement of the ionization response of amorphous selenium with 122 kev γ rays. *Journal of Instrumentation*, 16(06):P06018, 2021.

[115] Xinran Li. *The energy resolution and the energy deposition processes in disordered targets for rare-event searches*. PhD thesis, Princeton University, 2021.

[116] PN Luke. Unipolar charge sensing with coplanar electrodes-application to semiconductor detectors. *IEEE Transactions on Nuclear Science*, 42(4):207–213, 1995.

[117] AE Chavarria, Cristiano Galbiati, X Li, and JA Rowlands. A high-resolution cmos imaging detector for the search of neutrinoless double β decay in 82se. *Journal of Instrumentation*, 12(03):P03022, 2017.

[118] AE Chavarria, C Galbiati, B Hernandez-Molinero, Al Ianni, X Li, Y Mei, D Montanino, X Ni, C Peña Garay, A Piers, et al. Snowmass 2021 white paper: The selena neutrino experiment. *arXiv preprint arXiv:2203.08779*, 2022.

[119] S. I. Alvis, I. J. Arnquist, F. T. Avignone, A. S. Barabash, C. J. Barton, V. Basu, F. E. Bertrand, B. Bos, M. Busch, M. Buuck, T. S. Caldwell, Y-D. Chan, C. D. Christofferson, P.-H. Chu, M. Clark, C. Cuesta, J. A. Detwiler, Yu. Efremenko, H. Ejiri, S. R. Elliott, T. Gilliss, G. K. Giovanetti, M. P. Green, J. Gruszko, I. S. Guinn, V. E. Guiseppe, C. R. Haufe, R. J. Hegedus, L. Hehn, R. Henning, D. Hervas Aguilar, E. W. Hoppe, M. A. Howe, M. F. Kidd, S. I. Konovalov, R. T. Kouzes, A. M. Lopez, R. D. Martin, R. Massarczyk, S. J. Meijer, S. Mertens, J. Myslik, G. Othman, W. Pettus, A. Piliounis, A. W. P. Poon, D. C. Radford, J. Rager, A. L. Reine, K. Rielage, N. W. Ruof, B. Shanks, M. Shirchenko, D. Tedeschi, R. L. Varner, S. Vasilyev, B. R. White, J. F. Wilkerson, C. Wiseman, W. Xu, E. Yakushev, C.-H. Yu, V. Yumatov, I. Zhitnikov, and B. X. Zhu. Search for neutrinoless double-β decay in ^{76}Ge with 26 kg yr of exposure from the majorana demonstrator. *Phys. Rev. C*, 100:025501, Aug 2019.

[120] Stanislav P Mikheev and A Yu Smirnov. Resonance oscillations of neutrinos in matter. *Soviet Physics Uspekhi*, 30(9):759, 1987.

[121] Aldo M Serenelli, Sarbani Basu, Jason W Ferguson, and Martin Asplund. New solar composition: the problem with solar models revisited. *The Astrophysical Journal*, 705(2):L123, 2009.

[122] John N Bahcall. Be 7 solar neutrino line: A reflection of the central temperature distribution of the sun. *Physical Review D*, 49(8):3923, 1994.

[123] Carlo Giunti and Thierry Lasserre. ev-scale sterile neutrinos. *Annual Review of Nuclear and Particle Science*, 69:163–190, 2019.

[124] Kou Abe, J Adam, H Aihara, T Akiri, Constantinos Andreopoulos, S Aoki, A Ariga, S Assylbekov, D Autiero, M Barbi, et al. Search for short baseline ν e disappearance with the t2k near detector. *Physical Review D*, 91(5):051102, 2015.

[125] VV Barinov, BT Cleveland, SN Danshin, H Ejiri, SR Elliott, D Frekers, VN Gavrin, VV Gorbachev, DS Gorbunov, WC Haxton, et al. Results from the baksan experiment on sterile transitions (best). *Physical Review Letters*, 128(23):232501, 2022.

[126] VV Barinov, SN Danshin, VN Gavrin, VV Gorbachev, DS Gorbunov, TV Ibragimova, Yu P Kozlova, LV Kravchuk, VV Kuzminov, BK Lubsandorzhiev, et al. Search for electron-neutrino transitions to sterile states in the best experiment. *Physical Review C*, 105(6):065502, 2022.

[127] J. N. Abdurashitov, V. N. Gavrin, V. V. Gorbachev, P. P. Gurkina, T. V. Ibragimova, A. V. Kalikhov, N. G. Khairnasov, T. V. Knodel, I. N. Mirmov, A. A. Shikhin, E. P. Veretenkin, V. E. Yants, G. T. Zatsepin, T. J. Bowles, S. R. Elliott, W. A. Teasdale, J. S. Nico, B. T. Cleveland, and J. F. Wilkerson. Measurement of the solar neutrino capture rate with gallium metal. iii. results for the 2002–2007 data-taking period. *Phys. Rev. C*, 80:015807, Jul 2009.

[128] F. Kaether, W. Hampel, G. Heusser, J. Kiko, and T. Kirsten. Reanalysis of the gallex solar neutrino flux and source experiments. *Physics Letters B*, 685(1):47–54, 2010.

[129] Jeffrey M Berryman, Pilar Coloma, Patrick Huber, Thomas Schwetz, and Albert Zhou. Statistical significance of the sterile-neutrino hypothesis in the context of reactor and gallium data. *Journal of High Energy Physics*, 2022(2):1–39, 2022.

[130] Mikhail Danilov and Nataliya Skrobova. New results from the danss experiment. *arXiv preprint arXiv:2112.13413*, 2021.

[131] Y. J. Ko, B. R. Kim, J. Y. Kim, B. Y. Han, C. H. Jang, E. J. Jeon, K. K. Joo, H. J. Kim, H. S. Kim, Y. D. Kim, Jaison Lee, J. Y. Lee, M. H. Lee, Y. M. Oh, H. K. Park, H. S. Park, K. S. Park, K. M. Seo, Kim Siyeon, and G. M. Sun. Sterile neutrino search at the neos experiment. *Phys. Rev. Lett.*, 118:121802, Mar 2017.

[132] Manoa Andriamirado, AB Balantekin, HR Band, CD Bass, DE Bergeron, D Berish, NS Bowden, JP Brodsky, CD Bryan, T Classen, et al. Improved short-baseline neutrino oscillation search and energy spectrum measurement with the prospect experiment at hfir. *Physical Review D*, 103(3):032001, 2021.

[133] H. Almazán, L. Bernard, A. Blanchet, A. Bonhomme, C. Buck, P. del Amo Sanchez, I. El Atmani, J. Haser, F. Kandzia, S. Kox, L. Labit, J. Lamblin, A. Letourneau, D. Lhuillier, M. Licciardi, M. Lindner, T. Materna, A. Minotti, H. Pessard, J.-S. Réal, C. Roca, R. Rogly, T. Salagnac, V. Savu, S. Schoppmann, V. Sergeyeva, T. Soldner, A. Stutz, and M. Vialat. Improved sterile neutrino constraints from the stereo experiment with 179 days of reactor-on data. *Phys. Rev. D*, 102:052002, Sep 2020.

[134] A. P. Serebrov, R. M. Samoilov, V. G. Ivochkin, A. K. Fomin, V. G. Zinoviev, P. V. Neustroev, V. L. Golovtsov, S. S. Volkov, A. V. Chernyj, O. M. Zherebtsov, M. E. Chaikovskii, A. L. Petelin, A. L. Izhutov, A. A. Tuzov, S. A. Sazontov, M. O. Gromov, V. V. Afanasiev, M. E. Zaytsev, A. A. Gerasimov, and V. V. Fedorov. Search for

sterile neutrinos with the neutrino-4 experiment and measurement results. *Phys. Rev. D*, 104:032003, Aug 2021.

[135] P Abratenko, D Andrade Aldana, J Anthony, L Arellano, J Asaadi, A Ashkenazi, S Balasubramanian, B Baller, G Barr, J Barrow, et al. First constraints on light sterile neutrino oscillations from combined appearance and disappearance searches with the microboone detector. *Physical Review Letters*, 130(1):011801, 2023.

[136] Michel Bissonnette, Marc Hansroul, Eric Masson, Serge Savard, Sébastien Cadieux, Patrick Warmoes, Daniel Gravel, Jerry Agopyan, B Polischuk, W Haerer, et al. Digital breast tomosynthesis using an amorphous selenium flat panel detector. In *Medical Imaging 2005: Physics of Medical Imaging*, volume 5745, pages 529–540. SPIE, 2005.

[137] Mangmang An, Chufeng Chen, Chaosong Gao, Mikyung Han, Rong Ji, Xiaoting Li, Yuan Mei, Quan Sun, Xiangming Sun, Kai Wang, et al. A low-noise cmos pixel direct charge sensor, topmetal-ii. *Nuclear Instruments and Methods in Physics Research Section A: Accelerators, Spectrometers, Detectors and Associated Equipment*, 810:144–150, 2016.

[138] Shu-Guang Zou, Yan Fan, Xiang-Ming Sun, Guang-Ming Huang, Hua Pei, Zhen Wang, Jun Liu, Ping Yang, and Dong Wang. A highly pixelated CdZnTe detector based on topmetal ii- sensor. *Chinese Physics C*, 41(4):046003, apr 2017.

[139] Yan Fan, Chaosong Gao, Guangming Huang, Zili Li, Hua Pei, Xiangming Sun, Ruiheng Sima, Dong Wang, Zhen Wang, Ping Yang, et al. Pixelated cdznte detector based on topmetal-iia readout chip. *Nuclear Instruments and Methods in Physics Research Section A: Accelerators, Spectrometers, Detectors and Associated Equipment*, 924:23–27, 2019.

[140] Zili Li, Huanbo Feng, Xuefeng Huang, Jin Zhang, Jiaqi Su, Xinchen Cai, Zuke Feng, Qian Liu, Hongbang Liu, Chaosong Gao, Le Xiao, and Xiangming Sun. Preliminary

test of *topmetal-ii-* sensor for x-ray polarization measurements. *Nuclear Instruments and Methods in Physics Research Section A: Accelerators, Spectrometers, Detectors and Associated Equipment*, 1008:165430, 2021.

[141] Xun Chen, ChangBo Fu, Javier Galan, Karl Giboni, Franco Giuliani, LingHui Gu, Ke Han, XiangDong Ji, Heng Lin, JiangLai Liu, et al. Pandax-iii: Searching for neutrinoless double beta decay with high pressure 136xe gas time projection chambers. *Science China Physics, Mechanics & Astronomy*, 60(6):1–40, 2017.

[142] Yuan Mei, Xiangming Sun, and Nu Xu. Topmetal cmos direct charge sensing plane for neutrinoless double-beta decay search in high-pressure gaseous tpc. *arXiv preprint arXiv:2010.09226*, 2020.

[143] J Spanier. Oldham, kb: An atlas of functions, 1987.

[144] MR Bhat. Nuclear data sheets for a= 57. *Nuclear Data Sheets*, 85(3):415–536, 1998.

[145] Zhong He. Review of the shockley–ramo theorem and its application in semiconductor gamma-ray detectors. *Nuclear Instruments and Methods in Physics Research Section A: Accelerators, Spectrometers, Detectors and Associated Equipment*, 463(1-2):250–267, 2001.

[146] HH Barrett, JD Eskin, and HB Barber. Charge transport in arrays of semiconductor gamma-ray detectors. *Physical Review Letters*, 75(1):156, 1995.

[147] Qiushi Zhang, Congzhe Zhang, Yanye Lu, Kun Yang, and Qiushi Ren. Progress in the development of cdznte unipolar detectors for different anode geometries and data corrections. *Sensors*, 13(2):2447–2474, 2013.

[148] Martin Berger. Estar, pstar, and astar: Computer programs for calculating stopping-power and range tables for electrons, protons, and helium ions, 1992-01-01 1992.

[149] Alvaro E Chavarria, Selena Collaboration, et al. The selena neutrino experiment. In *Journal of Physics: Conference Series*, volume 2156, page 012155. IOP Publishing, 2021.